

HIGH RESOLUTION NEAR-INFRARED IMAGING WITH TIP-TILT
ADAPTIVE OPTICS

by

Laird Miller Close

A Dissertation Submitted to the Faculty of the
DEPARTMENT OF ASTRONOMY
In Partial Fulfillment of the Requirements
For the Degree of
DOCTOR OF PHILOSOPHY
In the Graduate College
THE UNIVERSITY OF ARIZONA

1995

INFORMATION TO USERS

This manuscript has been reproduced from the microfilm master. UMI films the text directly from the original or copy submitted. Thus, some thesis and dissertation copies are in typewriter face, while others may be from any type of computer printer.

The quality of this reproduction is dependent upon the quality of the copy submitted. Broken or indistinct print, colored or poor quality illustrations and photographs, print bleedthrough, substandard margins, and improper alignment can adversely affect reproduction.

In the unlikely event that the author did not send UMI a complete manuscript and there are missing pages, these will be noted. Also, if unauthorized copyright material had to be removed, a note will indicate the deletion.

Oversize materials (e.g., maps, drawings, charts) are reproduced by sectioning the original, beginning at the upper left-hand corner and continuing from left to right in equal sections with small overlaps. Each original is also photographed in one exposure and is included in reduced form at the back of the book.

Photographs included in the original manuscript have been reproduced xerographically in this copy. Higher quality 6" x 9" black and white photographic prints are available for any photographs or illustrations appearing in this copy for an additional charge. Contact UMI directly to order.

UMI

A Bell & Howell Information Company
300 North Zeeb Road, Ann Arbor, MI 48106-1346 USA
313/761-4700 800/521-0600

HIGH RESOLUTION NEAR-INFRARED IMAGING WITH TIP-TILT
ADAPTIVE OPTICS

by

Laird Miller Close

A Dissertation Submitted to the Faculty of the
DEPARTMENT OF ASTRONOMY
In Partial Fulfillment of the Requirements
For the Degree of
DOCTOR OF PHILOSOPHY
In the Graduate College
THE UNIVERSITY OF ARIZONA

1995

UMI Number: 9620385

UMI Microform 9620385
Copyright 1996, by UMI Company. All rights reserved.

**This microform edition is protected against unauthorized
copying under Title 17, United States Code.**

UMI
300 North Zeeb Road
Ann Arbor, MI 48103

THE UNIVERSITY OF ARIZONA ®
GRADUATE COLLEGE

As members of the Final Examination Committee, we certify that we have
read the dissertation prepared by LAIRD MILLER CLOSE

entitled HIGH RESOLUTION NEAR-INFRARED IMAGING WITH TIP-TILT
ADAPTIVE OPTICS

and recommend that it be accepted as fulfilling the dissertation
requirement for the Degree of DOCTOR OF PHILOSOPHY

Donald W. McCarthy Jr.
DONALD W. MCCARTHY
Fulvio Melia
FULVIO MELIA
Hans-Walter Rix
HANS-WALTER RIX

Date
12/14/95
Date
12/14/95
Date
12/18/95
Date

Date

Final approval and acceptance of this dissertation is contingent upon
the candidate's submission of the final copy of the dissertation to the
Graduate College.

I hereby certify that I have read this dissertation prepared under my
direction and recommend that it be accepted as fulfilling the dissertation
requirement.

Donald W. McCarthy Jr.
Dissertation Director
DONALD W. MCCARTHY

12/18/95
Date

STATEMENT BY AUTHOR

This dissertation has been submitted in partial fulfillment of requirements for an advanced degree at The University of Arizona and is deposited in the University Library to be made available to borrowers under rules of the Library.

Brief quotations from this dissertation are allowable without special permission, provided that accurate acknowledgment of source is made. Requests for permission for extended quotation from or reproduction of this manuscript in whole or in part may be granted by the head of the major department or the Dean of the Graduate College when in his or her judgment the proposed use of the material is in the interests of scholarship. In all other instances, however, permission must be obtained from the author.

SIGNED: Leirich Close

ACKNOWLEDGMENTS

Technical assistance from Mr. M. Williams, R. James, J. Waack, and J. Wu in the design and construction of the Cassegrain mirror mount helped make FASTTRAC possible. Dr. M. Rieke kindly provided the original NICMOS3 infrared camera, and Dr. J. Christou performed image deconvolutions and numerical simulations of the early FASTTRAC data. Dr. B. McLeod developed software for the InSb camera. The theoretical model for Sgr A* came out of discussions with Fulvio Melia. The development of FASTTRAC was supported by NSF grant AST 88-22465 and 92-03336 and NASA NAGW 2254. The National Science and Engineering Research Council of Canada provided a graduate student fellowship which made the work in this thesis possible.

David Wittman supported the CCD and helped with the FASTTRAC observations of 10214+4724. Charles Liu, Carol Heller and John Huchra made the MMT observations of 10214+4724. Many long discussions with Pat Hall made the chapter on 10214+4724 possible. Keith Hege kindly produced the IDA deconvolved images of 10214+4724.

Development of FASTTRAC II could not have possible without the Air Force Office of Scientific Research grant #F49620-94-1-0437 to the Center of Astronomical Adaptive Optics. I would like to thank P. Gray and W. Davidson for their excellent support and ideas for the design of the tip-tilt beam combiner. Osservatorio Astrofisico di Arcetri (Firenze, Italy) provided the capacitive sensor board design for FASTTRAC II.

It is a pleasure to acknowledge the excellent support I *always* received from the entire Steward Observatory Technical Support Group and telescope operators. Support from the whole CAAO team (Dave, Guido, Mike, Roger, Pat, Ty, Jake, Todd, Gu, Peter, John, Diana, and Doris) made the last 4 years a lot more productive and enjoyable.

I'd like to thank Dave Wittman, Eric Hooper, Peter Tamblyn, George & Marica Rieke, Steve Mutz, Joe Haller, Pat Hall, Valentin Ivanov, and everyone else who helped make FASTTRAC a success by using it (despite the occasional monsoon, patch of bad seeing, or software/hardware bug; at least there was always DOOM to play).

Don McCarthy has taught me how to work with care, dedication, and respect. Although I'm sure I'll never reach the level of dedication and energy he is able to thrive in, it will always be a goal of mine. He is the main reason my years here seem so productive.

DEDICATION

This dissertation is dedicated, to Shannon, the love of my
life, who I missed every night I was away under the stars and clouds,
to my dad Nicholas, for always being interested in what I had to say,
to my mom Patricia, for giving me the guts to say it,
to Tammy for always being my friend,
and to Nana, for all her love.

TABLE OF CONTENTS

LIST OF ILLUSTRATIONS	10
ABSTRACT	13
1. AN INTRODUCTION TO ADAPTIVE OPTICS	15
1.1 Limits on High Resolution Imaging Due to the Atmosphere	15
1.1.1 How Does the Atmosphere Degrade the Long-Exposure PSF?	17
1.2 Full Adaptive Optics	19
1.3 Partial Adaptive Optics	21
1.4 Gains With Adaptive Optics	23
1.5 Summary	26
2. FASTTRAC: A TIP-TILT SECONDARY FOR HIGH-RESOLUTION INFRARED IMAGING	27
2.1 Introduction	27
2.2 Tip-Tilt Sensing at Infrared Wavelengths	29
2.3 FASTTRAC	33
2.3.1 The Original Infrared Slope Sensor	34
2.3.2 The Original Infrared Science Camera	34
2.3.3 The New Infrared Slope Sensor: The Adaptive Optics Camera	35
2.3.4 The New Visible Slope Sensor: A CCD for FASTTRAC	37

TABLE OF CONTENTS -*Continued*

2.3.5 The Tip-Tilt Cassegrain Secondary Mirror	37
2.3.6 The Original Control Computer: Hardware and Software	41
2.3.7 The New Adaptive Optics Science Camera Control Hardware and Software	43
2.4 Performance	46
2.4.1 Image Stabilization	47
2.4.2 Required Corrective Frequency	49
2.4.3 Image Quality	51
2.4.4 Long Exposure Wide Field Imaging	54
2.4.5 Post-Detection Processing: Lucy Deconvolution	56
2.5 Conclusions	58
 3. FASTTRAC IMAGING OF THE BLACK HOLE CANDIDATE SAGITTARIUS A*	 59
3.1 Introduction	59
3.2 Observations	61
3.3 Photometric Measurements and Applications	62
3.3.1 Reductions	62
3.3.2 Is This Infrared Source Sgr A*?	66
3.3.3 Is Sgr A* Variable on a Time Scale of a Year?	67
3.4 Short Time Scale Variability	70
3.5 Discussion	73

TABLE OF CONTENTS -*Continued*

3.5.1 The Morphology of the Sgr A* Infrared Source	76
3.6 Conclusions	77
4. IS IRAS 10214+4724 THE MOST LUMINOUS OBJECT IN THE UNIVERSE OR JUST A GRAVITATIONAL LENS?	78
4.1 Introduction	78
4.2 Observations	79
4.2.1 Imaging with FASTTRAC	79
4.2.2 Spectroscopy	81
4.3 Discussion	87
4.4 Conclusions	92
5. AN ADAPTIVE BEAM COMBINING MIRROR FOR THE MMT	94
5.1 Introduction	94
5.2 Design of the Beam Combiner	97
5.2.1 Capacitive Displacement Sensors	97
5.2.2 Voice Coil Drivers	98
5.2.3 PID Control Circuit	99
5.2.4 Mirror Pivots	99
5.2.5 The Tip-Tilt Mirrors	102
5.2.6 System Integration	103
5.2.7 Control Overview	104

TABLE OF CONTENTS -*Continued*

5.3 Performance	105
5.4 FASTTRAC II's Future	107
5.5 Conclusions	108
6. CONTINUING & FUTURE PROJECTS FOR FASTTRAC AND FASTTRAC II	110
6.1 The Future for FASTTRAC and FASTTRAC II	111
6.1.1 Possible FASTTRAC Upgrades	111
6.1.2 FASTTRAC II	113
6.1.3 Laser Upgrade	114
6.2 Future Tip-Tilt Astronomy	115
6.2.1 Science to Be Done With FASTTRAC	115
6.2.2 Science To Be Done With FASTTRAC II	116
6.3 Conclusions	118
APPENDIX A: THE 6.5m MMT AO SYSTEM: AN EXAMPLE OF FUTURE ADAPTIVE OPTICS SYSTEMS	119
A.1 Science To Be Done With The 6.5m System	122
REFERENCES	126

LIST OF ILLUSTRATIONS

1.1 The effect of atmospheric seeing on a PSF	16
1.2 A cartoon of the atmosphere	17
1.3 A comparison between various degrees of partial AO	22
1.4 A comparison between corrected and uncorrected telescopes ...	23
1.5 A comparison between HST and tip-tilt correction	25
2.1 The optimal λ given a D for tip-tilt correction	30
2.2 A schematic diagram of FASTTRAC	32
2.3 A self guided image of the Galactic Center	35
2.4 Diffraction-limited image of ζ Aqr	36
2.5 Schematic diagram of the tip-tilt mount	39
2.6 Schematic timing diagram	42
2.7 Time series of corrected and uncorrected image motion	45
2.8 Power spectra of corrected and uncorrected image motion	46
2.9 The centroid positions of corrected and uncorrected images	48
2.10 Residual image motion VS correction frequency	49
2.11 Residual tilt phase error VS correction frequency	51

LIST OF ILLUSTRATIONS -*Continued*

2.12 A comparison of uncorrected, corrected, and perfect PSFs	52
2.13 PSF profiles	53
2.14 Imaging the Galactic Center with and without correction	55
2.15 The Galactic Center PSFs	56
3.1 Detection of Sgr A* at H	63
3.2 Detection of Sgr A* at K	64
3.3 Detection of Sgr A* at J	65
3.4 Periodogram of the Sgr A* flux timeseries	69
3.5 Periodogram of the Sgr A* flux timeseries from the next night..	72
3.6 Sgr A*'s fluxes fit with a black hole accretion disk model.....	74
3.7 The inner 5x5" of the Galactic Center at 0.2" resolution	75
4.1 The raw and deconvolved FASTTRAC images of 10214+4724..	80
4.2 The binned continuum spectrum of 10214+4724	82
4.3 Continuum of Sources 1 & 2	84
4.4 Spectrum of Source 1 and of a galaxy 23" to the south	86
5.1 Schematic of the FASTTRAC II instrument	95
5.2 The FASTTRAC II beam combiner on the MMT	97

LIST OF ILLUSTRATIONS -*Continued*

5.3 Schematic of the tip-tilt mirrors	101
5.4 The whole beam combiner without tip-tilt mirrors	102
5.5 Closed loop response of the beam combiner at the MMT	105
5.6 Comparison between corrected and uncorrected image profiles.	106
5.7 Comparison between adaptively stacked and unstacked images.	107

ABSTRACT

The development and design of the first operational tip-tilt Cassegrain secondary mirror are presented. This system, FASTTRAC, samples image motion at up to 50 Hz by tracking either infrared ($m_K \leq 11$) or visible ($m_R \leq 16$) guide stars up to 30" and 90" away from the science target respectively. The Steward Observatory 2.3m or 1.5m telescope secondaries act as rapid tip-tilt mirrors to stabilize image motion ($\leq 0.1''$ rms; ~ 5 Hz -3 dB frequency) based on the motion of the guide star. FASTTRAC obtains nearly diffraction-limited resolutions in seeing conditions where $D/r_0 < 4$ in agreement with theoretical expectations.

FASTTRAC's unique ability to guide on infrared stars has allowed the first adaptively corrected images of the heavily extincted Galactic Center to be obtained. Over a hundred excellent ($0.28'' < \text{FWHM} < 0.6''$) images have been obtained of this region. These images do not detect any long term variations in the massive black hole candidate Sgr A*'s luminosity from June 1993 to September 1995. The average infrared magnitudes observed are $K=12.1 \pm 0.3$, $H=13.7 \pm 0.3$ and $J=16.6 \pm 0.4$ integrated over $0.5''$ at the position of Sgr A*. No significant rapid periodicities were observed from Sgr A* for amplitudes $\geq 50\%$ of the mean flux in the period range of 3-30 minutes. It is confirmed in the latest $0.28''$ FWHM image that there is $0.5''$ "bar" of emission running East-West at the position of Sgr A* as was earlier seen by Eckart et al. 1993.

The observed fluxes are consistent with an inclined accretion disk around a $\sim 1 \times 10^6 M_\odot$ black hole. However, they are also explained by a line of hot luminous (integrated

luminosity of $\sim 10^{3.5-4.6} L_{\odot}$) central cluster stars positionally coincident with Sgr A* naturally explaining the observed 0.5" "bar".

High-resolution images with FASTTRAC guiding on a faint ($R=16$) visible guide star, combined with spectra from the MMT, have shown that IRAS FSC 10214+4724 ($z=2.28$) gains its uniquely large luminosity of $\sim 1.2 \times 10^{14} h^{-2} L_{\odot}$ by gravitational lensing magnification from a nearby (1.25" away) galaxy. The detection of a tentative 4000 Å continuum break at 5690 ± 90 Å indicates that this lensing galaxy has a redshift of 0.42 ± 0.02 . A simple lensing model predicts that 10214+4724 is a "normal" background ultraluminous IR galaxy with an intrinsic (unlensed) luminosity of $\sim 3.7 \times 10^{12} h^{-2} L_{\odot}$.

CHAPTER 1

AN INTRODUCTION TO ADAPTIVE OPTICS

1.1 Limits on High Resolution Imaging Due to the Atmosphere

The main tool available to astronomers is the telescope. Simply stated the purpose of a telescope is to collect light over a large aperture (of diameter D) and focus it into a sharp image. The image that a telescope forms of a single point source (a star for example) is described by a surface function called a point spread function (PSF).

Theoretically the point spread function (PSF) of a focused star should closely resemble an Airy pattern (the diffraction pattern of a circular aperture). However, as figure 1.1 clearly demonstrates, even in good conditions the atmosphere severely degrades the PSF of a long exposure image.

To quantify a PSF one usually refers to its Strehl ratio (the ratio of the peak intensity between a PSF measured by a telescope and that theoretically predicted if that telescope were in fact perfect) and its full width at half maximum (FWHM). The Strehl ratio indicates how much of the PSF's energy is in a diffraction-limit core and the FWHM indicates how sharp the PSF is. As figure 1.1 depicts it is better to have a large Strehl ratio and a small FWHM.

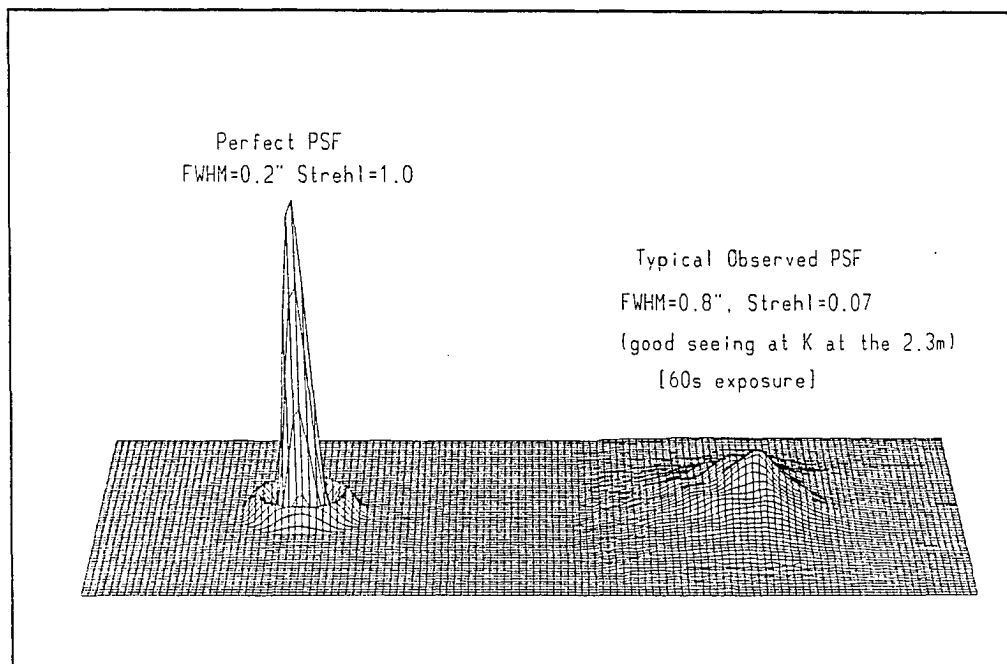


Figure 1.1: A comparison between a theoretically perfect PSF (*left*) produced by the Steward Observatory 2.3m telescope at $2.2\mu\text{m}$ and a typical PSF observed (*right*) in good "seeing" in a 60s exposure.

Theoretically the FWHM of the PSF should be very close to λ/D radians (where λ is the wavelength imaged). Therefore, a $D=2.3\text{m}$ telescope in the near infrared (in the K bandpass at $\lambda=2.2\mu\text{m}$) should have a Strehl of 1.0 and a FWHM of $0.20''$ if its optics were perfect. However, as can be seen from figure 1.1 the observed PSF of a 60s exposure degrades to a Strehl of only 0.07 and a FWHM of $0.8''$. In reality these are actually quite good values for a PSF from a 60s exposure at that particular telescope. The reason for this huge loss of resolution and sensitivity is due to atmospheric degradation (called atmospheric "seeing"). It is now well known that, even though the long-exposure FWHM of a telescope

should decrease as $1/D$, it is in fact typically almost *independent* of D (for $\lambda/D < 1''$). This means that large (very expensive) 8m telescopes produce the same $\sim 1''$ FWHM seeing-limited long exposure images as a 1m telescope at the same site.

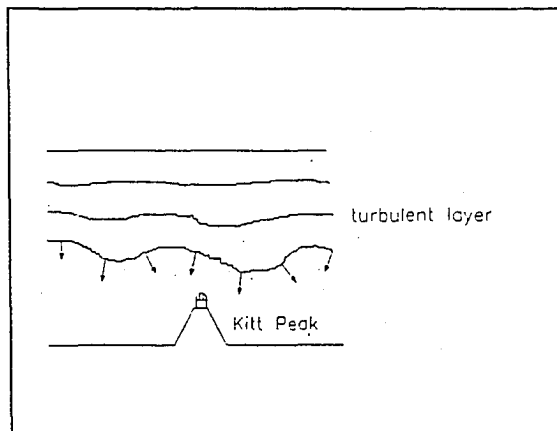


Figure 1.2: A cartoon of the distorting effect of the atmosphere on a incoming wavefront (reproduced from Schmidt 1991).

Adaptive optics (AO) attempts to limit or eliminate this atmospheric

"seeing" and restore the PSF to its diffraction-limit. It is only with an AO system that large 8m class telescopes can truly justify their enormous cost, since such an AO system would allow a 8m telescope to produce images *sixty times* sharper than a seeing-limited 1m telescope could in the visible. The advantages (and challenges) of large aperture AO will be further explored later in the chapter.

1.1.1 How Does the Atmosphere Degrade the Long-Exposure PSF?

Atmospheric "seeing" is due to the gradual random changes in phase across a wavefront as it propagates through the atmosphere (see figure 1.2). This distortion of the wavefront can be attributed to variations in the refractive index of the air (Δn) throughout the atmosphere, given by

$$\Delta n = 2 \Delta T \left(\frac{P}{T^2} \right)$$

where ΔT are the small scale turbulent changes in temperature of the air (at pressure P and temperature T) due to convection (and wind) along the line of sight. Convection manifests itself as a series of turbulent air cells of outer scale L_o (approximately 100m; although this varies from site to site) which in turn have smaller cells within and so on until cell sizes of millimeters are reached. The energy distribution $G(k)$ in such a structure is given by the Kolmogorov power spectrum

$$G(k) \propto \left[\frac{k L_o}{2\pi} \right]^2 \left[\frac{1}{\left[1 + \left(\frac{k L_o}{2\pi} \right)^2 \right]^{\frac{11}{6}}} \right]$$

where k is $2\pi/(\text{size of the cell})$.

It can be shown (Rodier 1988) that the above power spectrum describes atmospheric turbulence which produces the inhomogeneities in the refractive index (n) such that optical path fluctuations of at least several λ result along the line of sight across the telescope aperture D (where $\lambda/D < 1''$). Therefore, the instantaneous "image" actually formed by the telescope is merely the interference of many diffraction-limited interference fringe patterns from the segments of the wavefront that are random in phase across the mirror. This pattern is commonly referred to as a speckle pattern. A speckle pattern will quickly (\sim msec timescales) blur into a "gaussian-like" profile with a FWHM referred to as the "seeing disk" (typically $\sim 1''$ FWHM). Hence, long exposure images ($\Delta t > 5s$) are completely dominated

by this "seeing disk" and are independent of the true diffraction-limited resolution of the telescope.

The size of the seeing disk (α) is roughly given by $\alpha \sim \lambda/r_0$, where r_0 can be thought of as the distance across the wavefront over which the phase errors ($\Delta\phi$) are less than 1 radian rms (Fried 1966). In other words, a telescope with an r_0 sized aperture would just be able to produce a diffraction-limited image. If the telescope aperture is larger than r_0 then the short exposure image will have $\sim(D/r_0)^2$ speckles and the long exposure image PSF will be constrained to a "seeing-limited" FWHM of λ/r_0 independent of D .

Unfortunately r_0 is typically only ~ 10 cm at a good astronomical site in the visible. Therefore all ground based telescopes over 10cm in size are seeing-limited in resolution to $\sim 1''$ FWHM in the visible (V bandpass $\sim 0.55 \mu\text{m}$). However, at longer wavelengths λ increases and so fewer "wavelengths" of phase error occur across the telescope pupil. Therefore, r_0 must increase with λ . In fact it can be shown from Kolmogorov turbulence theory (cf. Roddier 1988) that $r_0 \propto \lambda^{1.2}$. This implies that, even though $r_0 = 10$ cm in the visible ($\lambda = 0.55 \mu\text{m}$), in the near infrared (K bandpass $\lambda = 2.2 \mu\text{m}$) r_0 will be ~ 52 cm!

1.2 Full Adaptive Optics

To restore a telescope's PSF to its diffraction-limit requires real-time mapping and correction of the incoming wavefront's phase errors. This can be most simply thought of as reconstructing the wavefront by sampling the wavefront from a bright guide star with at least ~ 1 subaperture per r_0 sized patch across the telescope's primary mirror. This reconstructed

wavefront allows the deviations from a plane-parallel wavefront to be determined. The opposite phase errors are then applied to a deformable mirror at a reimaged pupil of the telescope. If the whole servo loop is ~ 10 times faster than the characteristic speed of the atmosphere ($\tau_o \sim r_o/v$; v =wind speed) then the phase errors will be removed from the incoming wavefront as it reflects off the deformable mirror.

It might sound simple in theory; however, a full AO system in practice is an extremely complex, expensive, and delicate opto-mechanical system. For example, if one were to implement full AO at a 6.5m telescope in the visible it would require ~ 4000 subapertures with a 4000 actuator deformable mirror which must be updated at $\sim 1\text{KHz}$ (since $\tau_o \sim 10\text{ms}$ in the visible). Such systems also have low optical throughput (typically $\leq 1\%$) and so require bright ($V \leq 5^{\text{th}}$ mag) guide stars (to get enough S/N from each 10cm subaperture in the $\sim 1\text{ms}$ integration time). Not only do these guide stars have to be bright but they must also share the same " r_o -sized" patch of air as the science target. Therefore, these guide stars must be within the visible isoplanatic angle ($\theta_o \sim r_o/d$ where d is the height of the atmospheric turbulence) from the science target. Since $\theta_o \sim 3''$ in the visible there are very few interesting scientific targets within θ_o of a 5^{th} mag guide star. In light of this fact, and due to the overall complexity of the system, there are only a few visible wavelength AO systems in existence (cf., Fugate et al. 1991). Moreover, those that do exist were developed for mainly military and not astronomical targets where the "science" targets (such as spy satellites) are bright enough to be their own reference beacons.

A possible solution to the lack of bright guide stars is to simply create your own

reference beacon directly at the location of the science target. Artificial laser guide stars can be produced by either Rayleigh scattering (~ 20 km altitude) or by resonance scattering of a tuned dye laser off the much higher 90 km mesospheric ionized Na layer (Lloyd-Hart et al. 1995). Sodium laser guide stars can be produced with pumped dye lasers that produce $V \sim 10$ mag laser guide stars, which is still faint for the existing visible AO systems.

In any case it is far simpler to take advantage of the much larger infrared r_o and restrict the system to fully compensated imaging at $2.2\mu\text{m}$. Since a very good site like Mt. Hopkins can have $r_o \sim 100\text{cm}$ at $2.2\mu\text{m}$ (Lloyd-Hart et al. 1993) then one expects $\tau_o \sim 30\text{ms}$, and $\theta_o \sim 30''$. Based on these parameters a much simpler 6.5m AO system with only a hundred actuators and a sample/correction frequency of ~ 300 Hz is required to produce diffraction-limited images of $0.07''$ FWHM. Of course the much more complex visible AO system would have produced (if it ever worked) a sharper $0.018''$ FWHM image, but it is unlikely that this slightly sharper image would be worth the factor of ~ 40 in system complexity.

1.3 Partial Adaptive Optics

Even simpler AO systems can be built that do not produce a perfectly diffraction-limited PSF and a Strehl of unity. Such partial AO systems only try to correct the lower order aberrations of the wavefront. It was quickly realized that since r_o is so much bigger in the infrared often $D/r_o \leq 6$ for moderate sized telescopes ($D=2\text{-}3\text{m}$). In this regime correcting only the lowest Zernike terms of the wavefront or even just tip-tilt (simple image stabilization) can result in a nearly diffraction-limited image.

This is demonstrated by figure 1.3 where R/R_{\max} (the ratio of compensated to uncompensated Strehl) is predicted (and observed) to be ~ 4 for tip-tilt correction alone. There are other advantages to only correcting tip and tilt besides the simplicity of such systems. For example, the large isoplanatic angle of $\sim 60''$ and the ability to use the whole aperture of the telescope as a "subaperture" makes finding suitable guide stars much easier. In chapter 2, the advantages to tip-tilt systems will be discussed in more detail.

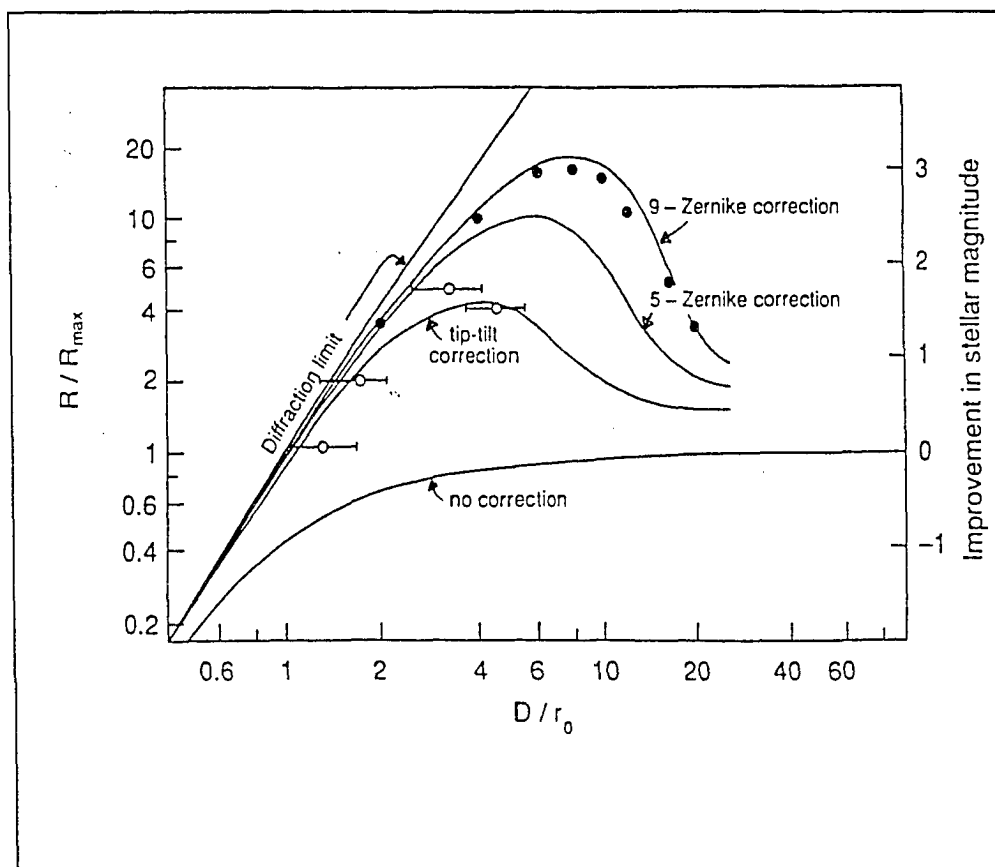


Figure 1.3: A comparison between various degrees of partial adaptive correction. Note the agreement of observational tip-tilt data with theory (open circles: tip-tilt data). The dark dots mark the predicted performance of a low order AO system (Graves et al. 1995). This figure is reproduced with permission from Roddier et al. (1991).

1.4 Gains With Adaptive Optics

It is obvious that AO provides images with improved resolutions, and needless to say higher resolution images will always provide more insight into the objects being imaged. In fact chapters 3 and 4 give detailed examples of significant astronomical results obtained from images produced by a simple tip-tilt system. *There is no field of observational astronomy that could not benefit from higher angular resolution.* Even spectrographic

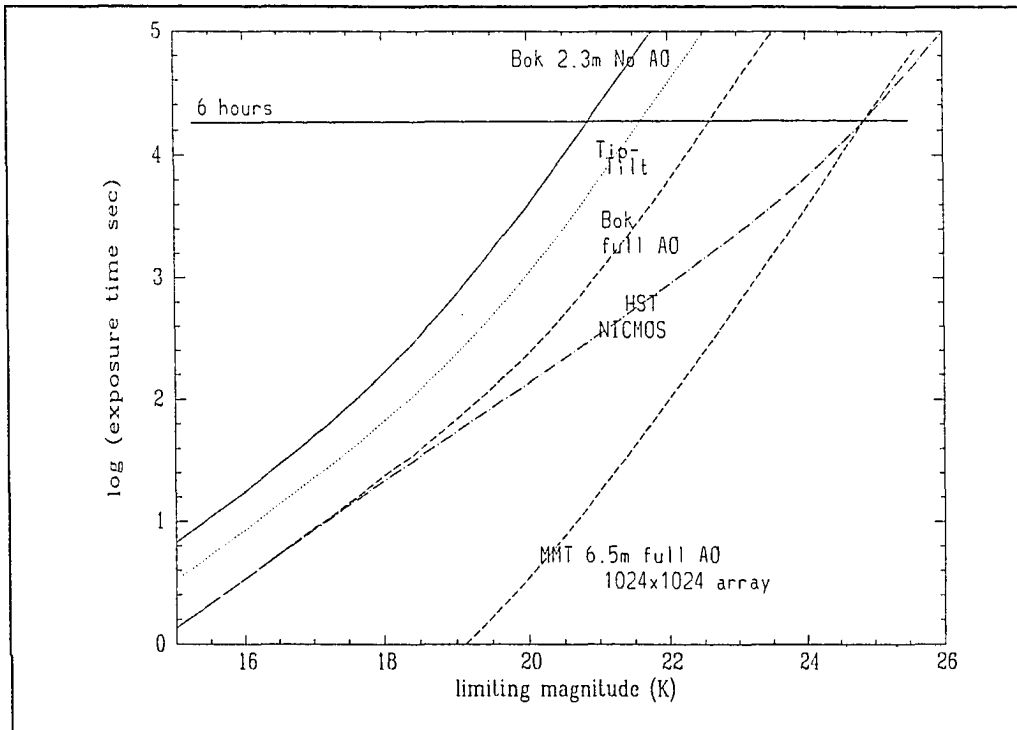


Figure 1.4: A comparison between the 2.3m (without correction, with tip-tilt, and with full AO correction) and the 6.5m with full AO and the HST NICMOS camera. In all cases the optical throughput was the same (~13%) and the detector was a NICMOS3 chip with a 0.1"/pixel platescale. Note that the 6.5m used a 1024x1024 second generation HgCdTe chip with a 10e rms readnoise.

measurements would gain from increased throughput and higher spectral-resolution using smaller slits if an AO "front-end" was used.

Another advantage of AO is that a smaller telescope with adaptive correction can in fact go deeper than a larger telescope in the same amount of integration time. For example a diffraction-limited 2.4m telescope can detect a $M_V = -7$ star at 150Mpc (in ~24 hrs) whereas the 10m KECK telescope (*with 17 times more light grasp*) will only detect such a star at 120 Mpc.

Figure 1.4 theoretically compares the Steward Observatory 2.3m telescope without AO, with tip-tilt only, and with full AO. There is a notable gain of ~1 magnitude with tip-tilt alone (in agreement with figure 1.3), and a factor of ~2 magnitudes with full AO. It is also apparent that the corrected telescope is effectively 25 times more efficient with costly telescope time.

Even more impressive performance can be obtained from the infrared full AO system like that outlined earlier for a 6.5m telescope (like the MMT 6.5m upgrade). Such a system would go ~4 magnitudes deeper and be ~1000 times more efficient than the uncorrected 2.3m. It is interesting to note that figure 1.4 shows that the 2.4m Hubble Space Telescope (HST) NICMOS near infrared camera (which is automatically diffraction-limited because it is *above* the atmosphere) is just as efficient as the much larger diffraction-limited 6.5m after 6 hours. This is mainly due to the much lower sky background that NICMOS will enjoy from HST when it becomes operational in 1997.

Of course HST can already obtain diffraction-limited imaging in the visible, in fact

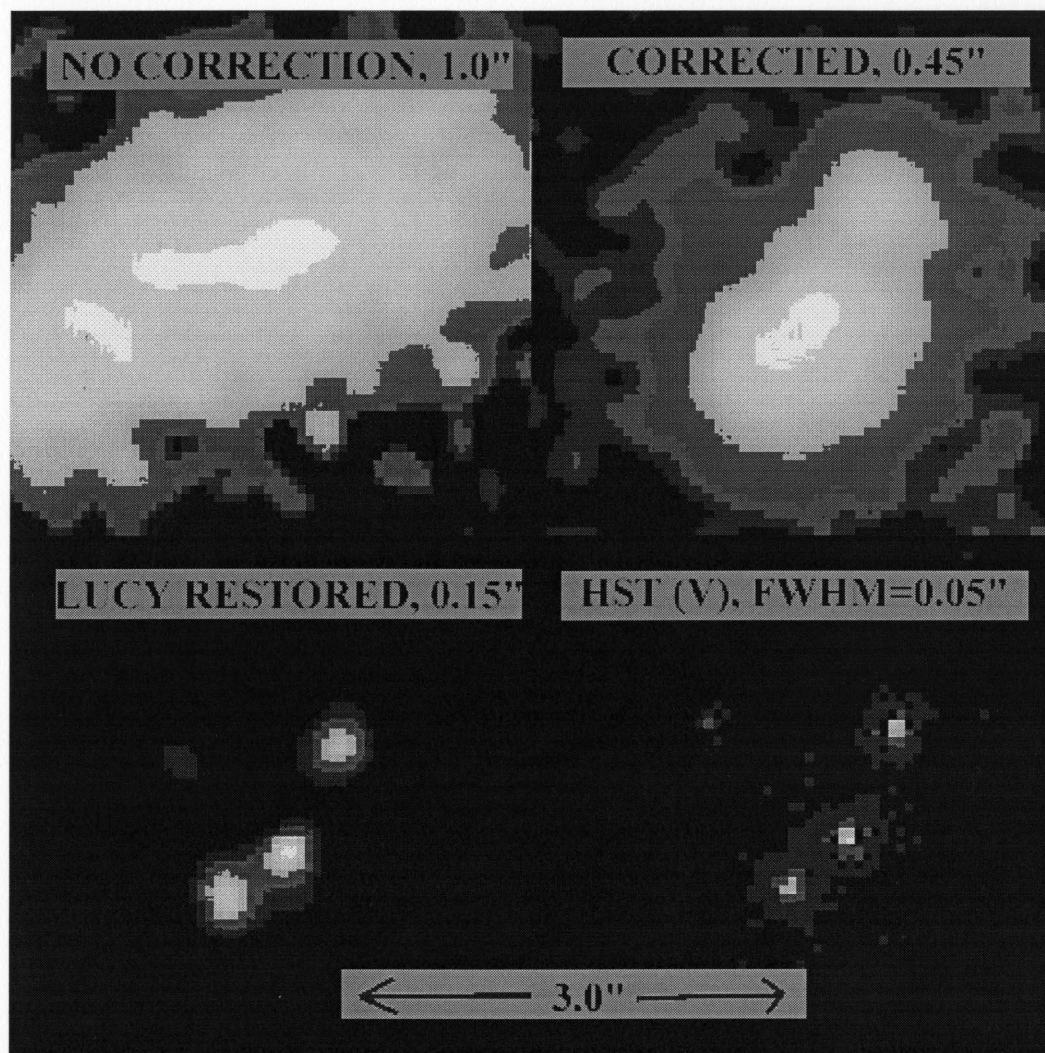


Figure 1.5: (*upper left*) A typical uncorrected image of the gravitationally lensed QSO 1422+231 (at $1.6\mu\text{m}$). (*upper right*) A 60s exposure that is tip-tilt corrected. (*lower left*) A Lucy deconvolved image of the tip-tilt corrected image. (*lower right*) An image of the field taken with the HST in the visible. Note how the deconvolved infrared image (lower left) is very similar to the HST image, except that the infrared image clearly detects the (faint) lensing infrared galaxy (for the first time). HST however detects the very faint 4th component of the lens which is not visible in the shorter infrared exposure.

The detection of the lensing galaxy has allowed estimates of its redshift. Its position will help modify models of this lensed system. Images of this quality should be able to measure a time delay between the lensed components, allowing the possibility of a independent estimate of H_0 sampled out to the QSO redshift of $z=3.6$ to be made.

HST can produce Nyquist sampled 0.036" images at say 0.4 μm with the FOC (3.5" FOV) and 0.1" pixel-limited images over a larger 35" FOV with WFPC II. Even though HST can provide the best images in the visible for general astronomy at the moment, it is a *very* over-subscribed instrument and so it is not available for many projects. HST was also extremely expensive to get fully operational (~3 billion dollars) compared to the few million dollars required to produce a full infrared AO system on a larger ground-based telescope which could obtain comparable resolutions. As will be discussed in chapter 2, even simple tip-tilt systems can produce similar resolutions as HST with the use of post-detection processing techniques such as deconvolution (see figure 1.5). Moreover, figure 1.5 shows how high-resolution ground-based infrared images are a good complement to the visible images produced by HST.

1.5 Summary

This chapter reviewed why the atmosphere degrades ground-based astronomical images. It was discussed how much easier it is to correct near infrared images compared to visible images. In addition, it was found that partial AO is a good compromise between performance and instrumental complexity.

Adaptively corrected telescopes not only produce higher resolution images but they also are much more efficient instruments. The next chapter describes a real astronomical tip-tilt AO system developed at Steward Observatory.

CHAPTER 2

FASTTRAC: A TIP-TILT SECONDARY FOR HIGH- RESOLUTION INFRARED IMAGING

FASTTRAC has become the most popular system for high resolution infrared imaging at the 2.3m and 1.5m telescopes. In this chapter the FASTTRAC instrument designed by Don McCarthy and myself is introduced. Both the original configuration and the present system configuration will be described. FASTTRAC's performance will also be outlined here.

2.1 Introduction

As mentioned in chapter one, AO restores the diffraction-limited imaging performance of large aperture telescopes by sensing and correcting atmospheric perturbations of the wavefront at high speed. Several adaptive systems are in use by both astronomical and military groups (cf., Rousset et al. 1990; Fugate 1992; Graves et al. 1995). Unfortunately, the usual approach of sampling the incident wavefront over many r_o -sized subapertures at a re-imaged pupil has led to instrumental complexity, low optical throughput, and high thermal background emission. If adaptive correction could be accomplished at a telescope's secondary mirror, much of this complexity would be reduced (cf. Sandler et al. 1995).

A simple, yet powerful, application of the adaptive secondary concept is to correct the two-dimensional slope ("tip-tilt") of the wavefront over the entire telescope aperture (D). In the near-infrared ($1\text{-}5\text{ }\mu\text{m}$), the Fried coherence parameter, r_0 , is relatively large ($0.5\text{-}2.0\text{ m}$) and so D/r_0 can be small. Under these conditions, the short exposure point spread function is dominated by a single, diffraction-limited speckle moving in the focal plane. According to Kolmogorov turbulence theory, such tip-tilt variations constitute 87% of the mean square wavefront phase error (Fried 1965). For $D/r_0 < 6$, tip-tilt correction improves image resolution up to a factor of ~ 4 and decreases the mean square wavefront phase error a factor of ~ 5.5 . An additional improvement can be gained by tracking the image's brightest speckle instead of its centroid (Christou 1992).

Because tip-tilt correction uses the *entire* telescope aperture for wavefront slope determination, it offers several advantages over fully adaptive techniques which must utilize many r_0 -sized subapertures. For example, it permits $\sim (D/r_0)^2$ more light for the centroid calculation and requires $\sim 3(D/r_0)^2$ fewer parameters to be measured and corrected. Based on a "frozen" turbulence atmospheric model, where static turbulence is blown across the telescope aperture, the timescale for tip-tilt fluctuations is $\sim (D/r_0)$ times slower. Furthermore, the field-of-view ("isoplanatic patch"), over which centroid motions remain highly correlated, is considerably larger for tip-tilt correction (radius $\geq 60''$; Roddier et al. 1991). For all these reasons, the probability of finding a suitable tip-tilt guide star is much higher.

An image obtained by tip-tilt correction preserves diffraction-limited information but, in general, exhibits a Strehl ratio, significantly less than unity. Nevertheless, such partially

corrected images are a considerable improvement over completely uncorrected images, and they can be improved further by image processing algorithms as demonstrated by the deconvolved tip-tilt data in figure 1.5.

This chapter describes the design and performance of an inexpensive tip-tilt secondary mirror system on the Steward Observatory 2.3m telescope. The complete instrument, known as FASTTRAC (Fast Adaptive Secondary for Tip-Tilt Removal by Automatic Centroiding), obtains nearly diffraction-limited images in the near-infrared and has been used to make the first adaptive images of the Galactic Center (Close et al. 1992). Other examples of unique science done with FASTTRAC will be covered in chapter 4.

2.2 Tip-Tilt Sensing at Infrared Wavelengths

Fluctuations in wavefront slope can be sensed equally well in the visible or infrared (Wittman et al. 1992). In fact, several rapid guiding systems are already in operation at visible wavelengths (Thompson and Ryerson 1984; Maaswinkel et al. 1988; Brown et al. 1988; McClure et al. 1989; Major et al. 1990; Golimowski et al. 1992, McCaughrean et al. 1994). All of these achieve tip-tilt correction with an additional small tip-tilt mirror located near the focal plane. Only FASTTRAC (and now CHARM; McCaughrean et al. 1994) takes advantage of the improvements possible by tracking at infrared wavelengths.

Since r_o scales as $\lambda^{1.2}$ it is possible to tip-tilt correct larger apertures in the infrared compared to the visible, yielding an increase in limiting magnitude for both scientific fields and, more importantly, for guide stars. As illustrated in figure 2.1, a 2.3m aperture is ideal

for tip-tilt corrective imaging in the K band ($2.2\ \mu\text{m}$). Such images should yield resolutions close to a FWHM of $0.2''$.

It is also advantageous to *track* in the infrared, since the total number of speckles, $\sim(D/r_0)^2$, in the instantaneous image is much smaller than in the visible. As a result, it becomes possible to track the brightest speckle in order to maintain the highest possible

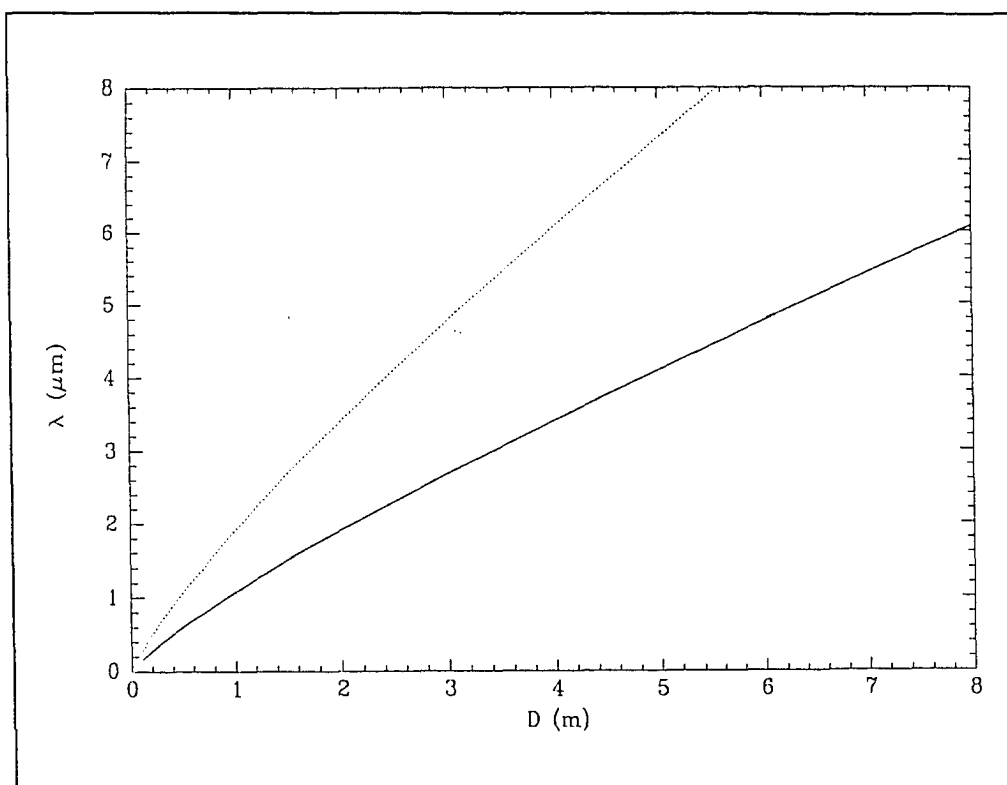


Figure 2.1: The optimal tip-tilt corrected wavelength as a function of telescope aperture. The dashed line indicates the wavelength at which $D/r_0=4$ for a site where $r_0=5\text{ cm}$ at $0.5\ \mu\text{m}$. The solid line describes a superior site where $r_0=10\text{ cm}$ at $0.5\ \mu\text{m}$. Note that FASTTRAC's 2.3m aperture is nearly ideal for tip-tilt corrected imaging near $2.2\ \mu\text{m}$ (the K infrared band) in good seeing ($r_0=10\text{ cm}$ at $0.5\ \mu\text{m}$).

resolution. For example, for $D/r_0=3.45$, Christou (1992) has shown that the brightest speckle contains a substantial fraction ($\sim 30\%$) of the total image power and that by tracking it, instead of the centroid, one achieves a significantly higher Strehl ratio (0.40 vs 0.32) in the final image. By improving the amount of power at the highest spatial frequencies, this technique also enhances the ability of deconvolution algorithms to eliminate artifacts and to further sharpen the image by post-detection processing.

Another reason to choose infrared wavefront sensing is that guide stars are more prevalent in fields that suffer from high extinction. For example, the Galactic Center is devoid of bright visible guide stars due to the large ~ 31.5 magnitudes of visual extinction (Rieke et al. 1989) whereas at $2.2\ \mu\text{m}$ the extinction is only ~ 3.5 mag. In order to utilize infrared guide stars in such fields, FASTTRAC was designed for infrared wavefront sensing.

However, the relatively high (50 electron rms) read noise of FASTTRAC's new infrared camera (the Adaptive Optics Science Camera) limits the use of infrared guide stars to those brighter than 11^{th} mag at K. Therefore, a six electron rms low-readnoise CCD has been developed for FASTTRAC by David Wittman (Close et al. 1994). This CCD allows FASTTRAC to track a visible guide star of $R\sim 16^{\text{th}}$ mag at $\sim 50\text{Hz}$ (within $90''$ of the science target) allowing many more fields on the sky to be corrected. Tracking in the visible and science imaging in the infrared also allows a bright science object (like the core of Seyfert galaxy) to be tracked and imaged at the same time.

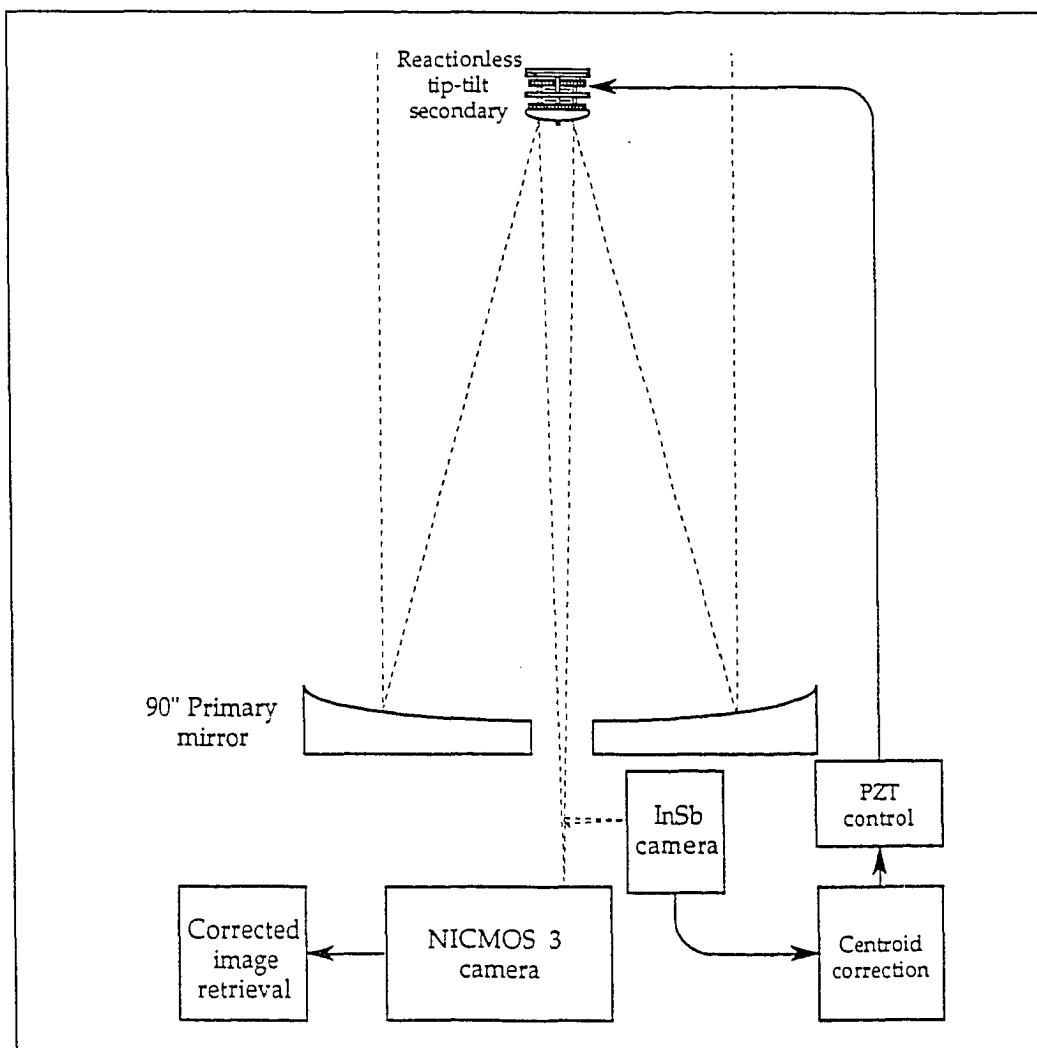


Figure 2.2: A schematic diagram of the original FASTTRAC tip-tilt correcting instrument. Converging light from a guide star reflects off a small pick-off mirror into the InSb infrared camera for high speed tracking of the guide star's centroid or brightest speckle. Piezoelectric actuators (PZTs) drive the secondary mirror to recenter the image. This stabilization process continues while the NICMOS3 science camera obtains a long exposure image of a $54 \times 54''$ tilt corrected field.

The InSb camera has now been replaced with a CCD and the pickoff mirror is now a dichroic for visible guide star tracking. In the case of infrared guiding, the new NICMOS3 Adaptive Optics Science Camera now acts as both a infrared tracking and science camera.

2.3 FASTTRAC

In light of the above arguments, a unique Cassegrain instrument, FASTTRAC, was developed in the Fall of 1991 at Steward Observatory (Close and McCarthy 1993). This instrument was designed to provide diffraction-limited images in the near-infrared using the 2.3m telescope on Kitt Peak and the 1.5-m telescope on Mt. Bigelow.

As illustrated in figure 2.2, the original configuration of FASTTRAC has a small diagonal pick-off mirror sending light from a guide star onto an InSb infrared detector array (McCarthy, McLeod, and Barlow 1990) which tracks either the brightest speckle or centroid at 2.2 μm . Wavefront slope stability is maintained by retilting the Cassegrain secondary mirror at speeds as high as 100 Hz closed-loop. A 256x256 pixel NICMOS3 infrared camera in the focal plane takes long exposures of the remaining tip-tilt corrected field-of-view around the pick-off mirror, providing scientific information at high angular resolution over the wavelength range 1-2.5 μm . Now FASTTRAC utilizes either a dichroic fed CCD or a subarray on the science detector itself to act as the guider.

Because this was the first operational tip-tilt secondary (there are now similar systems in operation at the University of Hawaii's 88inch telescope and the IRTF), FASTTRAC had to address novel engineering problems that will be relevant to the development of larger tip-tilt (or fully adaptive) secondaries now planned for many existing telescopes (UKIRT, CTIO 4-m) and future large telescopes (MMT 6.5-m, Keck I & II, GEMINI, LBT, and SUBARU). Consequently, FASTTRAC's development may serve as a guide for these projects.

2.3.1 The Original Infrared Slope Sensor

An InSb infrared speckle camera (McCarthy, McLeod, and Barlow 1990) originally served as the slope sensor. This camera consists of a focal plane detector array housed in a cryogenic dewar with selectable magnifications and filters. The detector is a direct readout, 58x62 InSb diode array developed by Santa Barbara Research Corporation. The controller electronics select different readout modes, including nondestructive reads and subarray pixel addressing. Plate scales of 0.5, 0.13, 0.065"/pixel are available depending on the brightness of the guide star and the method of tracking image motion. A scale of 0.5"/pixel is used for centroiding and 0.065 "/pixel for tracking the brightest speckle.

This camera allows tracking a guide star's brightest speckle, or image centroid, at ~100 Hz in a closed-loop feedback with the tip-tilt secondary mirror. Typically only a small subarray of the InSb array, centered on the guide star, is readout rapidly. In this fast readout mode (18 μ sec/pixel pair), the camera system has a relatively large read noise of ~500 electrons(rms)/pixel.

2.3.2 The Original Infrared Science Camera

The original science camera uses a 256x256 pixel NICMOS3 near-infrared (~1-2.5 μ m) array detector (Rieke et al. 1993) which is similar to that now used in the new Adaptive Optics Science Camera. The pixel scale was a somewhat coarse 0.21"/pixel yielding a 54x54" field-of-view within the expected isoplanatic patch for tip-tilt correction. However, this large field-of-view does not provide Nyquist sampling of the diffraction-limit, so the

resulting image quality is somewhat degraded. Science frames are sent immediately to an adjacent SUN workstation via ethernet to provide quick feedback about tip-tilt performance and scientific results.

2.3.3 The New Infrared Slope Sensor: The Adaptive Optics Science Camera

The previous InSb tracking camera had several disadvantages as a slope sensor. In particular its high readnoise of ~ 500 e rms limited FASTTRAC to very bright guide stars of $K \sim 8$. In addition, the use of a small pick-off mirror was awkward to easily, and flexibly acquire guide stars. To solve these problems a new Adaptive Optics Science Camera

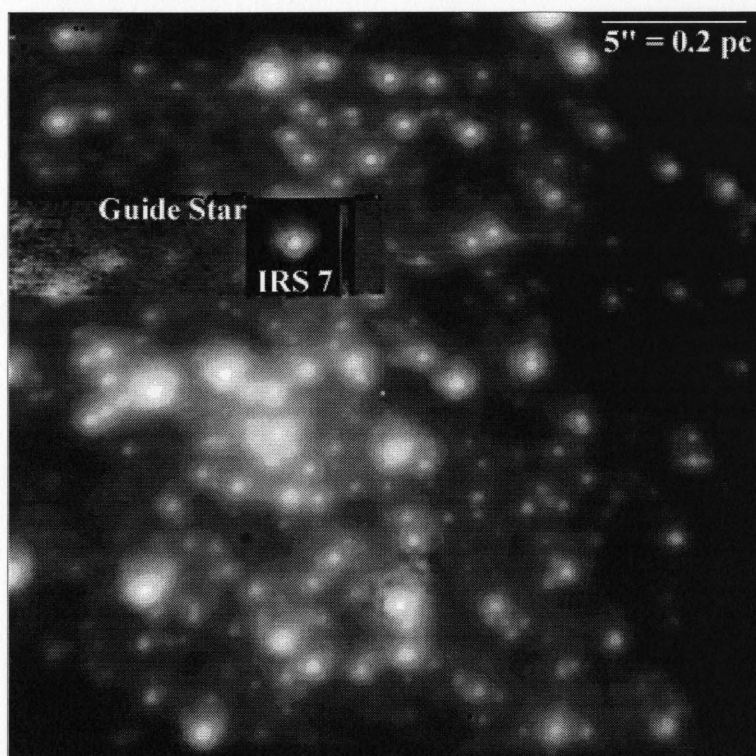


Figure 2.3: A typical FASTTRAC (60s) image obtained by guiding at 40Hz on a bright star at the Galactic Center with a 32x32 subarray (0.1''/pixel) of the Adaptive Optics Science Camera's 265x256 NICMOS3 array (FWHM = 0.28'', Strehl=0.20 at 2.2 μ m).

was developed which could act as a 256x256 science camera *and* as a tilt sensor at the same time.

The new Adaptive Optics Science Camera is a unique and versatile stand-alone instrument in its own right. It is capable of providing Nyquist sampled diffraction-limited imaging on any telescope with a $f/45$ beam at K ($2.2\mu\text{m}$), H ($1.6\mu\text{m}$), and J ($1.2\mu\text{m}$). The camera produces short-exposure diffraction-limited images with FASTTRAC at the Steward Observatory 2.3m telescope at Kitt Peak. The detector can be read out in 50ms for the full frame or at much higher rates for a subarray (up to 300Hz for a 10×10 box). The camera can uniquely select a subarray (centered on a guide star) and read it out at high speed while the rest of the detector integrates. Hence, the camera can act as an infrared tilt sensor and a science camera simultaneously. Therefore heavily extincted fields that have no bright visible guide stars but are rich in infrared guide stars, can be tracked by using FASTTRAC and this science camera. For example, figure 2.3

depicts what a typical frame looks like after utilizing a 32×32 subarray (centered on a bright infrared star IRS 7; $K\sim 6.7$ mag) for tracking (40Hz) at the Galactic Center where there are no nearby bright visible guide stars.

This camera is unique in that only *one* subarray is destructively readout from any one of the four NICMOS quadrants, unlike the MAGIC



Figure 2.4: A sum of 500 70ms speckle images (from the 2.3m telescope) shifted and added together (Strehl=0.5, FWHM=0.2" at $2.2\mu\text{m}$)

camera which corrupts data around the subarray in all *four* quadrants when employing this technique (McCaughrean & Stauffer 1994). The 50 electron rms readnoise of the NICMOS chip limits the camera to infrared guide stars of $K < 11^{\text{th}}$ mag.

The camera has obtained diffraction-limited images without AO by utilizing "shift and add" post processing techniques (see figure 2.4). This image illustrates the excellent imaging potential of the camera (Strehl 0.5, FWHM = 0.2" in a typical 70ms exposure).

2.3.4 The New Visible Slope Sensor: A CCD For FASTTRAC

Since the new infrared tip-tilt sensor has a relatively large read noise of ~50 electrons rms it is still desirable to add a lower read noise CCD to FASTTRAC. David Wittman has supported a 6 electron rms read noise 64x64 frame transfer CCD for use with FASTTRAC. This new CCD is fed by 95% reflectance (0.5- ~1 μm) dichroic placed above the science camera, which passes ~90% of the infrared light down to the science camera (see figure 2.2). This new CCD can track guide stars as faint as $R \sim 16$ at the 2.3m telescope at 50Hz sample rates. Since the CCD (with a FOV of 15x15") is mounted on a X-Y translation stage at the focal plane it can utilize guide stars up 90" away from the science target. It was with this CCD that the science results reported in chapter 4 were obtained.

2.3.5 The Tip-Tilt Cassegrain Secondary Mirror

The key to FASTTRAC (no matter which tracking camera is used) is its compact tiltable Cassegrain secondary mirror. At both the 2.3m and 1.5m telescopes the standard f/45

infrared secondary mirrors have been retrofitted with new mounts to provide high speed tilting motions in two dimensions. The 2.3m secondary is light-weight (800 g) and compact (diameter 16.5 cm), and so it provides relatively low inertia and can be moved rapidly without inducing vibrations in the telescope structure. The design of the mirror mount is a modified version of that developed for the SIRTf secondary mirror mechanism (Stier et al. 1989). For FASTTRAC piezoelectric (PZT) actuators are used to tilt the secondary because they provide large forces (100 N) and a large operating bandwidth (~ 200 Hz).

To achieve nearly diffraction-limited resolutions at K, FASTTRAC was required to stabilize image motion to less than half λ/D . To achieve less than 0.1" of image motion required that FASTTRAC have a correction frequency (the speed at which independent centroids are measured and the mirror recentered) of at least ~ 50 Hz for a relatively strong 10m/s wind. To achieve this correction frequency required that the mirror have a bandwidth and fundamental resonance well above 50 Hz.

Therefore the design goal of the tip-tilt secondary mirror was to stabilize images to $<0.1''$ rms in the focal plane with a total throw of $\pm 2.4''$ to overcome the tracking errors in right ascension (RA). This criterion is equivalent to controlling the edge of the secondary mirror to within $0.55 \mu\text{m}$ rms. To achieve this high degree of relative positioning, three Physik Instrumente low voltage PZTs equipped with strain gages (model P-820.20) and controlled by an amplifier system (model P-865.30) were used. The strain gages form a feedback loop capable of accurate expansion to $\sim 0.12 \mu\text{m}$ rms (or $\sim 0.02''$ in the focal plane) without error due to drift or hysteresis. The PZTs retained their operating bandwidth (~ 200

Hz) despite the use of 12 m extension cables between the PZTs, at the secondary, and the control electronics located at the Cassegrain focus. However, the extra resistance in these cables necessitated a major recalibration of the servo-electronics.

The design goal for image stabilization placed a stringent limitation on any induced

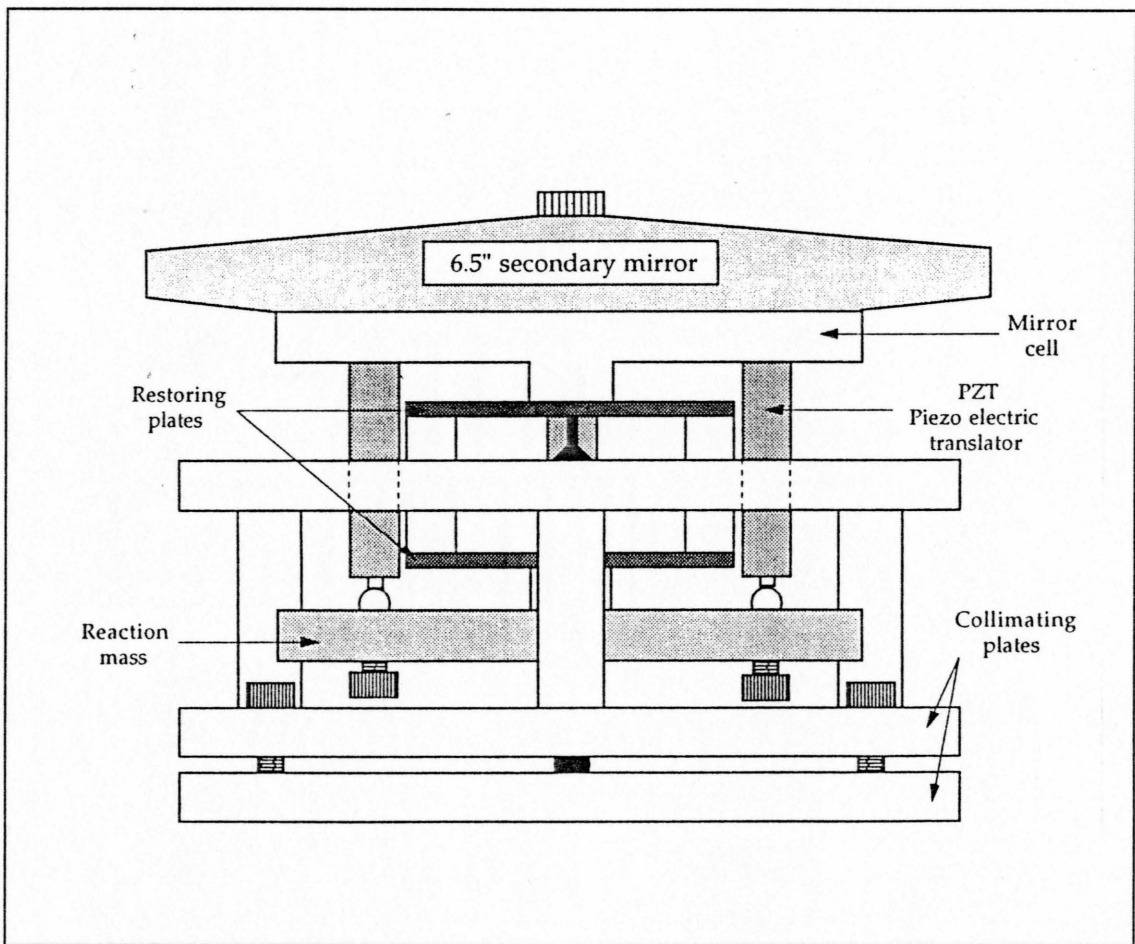


Figure 2.5: A schematic diagram of the 2.3m telescope's tip-tilt secondary mirror. The mirror is attached to a rigid cell which is rapidly steered by three piezoelectric (PZT) actuators (the third PZT is hidden from view). The system is reactionless since the PZTs displace both the reaction mass and the mirror equal amounts but in opposite directions.

vibrations of the telescope structure. For this reason, the secondary mount was designed to be reactionless (or momentum compensated) by placing the PZTs at equilateral positions sandwiched between the mirror cell (total moving mass of 1300 g) and a reaction mass (or "dummy mirror") also of 1300 g (cf., figure 2.5). Thus, the stroke (max 30 μm) of each actuator is divided equally between the real and dummy mirrors. The PZTs are mechanically preloaded and operated about their midrange voltage levels. In this configuration, both masses are acted on by equal but opposite torques. Hence, the internal torques cancel, resulting in no net vertical force applied to the support spider struts. However, since the pivot points are ~ 2 cm above and below the moving surfaces, a net lateral force is produced. This force, however, is negligible because the typical dynamical displacement of the center-of-mass is small (~ 0.5 μm) and because the total dynamical mass is low (2600 g). To test the degree of momentum compensation, a position sensor was applied to the spiders during operation. No vibration was detected down to the limit of the sensitivity of the probe (~ 0.3 μm rms from 0 to 4 kHz).

The reason no vibration was induced is, in part, due to the high fundamental resonance achieved in the mount. High resonant frequencies are less likely to be excited by the normal closed-loop operation of the secondary. To achieve a high fundamental resonant frequency, the entire dynamical system was designed for high stiffness. Two 1/8 inch thick stainless steel restoring plates are used as the flexible members (cf., figure 2.5). The PZT's must bend the plates to steer the mirror. These plates provide high stiffness (~ 14 N/ μm at the PZT positions) and led to a fundamental resonance at ~ 500 Hz. However, the coupling

between the secondary mirror and its cell is less stiff, resulting in a lower resonance at ~200 Hz. This lower resonance is successfully damped by tightly pressing the mirror into a bed of vibration damping material located between the backside of the mirror and the cell. Hence, the mirror responds to the PZT square wave drive signal with a critically damped motion. This critically damped response minimizes extraneous mechanical ringing and maximizes the duty cycle.

2.3.6 The Original Control Computer: Hardware and Software

A custom computer system interfaces to both the original InSb camera system and the tip-tilt secondary mirror. It receives analog signals from the InSb camera electronics, digitizes them to 16 bit accuracy and, as described below, calculates the image centroid or the position of the brightest speckle. It then modifies the control voltages of the three PZTs on the secondary mirror mount to recenter the image. While positioning the mirror, the InSb pixels are reset and a new readout begins.

The simplicity of using a single computer for slope sensing and control of the tip-tilt secondary mirror saves critical operational bandwidth. This leads to typical duty cycles of over 70% for closed-loop frequencies of 35 Hz or lower. The timing sequence of the tip-tilt correction process is illustrated in figure 2.6. After a short integration ($T=5-20$ ms) to "freeze" the atmosphere, either the centroid is determined within ~0.01" or the position of the brightest speckle is located to within one pixel (0.065") and a 5x5 box is fit around it.

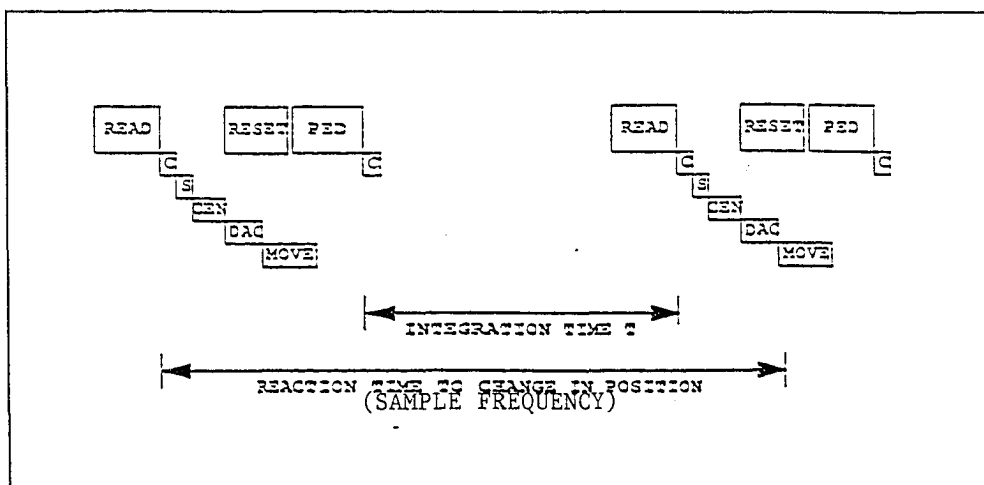


Figure 2.6: A schematic timing diagram of the InSb slope sensor software. After an integration of T milliseconds, the subarray is readout (READ; 1.7ms 12x12 box) and the image intensities are copied to memory (C; 0.2ms). Then the residual pedestal intensities (PED; 1.7ms) on the subarray are subtracted (S; 0.2ms) and the speckle frame is displayed. Next, the brightest pixel is located or the centroid is calculated around this pixel in a 5x5 box (CEN; 1.6ms). The correct steering voltages are applied to the PZTs to recenter the guide star (DAC; 1.5ms). Next, the mirror recenters the guide star (MOVE; 2 ms) while the subarray is reset. Finally, the next pedestal is taken (PED) and a new integration starts, renewing the cycle.

The same timing diagram applies to the new Adaptive Optics Science Camera when it is used for infrared tracking. The main difference is that resets are only applied when the subarray is approaching saturation (every 20 frames or so for example). The new camera also waits until the DAC's are set and the subarray displayed before the subarray is reset. For the new camera READ takes 17.4ms for a 32x32 subarray and the time required from C to MOVE is ~3ms.

Next, the computer controlling the readout electronics enables the piezoelectric translators (PZTs) to steer the secondary and recenter the image. Meanwhile, the subarray is reset and the next integration cycle begins. This process continues until the necessary exposure time has been reached on the science camera.

The old InSb guider had an advantage over the new infrared guider in that it could

use a much coarser platescale than the science camera. For example, in centroiding mode a 0.5"/pixel scale was used to increase the S/N of faint guide stars. The control algorithm begins by reading out a subarray (typically 12x12) of pixels on the InSb camera. It then searches an 8x8 pixel portion of this subarray for the position of the image peak on the InSb camera. Next, the centroid is calculated from within a smaller 5x5 pixel box centered at the brightest pixel location. If necessary, sky background flux can be subtracted before the centroid is calculated.

In software, an adjustable gain multiplies the digital correction signals before they are converted to analog voltages and sent to the PZT's controller. This optimizes the calibration between detected motion in the focal plane and mirror tilt. The value of this gain parameter is typically ~ 0.8 , depending on seeing conditions and on the size of the centroiding box.

2.3.7 The New Adaptive Optics Science Camera Control Hardware and Software

The new Adaptive Optics Science Camera is controlled by a 90MHz Pentium computer which can grab camera images at up to ~ 100 Mbytes/s by use of a customized Data Raptor (VESA local bus) frame grabber. The customized camera control electronics built by Infrared Labs Inc. allow full 256x256 frames to read out in 50ms. The electronics also allow a subarray (see figure 2.3 for example) for slope sensing be read out at much higher speeds (~ 200 Hz for a 10x10 box). The Pentium can take advantage of these high data rates and can transfer, process, scale, and display double correlated frames on its high resolution SVGA

display in a "movie" mode at $\sim 3\text{Hz}$, or in "speckle" mode at much higher speeds (70Hz for a 16×16 box). Movie mode can use "on the fly" sky subtraction to aid in the acquisition of faint objects. Speckle mode dramatically decreases time lost in focusing the camera since it can now be done in "real time".

When the camera is acting as the infrared slope sensor, the readout of the subarray and tilt correction follows a similar timing pattern as that depicted in figure 2.6. As with the InSb camera this new camera uses only the single Pentium to grab the subarray and calculate the brightest speckle's location (with a 5×5 centroid box centered on the brightest pixel) and then apply the correction to the secondary through the use of three internal DACs.

The Pentium can store both subarray speckle frames and full 256×256 frames to its 2 Gigabytes of hard disk space. It can also send the data (via ethernet) automatically to a nearby SUN workstation for further reduction with the IRAF astronomical data reduction package. To approach observing efficiencies of $\sim 95\%$ (for one minute exposures) the Pentium can also raster scan the telescope (via a high speed serial link) and turn on or off the tip-tilt tracking in the subarray.

In the FASTTRAC configuration where the new Adaptive Optics Science Camera is used only as the science camera and the CCD is the slope sensor, then the Pentium controls the CCD (via ethernet) *and* the science camera for single keyboard user friendliness and efficiency. In this manner the quad cell position on the CCD can follow the guide star as it is raster scanned across the CCD by the telescope. This also dithers the science field on the science camera and avoids costly off-source sky frames.

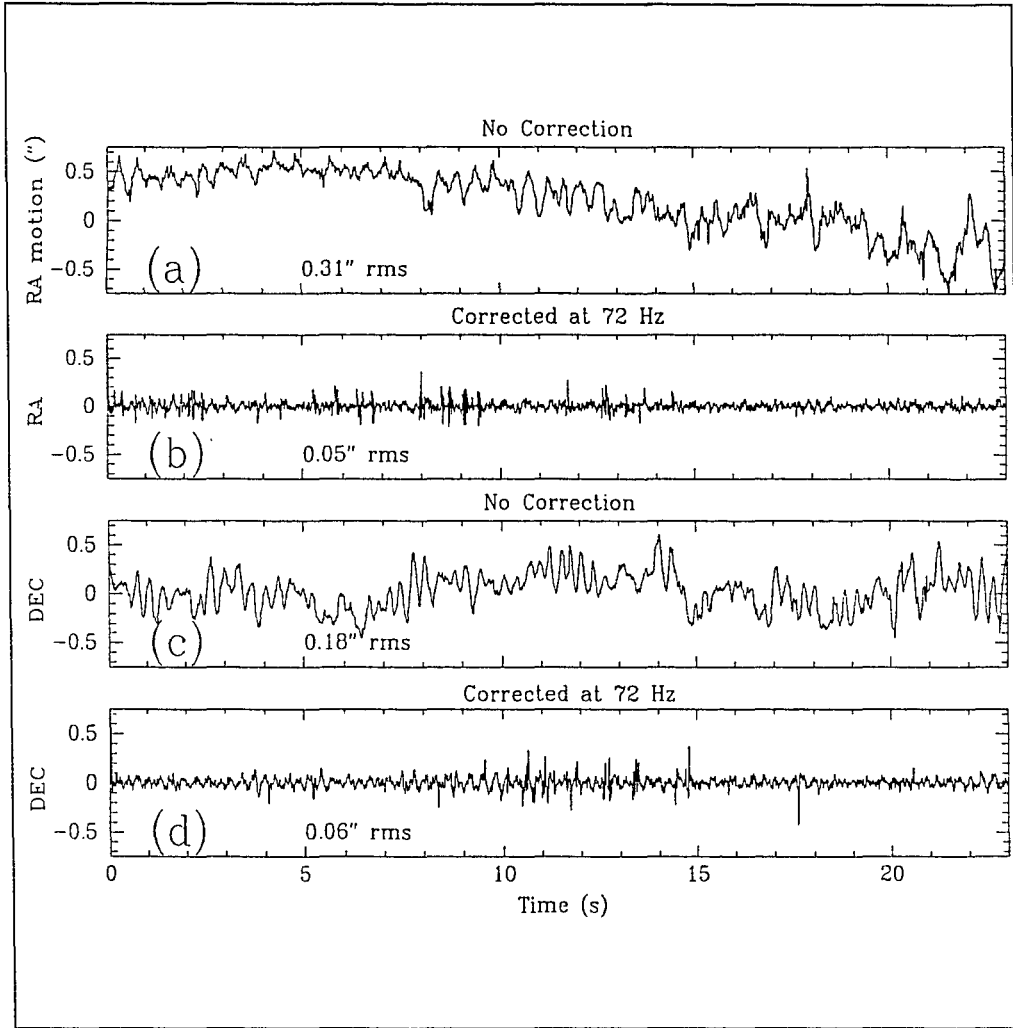


Figure 2.7: A time series plot of corrected and uncorrected image motion in right ascension, RA, (2.7a and 2.7b) and declination, DEC, (2.7c and 2.7d) during a typical 23 s interval of $D/r_0 \sim 5$ seeing (at $2.2 \mu\text{m}$). Part (a): typical uncorrected RA image motion due to seeing and telescope tracking errors. Part (b): residual RA image motion with FASTTRAC correcting for tilt variations at 72 Hz closed-loop. Note that the rms image motion is reduced by a factor of ~ 6 to only 0.05" rms. Part (c): uncorrected motion in DEC (note the resonance at 3.3 Hz caused by wind vibration). Part (d): residual image motion after tip-tilt correction at 72 Hz. Note that the rms motion has decreased by a factor of 3, to only 0.06", and that the wind induced vibrations are almost completely removed.

2.4 Performance

The data shown here was obtained with the original FASTTRAC InSb detector. It appears, from data recently taken, that the system performs with the CCD (or the new Adaptive Optics Science Camera) the same as with the old InSb. The major difference now is that fainter guide stars (R~16, K~11) can be used for guiding on.

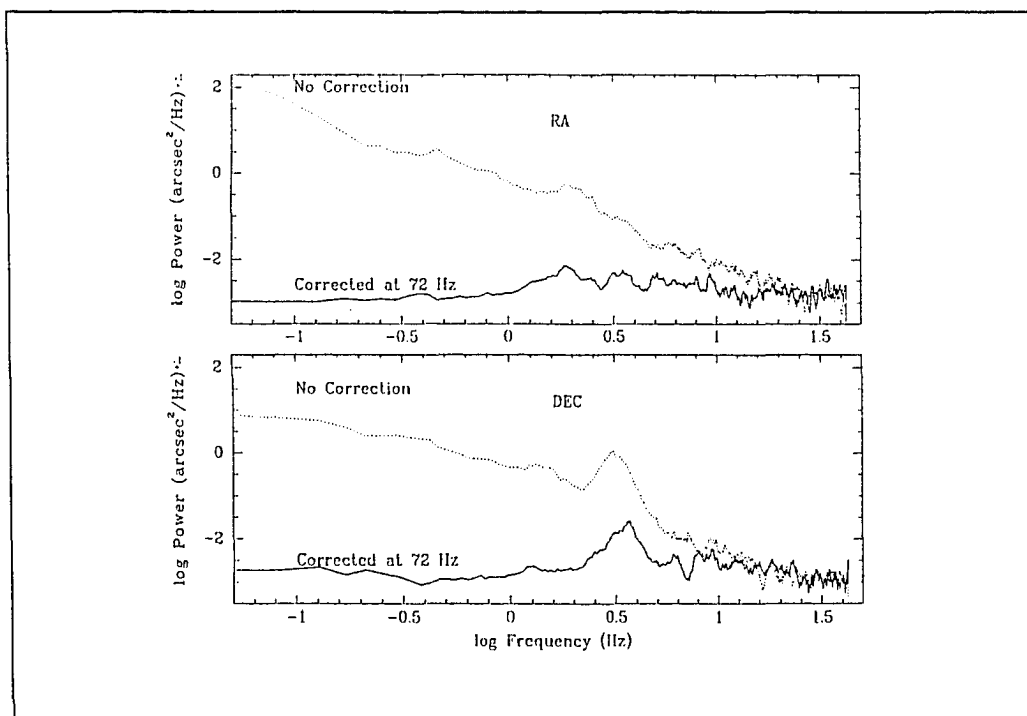


Figure 2.8: Power spectra of the corrected and uncorrected time series image motion from figure 2.7 (RA at top, DEC at bottom). The vast majority of tilt power is removed by FASTTRAC, including power in the 3.3 Hz wind-induced vibration in DEC which is reduced by over ~95%.

2.4.1 Image Stabilization

Figure 2.7 demonstrates FASTTRAC's ability to remove image motion caused by telescope tracking errors, wind buffeting, and atmospheric turbulence. During observations of κ^2 Boo ($m_K = 3$), at $2.2 \mu\text{m}$, two sequences of 2000 exposures (each 5 ms long) were obtained with the InSb sensor at a scale of $0.5''/\text{pixel}$. A 11.5 m/s wind was buffeting the telescope from the north-west. Figure 2.7a illustrates the uncorrected image motion measured in right ascension at a sampling frequency of 85 Hz. The telescope's periodic tracking error ($\sim 1''$ amplitude; 40 s period) is clearly evident. The residual rms image motion indicates that $D/r_o \sim 5$ (Martin et. al 1987). Figure 2.7b illustrates the typical degree of image stabilization achieved when FASTTRAC is enabled at a closed-loop frequency of 72 Hz (images sampled at 85 Hz as in figure 2.7a). The residual rms image motion is reduced by a factor of ~ 6 to only $0.05''$, close to the $0.02''$ PZT accuracy limit. Figures 2.7c and d show the corresponding results in the declination direction. The peak at 3.3 Hz corresponds to an assumed resonance in the telescope structure excited by the wind. However, most of this resonant motion is removed by FASTTRAC, leaving only a $0.06''$ rms residual after correction.

To further illustrate FASTTRAC's ability to remove tilt power, figure 2.8 plots power spectra of the time series data from figure 2.7. Almost all significant tilt power has been removed in both coordinates out to a frequency of ~ 20 Hz. However, due to its finite closed-loop frequency, FASTTRAC is only able to remove $\sim 95\%$ of the 3.3 Hz resonance. Hence, the residual peak at that frequency is merely an artifact of the finite 72 Hz closed loop

frequency. It is, however, reassuring that a rapidly moving massive optic can indeed *reduce* resonant power in its support spiders, instead of possibly increasing it. Also, note that FASTTRAC is able to reduce power out to a -3dB closed loop bandwidth of ~ 7 Hz which is adequate to remove almost all of the atmospheric tilt.

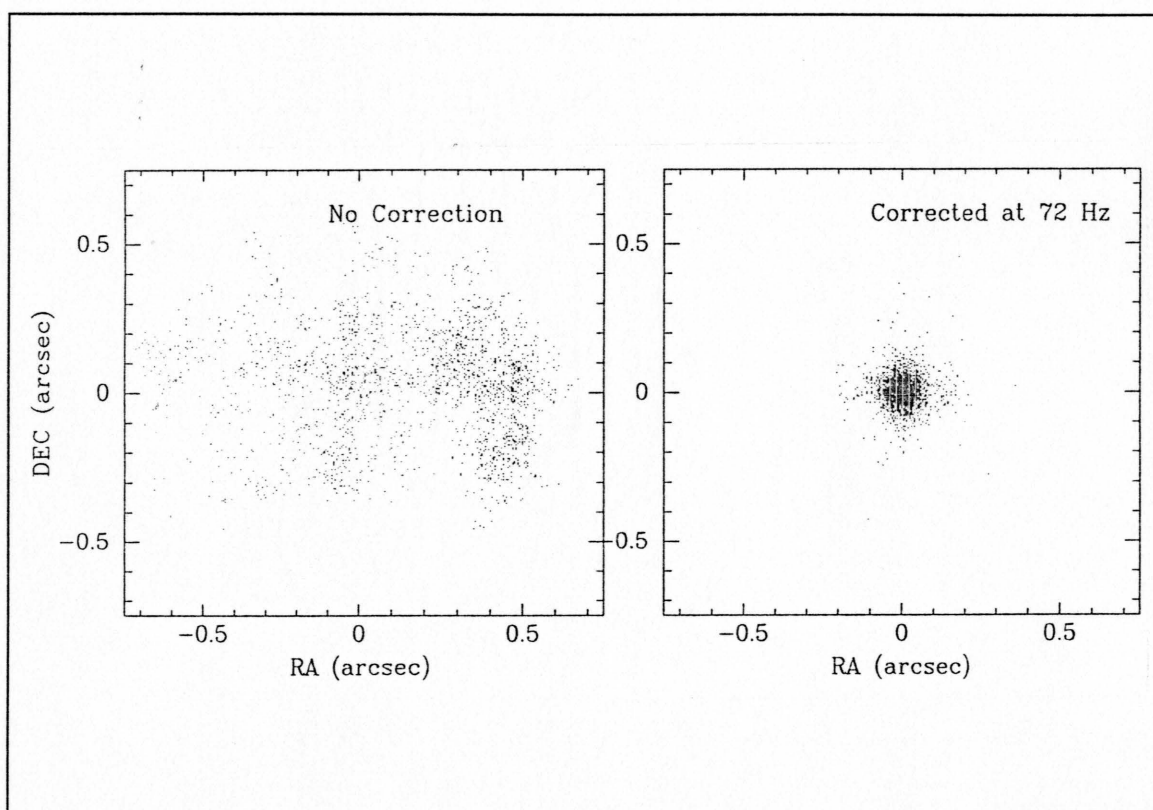


Figure 2.9: The positions of each of the 2000 individual centroids in figure 2.7. Note that FASTTRAC constrains the centroid for $\sim 80\%$ of an exposure to within $0.05''$ of the center, whereas in the uncorrected case the centroid wanders within a radius of $\sim 0.3''$.

Figure 2.9 contrasts the corrected and uncorrected positions of all 2000 individual centroids from the data of figure 2.7. Under the present conditions ($D/r_0 \sim 5$), FASTTRAC constrains $\sim 80\%$ of an integration to within $0.05''$ of the subarray center, whereas $\sim 80\%$ of

the uncorrected exposure is spread over a larger radius of $\sim 0.3''$.

FASTTRAC is also able to achieve image stability when tracking a guide star's brightest speckle in the infrared. Typically, the rms stability is limited to $0.05''$. Results are presented in section 2.4.3.

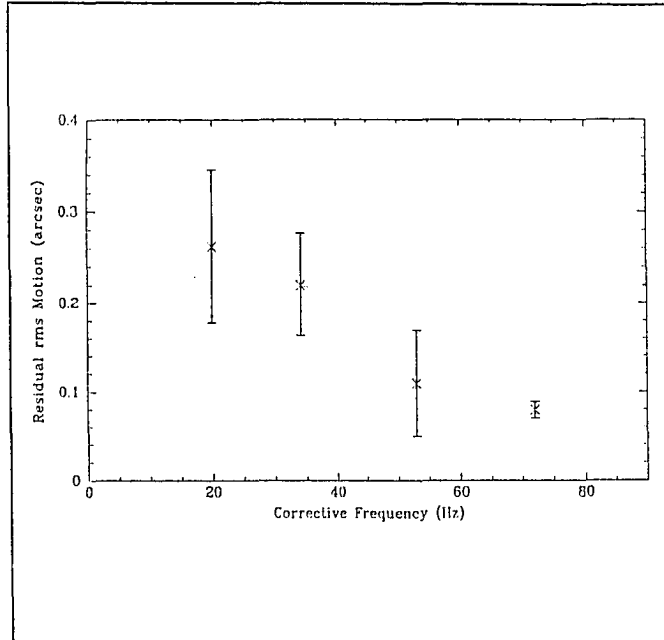


Figure 2.10: The observed residual rms image motion (in RA and DEC) as a function of closed-loop correction frequency for a night of moderate 11.5 m/s wind.

2.4.2 Required Corrective Frequency

To remove the majority of tilt power, the atmosphere must be sampled and corrected at a rate significantly higher than the characteristic frequency of the tilt fluctuations. For observations obtained during the night described in section 2.4.1, figure 2.10 illustrates the relationship between residual centroid motion (in both coordinates) and correction frequency (defined as the inverse of the maximum time required for correction; cf., figure 2.6). Only correction frequencies over ~ 60 Hz are successful at limiting the rms phase error due to residual tilt to below 1 radian^2 . This 60 Hz cut-off frequency is higher than usual due to the moderately strong 11.5 m/s wind, in agreement with predictions from the "frozen-in"

turbulence model, which predicts that tilt fluctuations will occur with a frequency of $\sim v/D$, where v is the wind speed of the dominate layer of turbulence.

It is possible to compare different sets of data (taken under different wind conditions) by scaling the applied correction frequency, f , to a wind velocity of 5 m/s (typical for Kitt Peak). Therefore,

$$f_s = f(5/v) \text{ Hz}, \quad (2.1)$$

where v is in m/s and f_s is the scaled correction frequency. From the rms image motion (θ) the residual mean square tilt error is given by

$$\langle \phi_T^2 \rangle \sim 119(D\theta/\lambda)^2 \text{ rad}^2 \quad (2.2)$$

where wavelength, λ , is in microns and D in meters. In order to have adequate tilt correction requires $\langle \phi_T^2 \rangle$ to be less than 1 rad^2 . Figure 2.11 indicates that

$$f_s \geq [27 \pm 10] \text{ Hz}, \quad (2.3)$$

if $\langle \phi_T^2 \rangle$ is to be less than 1 rad^2 for a 2.3-m aperture. In general,

$$f \geq [12.4 \pm 4.6](v/D) \text{ Hz}, \quad (2.4)$$

where f is the required closed-loop frequency to reduce $\langle \phi_T^2 \rangle$ to $\leq 1 \text{ rad}^2$. Hence, a 8-m aperture in a similar turbulence profile with a 5 m/s wind would require a closed-loop tilt correction frequency of $\sim 8 \text{ Hz}$.

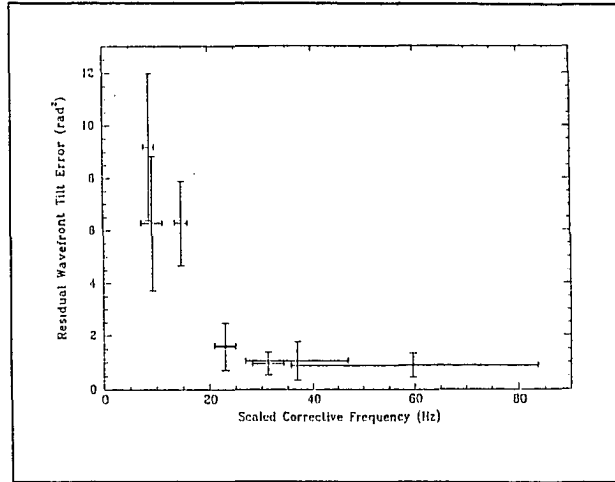


Figure 2.11: The residual mean square wavefront tilt error as a function of closed-loop frequency scaled to 5 m/s winds (which is a typical velocity for Kitt Peak).

2.4.3 Image Quality

FASTTRAC's ability to remove image motion improves image sharpness and helps retain diffraction-limited information. For example, figures 2.12 and 2.13 present the results of simply summing a time series of 2000 short guiding exposures (each 30 ms long) of the guide star LkH α -101 at $1.6 \mu\text{m}$ with the $0.065''/\text{pixel}$ scale on the InSb tracking camera. In figure 2.12a, with FASTTRAC disabled, the resulting 125 s exposure has a FWHM of $\sim 0.8''$ (in declination) and a Strehl ratio of ~ 0.05 . However, an identical exposure on the same star, obtained while tracking the brightest speckle at 16 Hz in a low $\sim 1 \text{ m/s}$ breeze (figure 2.12b), has a nearly diffraction-limited FWHM of $0.19''$ and a Strehl ratio ~ 0.14 on the InSb camera. Hence, it is possible to obtain a factor of ~ 4 improvement in

resolution when tip-tilt correcting. This improvement in resolution was also observed in simultaneously imaged field stars around LkH α -101 that were in the NICMOS3 field-of-view.

Dr. Julian Christou has kindly performed a numerical simulation of the performance of brightest speckle tracking at the 2.3-m telescope with the InSb camera in seeing conditions of $D/r_0=4$. The result, illustrated in figure 2.12d, shows that an optically perfect telescope at 1.6 μm would produce an image with a diffraction-limited FWHM of 0.15" and a Strehl ratio of 0.36. The somewhat poorer

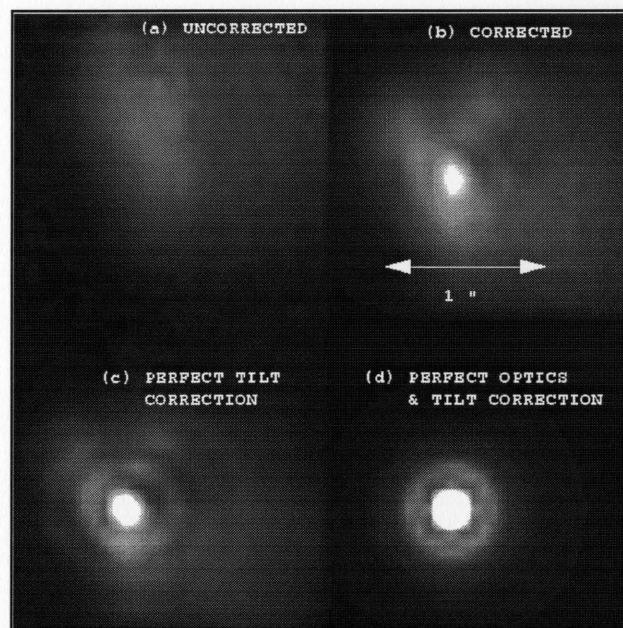


Figure 2.12: Part (a): a 125 s exposure without correction in $D/r_0 \sim 4$ seeing (the 0.065" pixels have been smoothed; north is left). This uncorrected image has a FWHM of 0.8" (in DEC) and a Strehl ratio of ~ 0.05 . Part (b): a similar image obtained by brightest speckle tracking, yielding a nearly diffraction-limited FWHM of 0.19" and a Strehl of 0.14. Part (c): a post-detection processed image that would have been produced by a perfect tip-tilt corrector with the same optical aberration (FWHM=0.15", Strehl ~ 0.20). Part (d): a theoretical $D/r_0=4$ tilt-corrected image produced by an optically perfect 2.3m telescope (FWHM=0.15", Strehl=36%) courtesy of J. Christou.

quality of the images achieved here (FWHM=0.19"; Strehl=0.14) is not solely due to residual image motion. This follows from analysis of the uncorrected image motion data. A perfect tip-tilt system should yield the same image quality as a post-detection "shift-and-add" image in which all 2000 individual exposures have been superimposed on the position of

their brightest speckle. As illustrated in figure 2.12c, a perfect tip-tilt system would have achieved a FWHM~ 0.15" and a Strehl of only 0.20. Instead, the images are degraded by static optical aberrations in the optical train, most likely defocus and collimation errors between the InSb camera and the telescope. These static aberrations appear to reduce the achieved Strehl ratio by a factor of ~2.

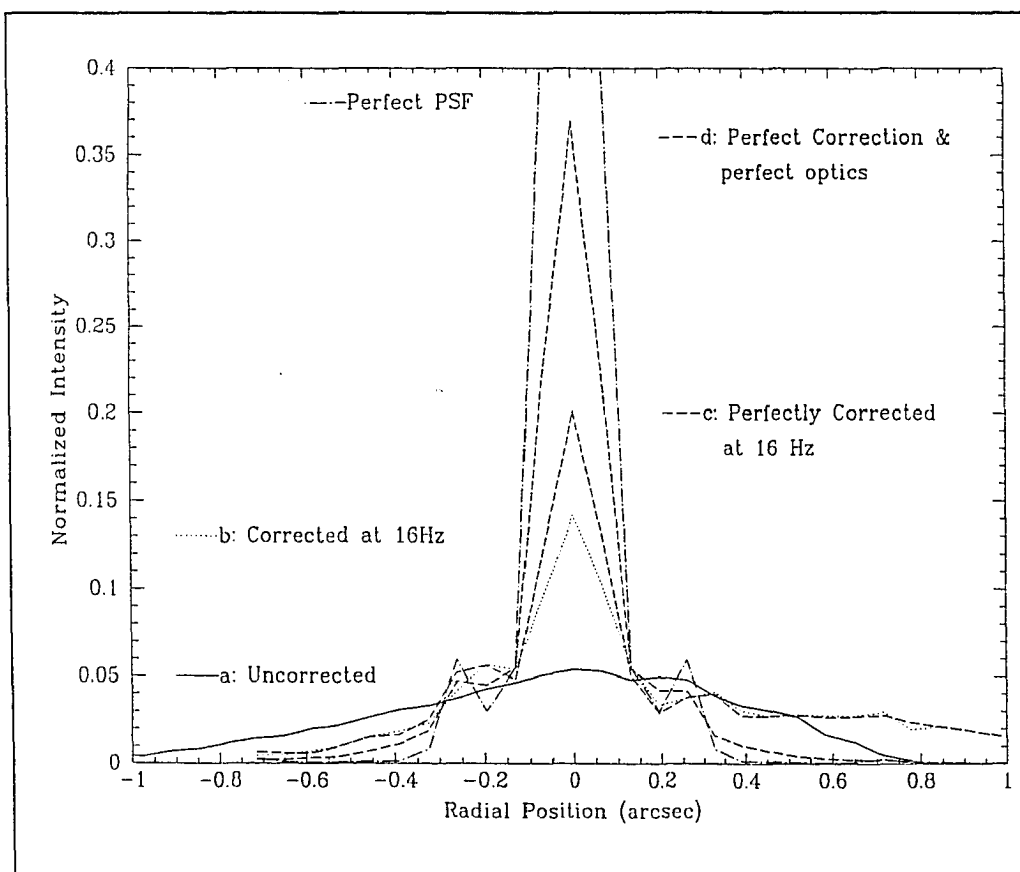


Figure 2.13: Image profiles of the four images in figure 2.12 normalized by a perfect PSF. Note the loss in Strehl due to optical aberrations.

Since figure 2.12c has a Strehl ratio of 0.20, it is apparent that FASTTRAC's small (but finite) uncorrected residual image motion of $\sim 0.06''$ limits it to ~ 0.7 of the maximum Strehl ratio possible with the present optics. However, it is important to note that FASTTRAC still gains by tracking the brightest speckle of the guide star instead of the centroid, since tracking the centroid (post-detection processed) only was found to produce a maximum Strehl of 0.16 compared to the 0.20 observed by perfect brightest pixel tracking (post-detection processed). This improvement of a factor ~ 1.3 in Strehl using brightest speckle tracking (compared to centroiding) is in agreement with the theoretical predictions (Christou 1992).

2.4.4 Long Exposure Wide Field Imaging

To demonstrate the typical improvement in wide field science images, figure 2.14 compares two 60 s exposures of the Galactic Center in the K band using the new Adaptive Optics Camera as the infrared slope sensor. For clarity only the central $6 \times 6''$ sections of these $25 \times 25''$ images are shown. Figure 2.14 (upper left-hand side) is an *uncorrected* seeing-limited image (FWHM $\sim 0.8''$, Strehl ~ 0.07 ; $D/r_0 \sim 3.5$). Figure 2.14 (upper right-hand side) is the same field corrected with FASTTRAC by guiding at 40 Hz on the brightest speckle of IRS 7 ($m_K \sim 6.7$, see figure 2.3 for the whole field). The corrected image shows a factor ~ 3 improvement in resolution and Strehl with a FWHM $\sim 0.28''$ (Strehl ~ 0.20). This is in agreement with theory (see figure 1.3) for $D/r_0 \sim 3.5$ seeing conditions. Image motion was reduced by ~ 3 times to $0.12''$ rms.

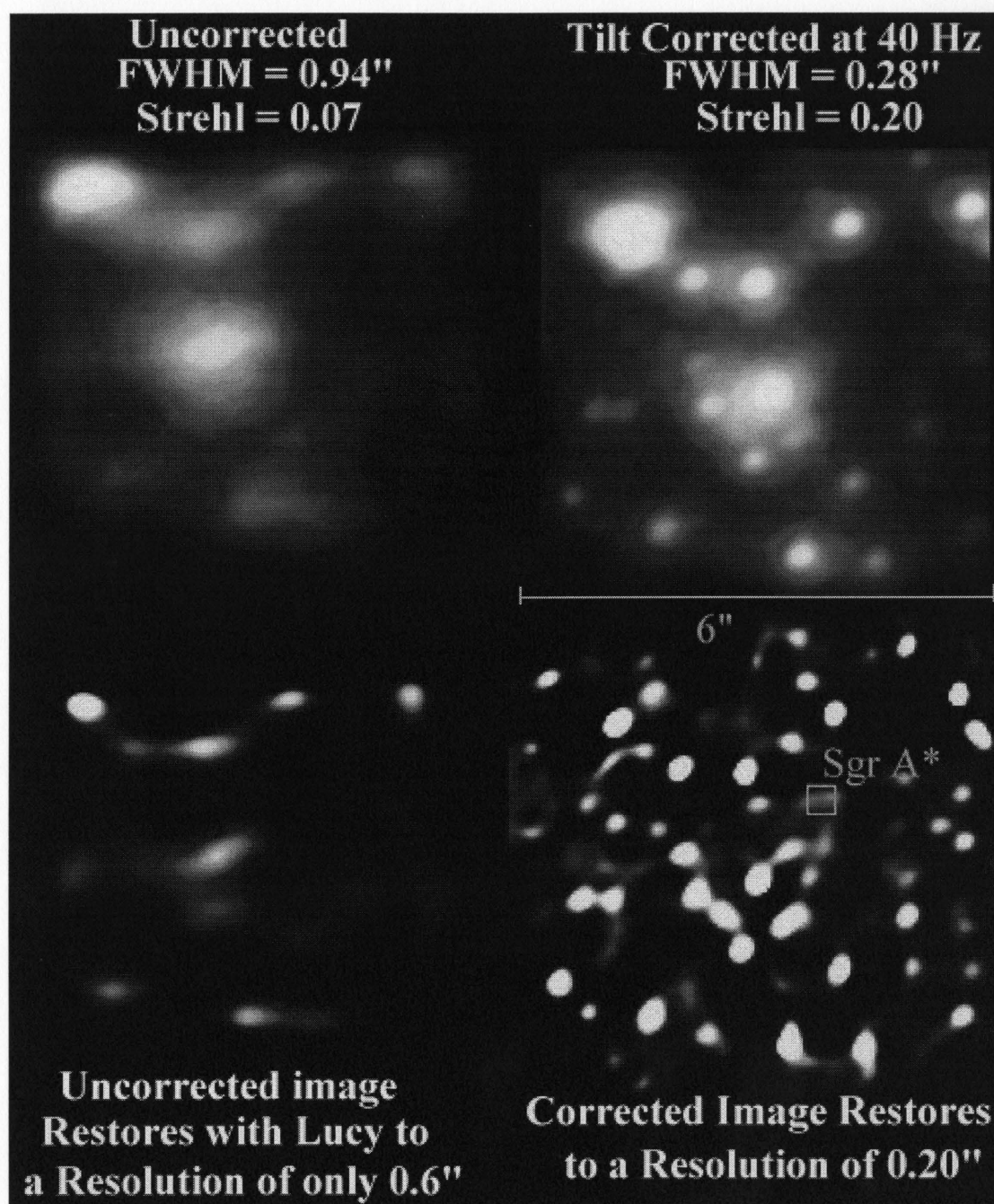


Figure 2.14: A comparison of FASTTRAC imaging of the Galactic Center without and with tilt correction (at $2.2\mu\text{m}$ at the 2.3m at a -3dB point of ~ 4 Hz). The images in the lower half of figure 2.14 are Lucy restored images of those above.

2.4.5 Post-Detection Processing: Lucy Deconvolution

The Lucy deconvolution algorithm has been found to be reliable for restoring diffraction-limited morphologies in partially compensated AO images with significant Strehl ratios (Roddier et. al 1996). Therefore, the Lucy deconvolution algorithm (as implemented in the IRAF RESTORE package) will be used here. The lower sections of figure 2.14 show how the "off" and "on" images deconvolve. Since the "on" or corrected image has a significant amount of power in a diffraction-limited core (see figure 2.15) it is possible to restore the image to diffraction-limit of the telescope (0.2"). However, the "off" or

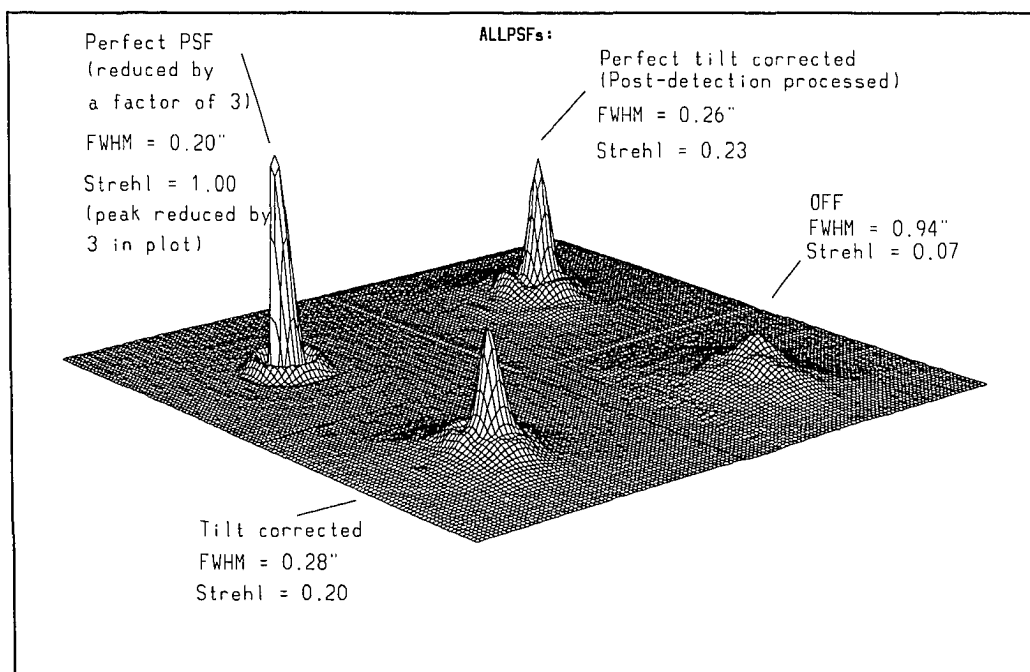


Figure 2.15: A comparison between no tip-tilt, tip-tilt correction, perfect tip-tilt, and a theoretically perfect PSF (20s exposures at the Galactic Center, at 2.5 airmasses). This data was taken by the Adaptive Optics Camera acting as its own tilt sensor at 40Hz with the FASTTRAC tip-tilt secondary at the 2.3m telescope ($r_0=66\text{cm}$, at $2.2\mu\text{m}$).

uncorrected image on the left hand side of figure 2.14 does not have enough signal at the higher spatial frequencies to restore structures sharper than $\sim 0.6''$ in size. Hence, it is apparent that post-detection processing such as Lucy deconvolution can restore images to the diffraction-limit of the telescope if they have a significant amount of power in a diffraction-limited core. Since such intermediate Strehl images are typically produced by partial AO systems (such as tip-tilt), it is clear post-detection processing (such as Lucy deconvolution) should be commonly employed to obtain diffraction-limited resolutions. Another advantage to Lucy restored images is that faint sources that would otherwise be lost in the wings of nearby bright sources can be easily recovered (such as the "bar" at the position of Sgr A* in figure 2.14).

In general, intermediate Strehl images should be iterated by Lucy until the diffraction-limit is reached on the objects of interest in the frame. Typically this requires many iterations to have faint point sources converge (for example 700 Lucy iterations were used in figure 2.14). Bright point sources (or extended objects) will converge to the diffraction-limit after only 10-50 iterations.

However, deconvolution can produce incorrect photometric and morphological results in cases where there is a mismatch between the true PSF and the "model" PSF being used by Lucy. Therefore, any deconvolved image is only as good as the PSF that was used to reconstruct it. The best case is when the PSF can be directly sampled from an isolated, bright star in the image itself (the guide star for example). If there is not a good PSF star in the science field then a bright PSF star (similar to the guide star) should be observed before

and after the science images with the same exposure time and the same AO correction parameters. Another fundamental problem with AO images is that anisoplanatic effects change the PSF as one goes farther out from the guide star. At the moment there is no solution to this problem beyond only deconvolving small areas of the science images that share a common PSF.

2.5 Conclusions

A tip-tilt secondary mirror system for high resolution imaging in the near-infrared has been developed. This system, FASTTRAC, utilizes infrared guide stars as faint as $K=11$ to correct a $25 \times 25''$ field at closed-loop frequencies of ≤ 50 Hz. FASTTRAC also utilizes a low read noise CCD to track faint $R \sim 16$ guide stars at 50 Hz. At these frequencies the majority of tilt power due to tracking errors, wind buffeting, and atmospheric turbulence is removed. The residual tilt phase error of the wavefront is reduced to $\leq 1 \text{ rad}^2$, yielding images with nearly diffraction-limited FWHM when $D/r_0 \leq 5$. In poorer seeing conditions, $5 \leq D/r_0 \leq 10$, an improvement of ~ 2 in resolution is common. FASTTRAC has obtained 125 s exposures at H ($1.6 \mu\text{m}$) in $D/r_0 \sim 4$ seeing conditions producing a factor of 4 improvement in resolution to $0.19''$ FWHM with a Strehl ratio of 0.13. These results from FASTTRAC indicate that tip-tilt secondaries on large telescopes can obtain diffraction-limited imaging in the infrared.

CHAPTER 3

FASTTRAC IMAGING OF THE BLACK HOLE CANDIDATE SAGITTARIUS A*

This chapter describes some of the high resolution imaging that FASTTRAC has accomplished at the Galactic Center. In particular, the nature of the infrared source coincident with the unique radio source Sgr A* will be discussed.

3.1 Introduction

Sgr A* is a unique, non-thermal radio source at the center of the Galaxy. Its radio position lies within $\sim 1''$ of the Galactic dynamical center (Lacy et al. 1993). Moreover, Sgr A*'s proper motion with respect to the central cluster appears to be near zero (Backer & Sramek 1987). Since these are among the dynamical characteristics expected of a massive object, it is commonly thought that this compact radio source (< 3.3 AU at 43 GHz; Backer et al. 1993) may be a massive central black hole (cf., Lynden-Bell & Rees 1971). Confirming indications of a large central mass come from studies of the nearby gas dynamics ($\sim 1.6 \times 10^6 M_{\odot}$; e.g., Serabyn et al. 1988) and stellar motions ($\sim 2 \times 10^6 M_{\odot}$; McGinn et al. 1989; Sellgren et al. 1990; Haller et al. 1996).

The lack of a strong Sgr A* detection in the near-infrared, however, has led to the conclusion that no large accretion disk could be present (Rieke & Lebofsky 1982; Lacy, Townes, & Hollenbach 1982; Allen & Sanders 1986; Rieke, Rieke, & Paul 1989). Recently,

aided by better infrared detectors, several investigators (Eckart et al. 1992, 1993; Close et al. 1992; Herbst, Beckwith, & Shure 1993) have reported the detection of a relatively faint infrared counterpart to Sgr A*. In particular Eckart et al. (1993) shifted and added many short (0.5-1.0 s) exposures of the Galactic Center (centering the position of IRS 7) and then deconvolved the final image to a resolution of 0.15". These final deconvolved images contained a $K=12.0\pm0.5$ and $H=13.9\pm0.5$ infrared source (magnitudes integrated over 0.5") within 0.15" of Sgr A*'s position.

This chapter reports new, near-infrared (1.2-2.2 μm) observations of the Sgr A* infrared source. The previously observed K and H magnitudes by Eckart et al. (1993) are confirmed and the first J detection of the source is presented. The possibility that the source is variable on the time scale of years is examined. It is also confirmed (for the first time) that the Sgr A* infrared source is located in a $\sim 0.5''$ "bar" running from East to West. This morphology was first detected by Eckart et al. (1993).

If Sgr A* is a massive black hole, it is expected (Melia & Lamb 1994; Hollywood et al. 1995) that the infrared source could be variable on time scales of ~ 8 min. This time scale corresponds to the characteristic Keplerian orbital period at the inner edge of an accretion disk surrounding a $\sim 10^6 M_{\odot}$ black hole. Such rapid variability is searched for by a Fourier analysis of the observed flux timeseries. The observed fluxes from the infrared source are also compared to those predicted by a simple $\sim 10^6 M_{\odot}$ black hole accretion disk model.

3.2 Observations

Since FASTTRAC (in its original configuration) was the first adaptive system to incorporate a high speed *infrared* camera (McCarthy, McLeod, & Barlow 1990) to track the centroid of a guide star, it was an ideal instrument to image the Galactic Center (since there are no bright nearby visible guide stars due to the high extinction towards the Center). In this application the bright infrared source IRS7 ($m_K=6.7$; spectral type M2 Ia), located only 6" north of Sgr A*, served as an excellent guide star. This enabled FASTTRAC to obtain the first real-time tip-tilt corrected images of the Galactic Center. The advantage of such images is that they achieve high angular resolution and significant Strehl ratios.

On two consecutive nights (May 31 and June 1, 1993) FASTTRAC imaged the central 54x54" of the Galaxy at a 0.21"/pixel scale on the original NICMOS3 256x256 infrared array (Rieke et al. 1993). These nights were photometric and yielded excellent images ($\langle \text{FWHM} \rangle \sim 0.55''$) although the airmass to the Galactic Center is >2.0 from Kitt Peak. Without FASTTRAC the seeing-limited resolution was 1.0-1.5" at these airmasses.

On the first night (May 31), FASTTRAC obtained 150 exposures of 10 s each in the H band (1.65 μm) followed by an identical sequence at K (2.22 μm) over a total period of 130 min. On the following night 150 10 s images at K (over a 60 min period) were followed by eight 180 s images at J (1.25 μm). Two off-source sky calibration images were taken after every set of five on-source images.

On the night of September 3, 1995 FASTTRAC utilized the new Adaptive Optics Science Camera (at its 0.10"/pixel scale) to obtain an excellent 60s exposure with a FWHM

of 0.28" and a Strehl of 0.20. This image was obtained by use of the unique ability of the Adaptive Optics Science Camera to readout a single 32x32 subarray to track the brightest speckle of IRS 7 and integrate on the rest of the 25x25" field around the subarray (as illustrated in figure 2.3). Although this excellent single image does not help set constraints on the short term variability of Sgr A* it does help constrain the long term variations and (most importantly) the morphology of the region. For clarity this most recent image will only be referred to in sections 3.3.3 and 3.5.1.

3.3 Photometric Measurements and Applications

3.3.1 Reductions

All images were reduced with standard corrections and calibrations for sky background, dark current, and flat-fielding. Off-source sky frames were medianed together to give both a sky frame and a flat frame. An infrared source was visible at Sgr A*'s position in the best individual images (cf., figure 3.1a). To accomplish accurate photometry of the Sgr A* source in this crowded field the photometry package DAOPHOT was used, which is optimized for photometry in such fields (Stetson 1987). Four isolated point sources near Sgr A* were fit to model the point spread function (PSF) for each image. The point sources utilized were IRS 9, 18, 19, and a source 4.5" east of IRS 9 (see Becklin and Neugebauer (1975) for source locations). To increase the accuracy of the PSF all contaminating sources

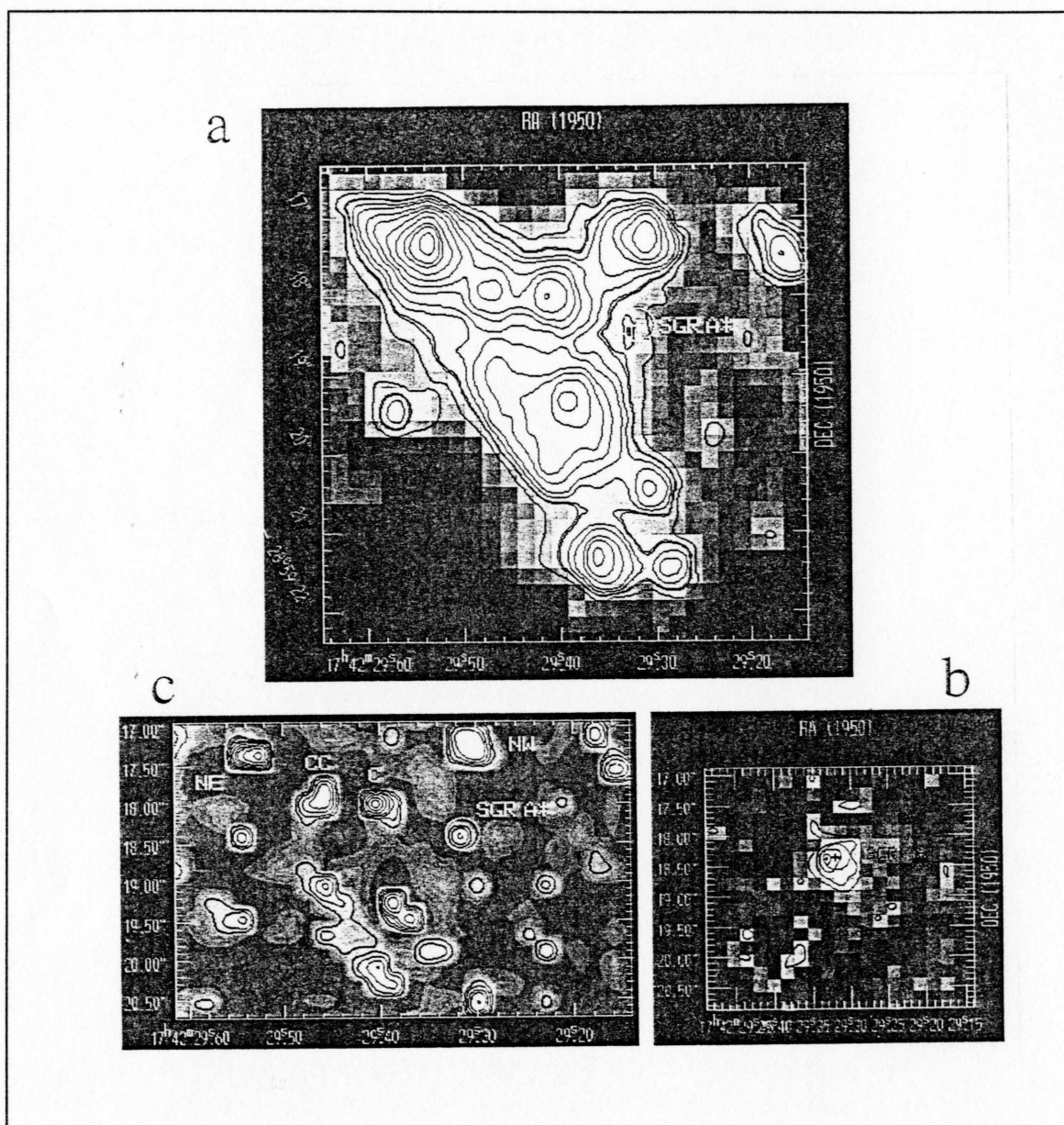


Figure 3.1a: A typical 10s H ($1.6\mu\text{m}$) image taken the first night. The FWHM is $\sim 0.54''$, and the contour levels are 8 ($\sim 3\sigma$), 9.8, 10.3, 12, 14, 18, 22, 30, 41, 56, 68, and 90% of IRS 16 NE's peak flux. The cross marks the position of Sgr A*. The uncertainty in this position ($\pm 0.2''$) is denoted by the white error circle. **Figure 3.1b:** The same image as in (a) after DAOPHOT has fit and subtracted the surrounding stars leaving the Sgr A* source. Contour levels are at 6, 7, 8 ($\sim 3\sigma$), 9, and 10% of IRS 16 NE's peak flux. **Figure 3.1c:** The deconvolution of image (a) to a FWHM $\sim 0.2''$ (as described in section 3.3.1). Contour levels are 2.5, 4.5 ($\sim 3\sigma$), 8, 12, 20, 30, 40, 60, and 90% of IRS 16 NE's peak flux. The image pixels have been linearly smoothed. The positions of IRS 16 NE, CC, C, and NW are indicated.

within 5" were removed around these PSF stars. Then, for the full frame, the brightest ($K < 11.5$) sources were fitted with this model PSF and subtracted, followed by a similar subtraction of the remaining faint point sources around the Sgr A* source (cf., figure 3.1b). To obtain the highest accuracy sky level, all pixels within a two pixel radius of intensity $> \pm 3 \sigma$ were rejected in the fit of the sky background around each star.

In the poorer quality images ($\text{FWHM} \geq 0.8''$) DAOPHOT could not reliably find a point source near the position of Sgr A*. Therefore only the sharpest 40 images at H ($0.48 < \text{FWHM} < 0.64''$, see figure 3.1a) and 40 images at K ($0.55 < \text{FWHM} < 0.69''$, see figure 3.2) were selected from the first night. On the second night, the seeing was worse and only 33 K images ($0.58 < \text{FWHM} < 0.73''$) and all eight J images ($\text{FWHM} \sim 0.7''$, see figure 3.3) were selected.

The photometric standard used for calibration was IRS 9. The brighter star IRS 7 could not be utilized since it served as the guide star and was picked-off by

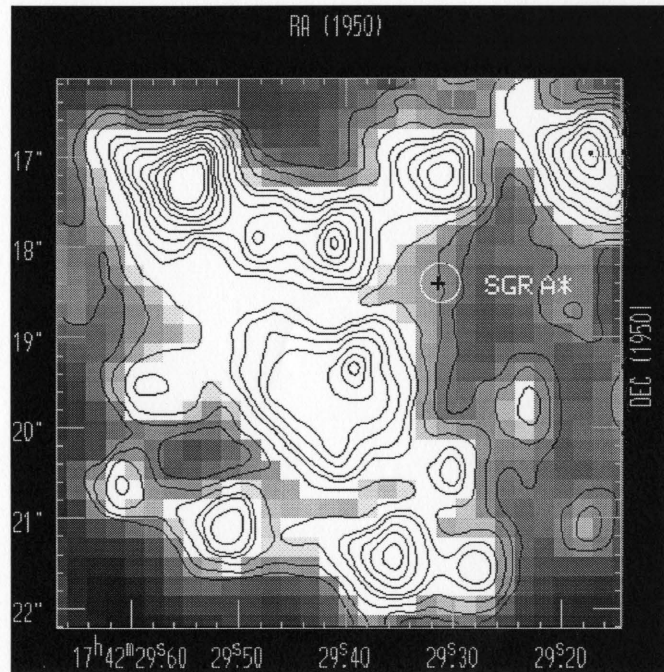


Figure 3.2: A summed 1 min exposure at K taken on the first night ($\text{FWHM} = 0.6''$). Contour levels are 7.5, 9 ($\sim 3\sigma$), 12, 16, 18, 23, 28, 36, 44, 52, 65, 78% of IRS 16 NE's peak flux.

eliminate fluctuations due to changes in atmospheric transmission, each frame was

normalized so that the total flux from the PSF stars remained constant. The resulting average absolute differences for IRS 16 NW, C, and NE compared to previously published magnitudes (DePoy & Sharp 1991) were 0.03 mag (K), 0.06 mag (H), and 0.05 mag (J).

In all 121 selected images

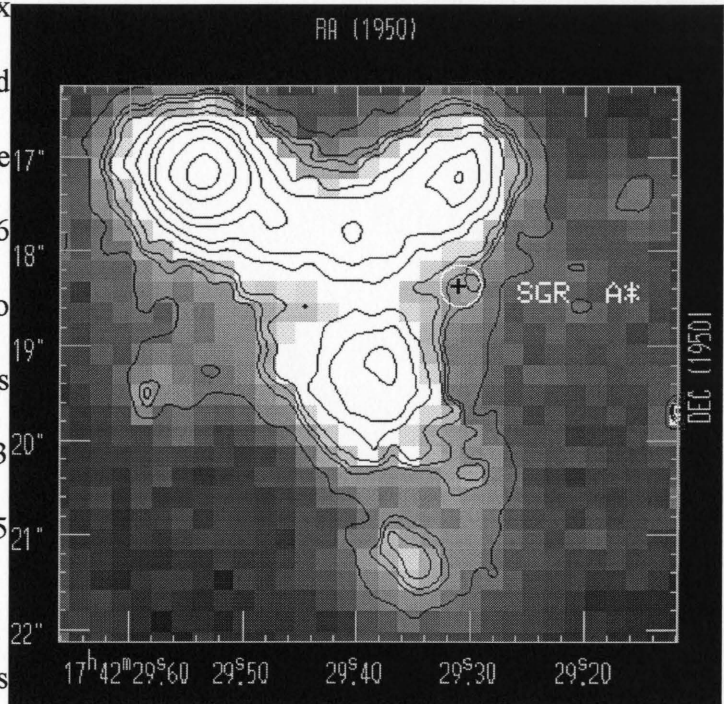


Figure 3.3: A summed 21 min exposure at J (FWHM=0.7''). Contour levels are 19, 24, 26 ($\sim 3\sigma$), 28, 34, 40, 49, 60, 75, 95% of IRS 16 NE's peak flux.

$\pm 0.2''$ (Herbst et al. 1993) infrared positional error of Sgr A* (cf., figure 3.1). To ensure that the magnitudes of this source were not biased by improper photometry, all the major photometric parameters were examined for erroneous correlations with Sgr A*'s magnitude. No significant correlations were found between this magnitude and sky level, DEC position, RA position, or FWHM in all 121 images. From the possible correlations in the H and K data sets the largest was between Sgr A*'s H magnitude and its RA position, which still had a $p=80\%$ probability of not being correlated. The K data from the second night had its most significant correlation between Sgr A*'s magnitude and its DEC position, with a $p=60\%$ probability of no correlation. Hence none of the correlations was significant since all of the

probabilities were above the significance level of $p=5\%$. The lack of any significant correlations indicates that there are no obvious systematic errors in the flux calculation for Sgr A* by DAOPHOT in this crowded field.

The average magnitudes (weighted by photometric error) for Sgr A* are: $K=12.1\pm0.3$, $H=13.7\pm0.3$, and $J=16.6\pm0.4$ mag. The errors in these photometric averages are dominated by the absolute calibration error. To independently check the DAOPHOT photometry, six H and K frames were deconvolved (to a FWHM $\sim0.2''$) with an iterative deconvolution algorithm (Jefferies & Christou 1993). The resulting images confirm a source within the positional error of Sgr A* (cf., figure 3.1c), with $K=12.2$ and $H=13.8$, well within 1σ of the DAOPHOT magnitudes.

3.3.2 Is This Infrared Source Sgr A*?

Recently Tamblyn et al. (1996) utilized FASTTRAC to image the Galactic Center at high resolution through a narrow band filter centered at the HeI ($2.06\mu\text{m}$) emission line. They detected a tentative emission source coincident with the infrared source in a 35 minute exposure. Therefore, the infrared source may have an effective surface temperature of $T > 1 \times 10^4$ K, since it appears to be a HeI emission source.

The K, H, and J fluxes are best fit (minimized reduced chi squared, χ_v^2) by the Galactic Center extinction law (Rieke et al. 1989) with $A_v=27.4\pm3.5$ mag for $T > 1 \times 10^4$ K. Since $A_v \sim 27$ is the estimated local value of extinction around Sgr A* (DePoy & Sharp 1991; Herbst et al. 1993), it appears that this source is inside the Galactic Center region near IRS

16 C (DePoy & Sharp 1991) and so is likely within the high density central cluster.

In addition the source is also positionally coincident with Sgr A*. The mean value of Sgr A*'s radio position, as given by Rosa et al. (1992), is RA=17:42:29.316 and DEC=-28:59:18.38 [1950]. This mean position results from high resolution radio observations made by Backer & Sramek (1982), and Yusef-Zadeh et al. (1990). Following Herbst et al. (1993), it has been adopted that the corresponding infrared position of Sgr A* is $1.11 \pm 0.2''$ S and $0.05 \pm 0.2''$ E from IRS16 NW. Therefore, the average H and K position of the observed source is $0.21 \pm 0.24''$ S and $0.01 \pm 0.20''$ E of Sgr A*. Hence, the source is offset $0.2 \pm 0.3''$ from Sgr A*'s position.

The positional error in the observed source's offset is dominated by the $\pm 0.2''$ systematic uncertainty between the infrared and radio coordinate grids at the Galactic Center (cf. Forrest et al. 1986). Hence, the identification of this source as Sgr A* can only be tentative until the positional uncertainty between the infrared and radio coordinates for Sgr A* is further reduced.

3.3.3 Is Sgr A* Variable on Time Scales of a Year?

The infrared source may have recently increased in luminosity. The detection of a K=12.1, H=13.7 source agrees with Eckart et al.'s (1993) recent measurements (integrated over a comparable $0.5''$) of a $K=12.0 \pm 0.5$ (March 1992) and $H=13.9 \pm 0.5$ (August 1992) source within $0.15''$ of Sgr A*'s position. However, in September of 1989, DePoy and Sharp (1991) did *not* observe an infrared counterpart to Sgr A* with a similar ($\sim 0.5''$) resolution.

Moreover, they placed a $\sim 3\sigma$ upper limit to Sgr A* of $K \geq 13.5$, $H \geq 14.5$, and $J \geq 18$. Therefore, these observations reported here are $\sim 10\sigma$ more luminous than DePoy and Sharp's upper limit. *If* there are no systematic errors in comparing the photometry, then the flux from this source may have significantly increased over a ~ 2.5 yr period.

The possibility of a recent increase in flux was suggested by Herbst et al. (1993). In 0.5" seeing (in May 1991) they measured a $K=14.5$ point source 0.07" N and 0.04" W of the source observed here. This is 2.5 magnitudes fainter than Eckart et al.'s March 1992 detection. If this is the same object and if the photometry is compatible, then an increase in flux by a factor of ~ 10 over a period of ~ 1 yr is required.

Such an increase in flux may be possible if the source represents emission from an accretion disk. For example, Ruffert and Melia (1994) have carried out three-dimensional hydrodynamical simulations of the Bondi-Hoyle accretion of a uniform gas flowing past a $1 \times 10^6 M_{\odot}$ black hole. They find that fluctuations in the accretion pattern produce an infall with a finite, though variable, specific angular momentum that changes in magnitude and sign on a time scale of several years, leading to the occasional flip from prograde to retrograde rotation of the accretion disk. Therefore infrared luminosity fluctuations over the observed time scale of about one year might be expected as Sgr A*'s disk changes in size and accretion rate.

On June 20, 1994 the K flux from Sgr A* was remeasured and found to be 0.3 ± 0.5 mag fainter at K. This measurement was obtained from nine images taken with the "original" FASTTRAC configuration. These images had FWHM $\sim 0.6''$ each. Using the data reduction

procedure outlined in §3.3.1 a $K=12.4\pm0.4$ point source at the Sgr A* position was detected. Since this flux is within $\sim 1\sigma$ of the previous measurements it appears that the infrared luminosity of the object has not changed significantly from June 1993 to June 1994.

The most recent image of the Galactic Center (taken on September 3, 1995) also

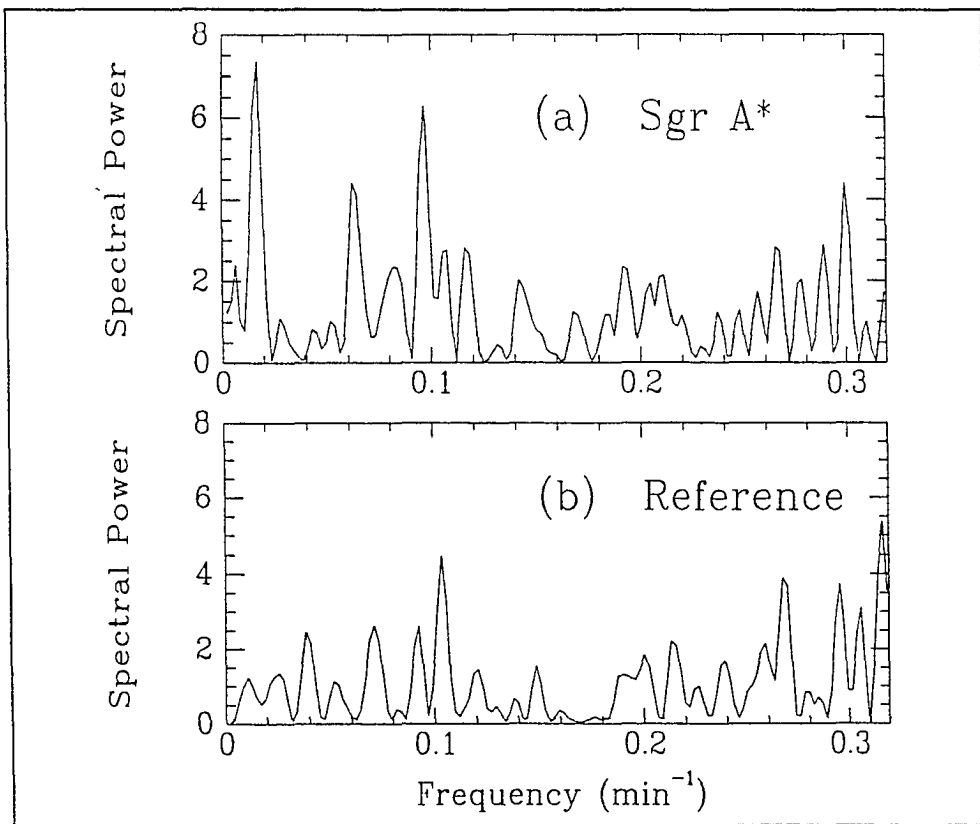


Figure 3.4a: A normalized periodogram of the flux timeseries of the 80 H and K measurements of Sgr A* from the first night. **Figure 3.4b:** A periodogram (with the same normalization) for a nearby reference star. Note that the 0.9σ peak at 9.7 min indicates that the 1.8σ peak at 10.4 min (in figure 3.4a) may be due to systematic effects.

showed that in a 0.5" aperture the flux from the 0.5" "bar" was unchanged at $K=12.21\pm0.21$. Therefore, in agreement with Eckart (1995), no sign of significant long-period luminosity changes from the Sgr A* source from June 1993 to Sept 1995 is observed.

3.4 Short Time Scale Variability

To search for periodic signals in the flux timeseries from Sgr A*, a Fourier analysis technique was employed to calculate periodograms. These periodograms were produced by the Lomb-Scargle method as modified by Press and Rybicki (1989). This method is quite powerful for finding weak periodic signals in noisy unevenly sampled timeseries data. In addition the technique provides a significance estimate for the strongest periodic signal found.

The 40 H fluxes measured for Sgr A* were scaled up to the mean K flux by multiplication by the ratio of the H and K means. The DC component of the resulting 130 min timeseries was subtracted. The Lomb-Scargle normalized (unity average power) periodogram was then calculated (see figure 3.4a), and the significance of the major peak estimated by the method of Press and Rybicki (1989). The 2.2σ peak at a period of 54 min in figure 3.4a may be real but a longer data set is required to be certain. The 130 min sampled (at ~ 1.5 min intervals) allows for periods only in the range of ~ 30 -3 min to be detected with certainty.

The only other possibly significant feature in figure 3.4a is a 1.8σ peak at 10.4 min. In the flux timeseries data there is indeed evidence of a $30\pm 15\%$ peak to peak pulse with a

10.4 min period. This pulse has been modeled in detail by Hollywood et al. 1995 who find that it is very similar to what might be expected from a hotspot on an accretion disk around a million solar mass black hole. It is also interesting to note that the 33 K measurements from the second night show evidence of a somewhat stronger 2σ peak at 8.0 min (see figure 3.5a) which is close to the 10.4 min period observed the previous night.

To check for any erroneous periodicities in the reduction, four stars near Sgr A* (K~10-12 mag) were also examined. Periodogram peaks of $\sim 0.5\sigma$ were observed on average, and no significant (3σ) periodicities were found. Of the four stars one in particular, located only $\sim 3''$ S and $\sim 1''$ W of Sgr A*, had a similar magnitude (K~11.9) and photometric errors (10-15%) as Sgr A*. The identically normalized periodogram of this reference star is shown in figures 3.4b and 3.5b. The periodogram in figure 3.4b indicates a 9.7 min (0.9σ) peak which has a $\sim 37\%$ chance of being due to random noise. The strength of this peak is not significantly different from the 10.4 min peak observed for Sgr A*. This implies that the 10.4 min period may be due to systematic error, and so should be viewed with skepticism.

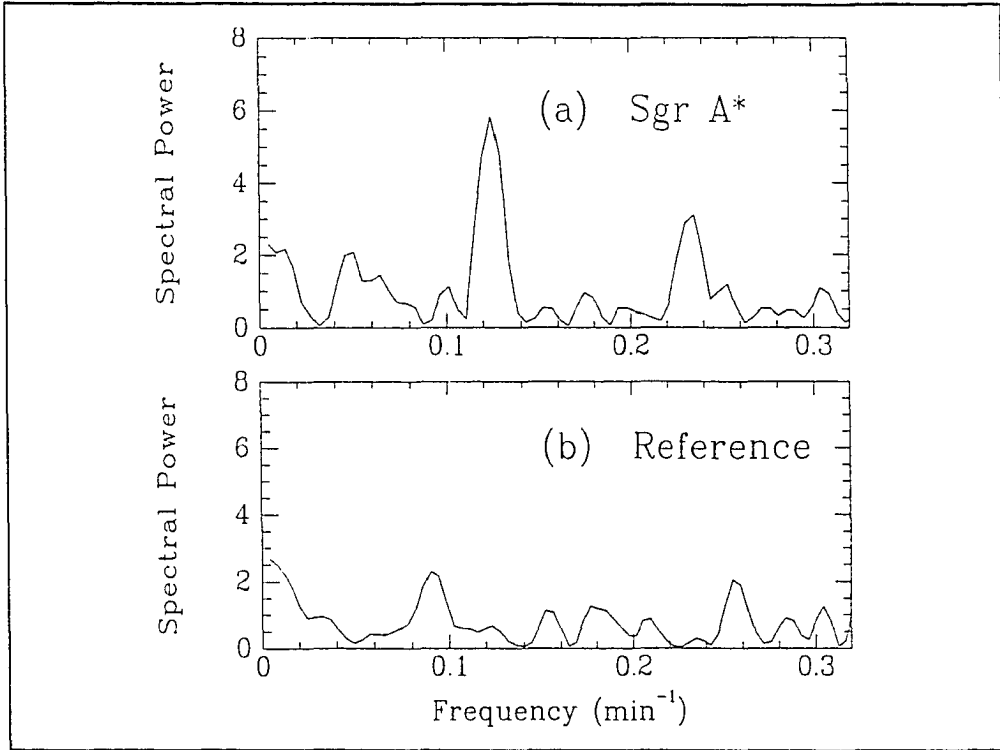


Figure 3.5a: A normalized periodogram of the 33 K fluxes from Sgr A* taken the second night; note the 2σ peak at 8.0 min. **Figure 3.5b:** A periodogram for the reference star.

Based on simulations of data with the same timeseries spacing and similar noise levels ($\text{RMS} \approx 31\%$), it is estimated that a real periodic signal from Sgr A* of peak to peak amplitude $\geq 50\%$ should have been detected at the 3σ level. Hence, one may conclude that there is no periodic signal of amplitude $\geq 50\%$ from the infrared source in the range of 3-30 min periods. The unambiguous detection of weaker signals will require photometric data with a RMS below the 31% achieved here.

A field as crowded as that around Sgr A* requires higher resolution (unprocessed $\text{FWHM} < 0.2''$) images with constant well determined PSF's to achieve accurate ($\leq 5\%$)

photometry on a K=12 source. This accurate photometry, when coupled with hundreds of consecutive measurements ($\sim 300/\text{hr}$), should allow a rapid periodic signal of amplitude $\geq 5\%$ to be detected at the 3σ level. This scientifically interesting detection limit could be achieved in the near future (1997) with the HST near infrared camera (mentioned in §1.4) or perhaps with a laser guide star AO system.

3.5 Discussion

From the dynamical arguments briefly mentioned in the introduction it seems possible that Sgr A* may be a $\sim 10^6 M_\odot$ black hole. Moreover, it is possible to check if the observed fluxes match what is expected from a million solar mass black hole's accretion disk. Since Sgr A* appears to have a sub-Eddington accretion rate, the accretion disk can be approximated as thin and Newtonian with a temperature distribution with radius R given by

$$T(R) = \left[\frac{3\alpha G M \dot{M}}{8\pi \sigma R^3} \left(1 - \sqrt{\frac{3r_g}{R}} \right) \right]^{\frac{1}{4}} \quad (3.1)$$

where $\alpha = 1 - (3r_g/R)^{1/2}$ correctly takes into account the fact that the dissipation rate goes to zero as the plasma approaches the inner edge of the accretion disk at three Schwarzschild radii ($3r_g$) (Shapiro, Lightman, & Eardley 1976). Since the disk is expected to be optically thick, its emission has been approximated as a sum of black bodies. To solve for the luminosity density all the isothermal rings in the disk are integrated over. The luminosity

density (L_ν , in units of $\text{erg s}^{-1} \text{Hz}^{-1}$) is then

$$L_\nu = \frac{16\pi^2 h \nu^3 \cos(i)}{c^2} \int_{3r_g}^{R_{\text{out}}} \frac{R dR}{e^{\left(\frac{h\nu}{kT(R)}\right)} - 1} \quad (3.2)$$

where the disk inclination angle (i) is unknown. The mass accretion rate (\dot{M}) is set by the amount of Galactic Center gas gravitationally captured by Sgr A*. Based on the Galactic Center wind characteristics it is estimated that $\dot{M} \sim 4 \times 10^{21} \text{g s}^{-1}$ (Melia 1992). Thus, from equation (3.2), a thin disk inclined from $i=0-88^\circ$ closely fits the observed infrared fluxes for a mass range of $M=(0.5-2) \times 10^6 M_\odot$

respectively. Hence a $M \sim 1 \times 10^6 M_\odot$ black hole's accretion disk fits the observed near infrared fluxes with an inclination of $i=80^\circ$ (see figure 3.6). The outer edge of the disk, R_{out} is assumed to be $9r_g$ since these values of \dot{M} and R_{out} can self-consistently also reproduce the observed X-ray and radio fluxes for the same black hole mass (Melia 1994), and are also indicated by the three dimensional hydrodynamical simulations (Ruffert & Melia 1994).

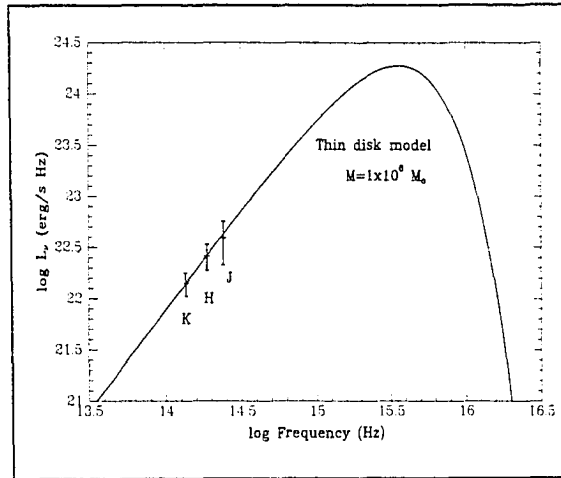


Figure 3.6: The K, H and J fluxes de-reddened (with the Galactic Center extinction law where $A_V=27.4$) and converted to luminosity density at the Galactic Center ($D=8.5$ kpc). The solid line is the computed spectrum for a small ($R=9r_g$) inclined ($i=80^\circ$) accretion disk around a $M=1 \times 10^6 M_\odot$ black hole.

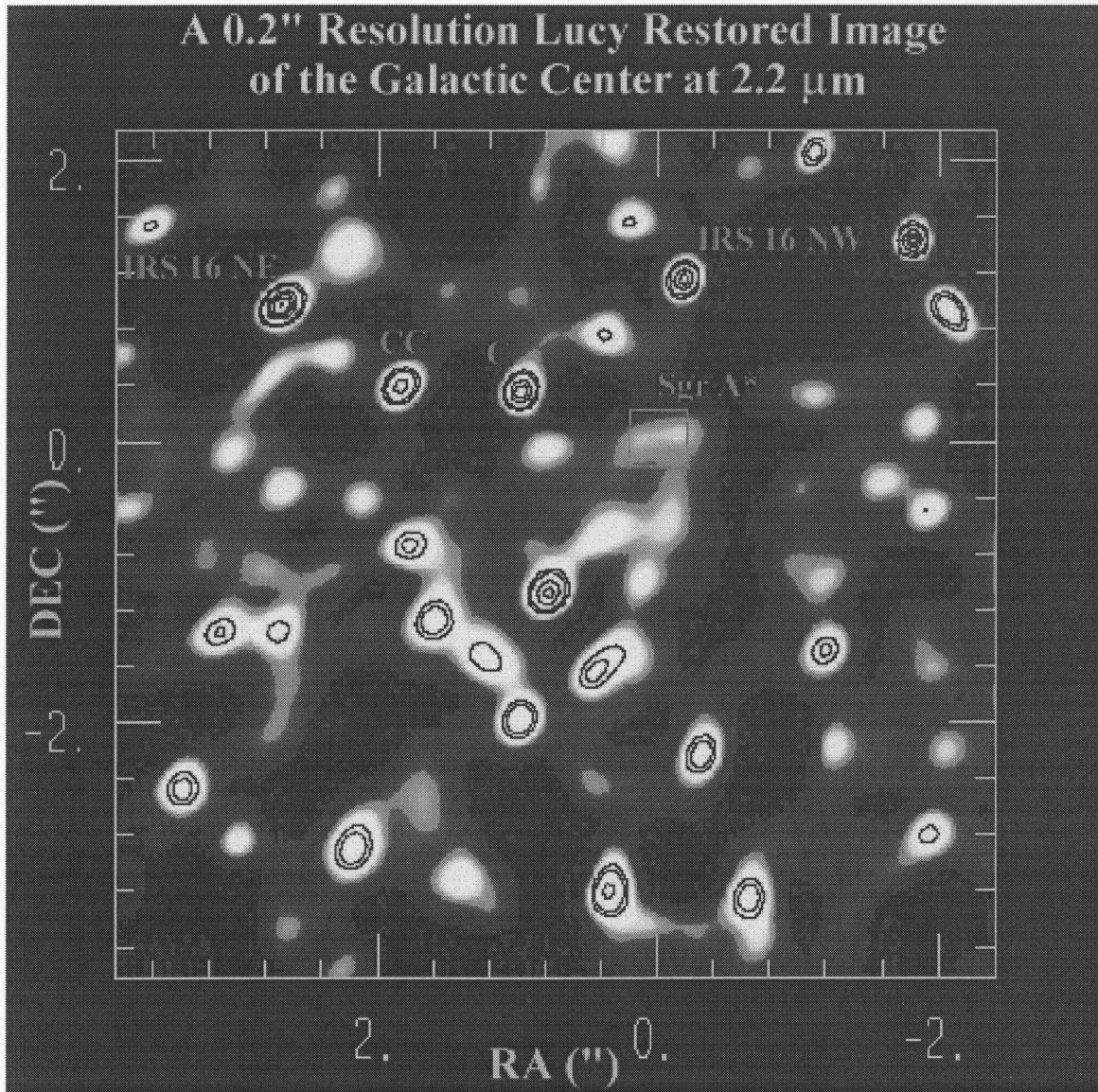


Figure 3.7: The Lucy deconvolved inner $5 \times 5''$ of the FASTTRAC image in Fig. 2.3. Note the $0.5''$ "bar" running East-West at the location of Sgr A* (marked by a small square $\pm 0.2''$ error box).

The black hole mass of $\sim 1 \times 10^6 M_{\odot}$ suggested by dynamical studies (cf., Serabyn et al. 1988; McGinn et al. 1989; Sellgren et al. 1990; Haller et al. 1996), and frequency-

dependent source size measurements (cf., Melia, Jokipii & Narayanan 1992; Backer et al. 1993) appears to be consistent with the infrared fluxes observed here. However, it should be stressed that these fluxes are also completely consistent with a hot ($1 \times 10^4 < T < 3.5 \times 10^4$ K) luminous ($L \sim 10^{3.5-4.6} L_{\odot}$) star (or tight group of stars) in the central stellar cluster. The probability of finding a hot $K \leq 12$ star (or group of ~ 5 fainter stars) within $0.2''$ of Sgr A*'s position is a small, but finite, $\sim 10\%$ in the crowded Galactic Center field. However, if the source has increased several times in brightness over the last few years (or is variable on rapid time scales) then the possibility that it is stellar is significantly reduced.

3.5.1 The Morphology of the Sgr A* Infrared Source

The most recent $0.28''$ image of the Galactic Center has been deconvolved to the diffraction-limit of the 2.3m telescope. As mentioned in §2.4.4 and illustrated in figure 2.14 this image has a high enough Strehl ratio to merit such a deconvolution. The inner $5 \times 5''$ of this Lucy restored image is illustrated in figure 3.7. It is apparent that at a resolution of $0.2''$ the Sgr A* "point source" clearly becomes a $0.5''$ "bar" running East West. This bar is $\sim 10^5$ times too large to be Sgr A*'s accretion disk; however, it does match the ~ 0.02 pc "accretion radius" (the distance at which the inter-stellar wind becomes bound) of a million solar mass black hole, and so perhaps this "bar" structure results (in part) due to a warm dust "pile-up" at the shock which should form at this accretion radius. However, it appears that most of the flux from Sgr A* is not from dust emission since figure 3.6 implies temperatures of at least ~ 6000 K.

Figure 3.7 is the first independent confirmation of this "bar" morphology observed by Eckart et al. (1993). The best image obtained at the 3.5m NNT telescope (FWHM \sim 0.13") hints that this bar is a line of 5 or more individual sources which are likely just individual hot ($T > 6000$ K) stars (Eckart 1995). It is still possible that Sgr A* is one of these point sources; however, it becomes increasingly hard to model one of these sources as a million solar mass black hole since each individual source is so faint it could only be produced by an accretion disk inclined at a very *a priori* unlikely $i \geq 88^\circ$.

3.6 Conclusions

An infrared source has been detected within $0.2 \pm 0.3''$ of the location of Sgr A*. The source's infrared fluxes are $K=12.1 \pm 0.3$, $H=13.7 \pm 0.3$, and $J=16.6 \pm 0.4$. The resulting colors are best fit by a hot object in the Galactic Center region around Sgr A* ($A_V=27.4 \pm 3.5$). No significant (3σ) periodicity is observed from Sgr A* for amplitudes $\geq 50\%$ in the period range of 3-30 min. The observed fluxes are consistent with an inclined accretion disk around a $\sim 1 \times 10^6 M_\odot$ black hole. However, they are also explained by a line of hot luminous (integrated luminosity of $\sim 10^{3.5-4.6} L_\odot$) central cluster stars positionally coincident with Sgr A* explaining the observed $0.5''$ "bar".

CHAPTER 4

IS IRAS 10214+4724 THE MOST LUMINOUS OBJECT IN THE UNIVERSE OR JUST A GRAVITATIONAL LENS?

4.1 Introduction

Since its serendipitous discovery (Rowan-Robinson et al. 1991; hereafter RR91) as a $z = 2.28$ source IRAS FSC 10214+4724 has been observed over most of the electromagnetic spectrum and has been an object of great debate. It was commonly thought that FSC 10214's unique "hyper-luminosity" and extended structure could be a product of a unique massive starburst in a protogalaxy, an obscured QSO or both (cf. RR91, Lawrence et al. 1993, hereafter L93, and Elston et al. 1994, hereafter E94). However, it is now becoming clear that FSC 10214 has an arc-like morphology suggestive of a gravitational lens (Matthews et al. 1994, hereafter M94; Graham & Liu 1995, hereafter GL95; and Broadhurst & Lehar 1995; hereafter BL95). To definitively prove that FSC 10214 is a lensed system requires a redshift for the lensing galaxy. Unfortunately this galaxy has a Gunn r magnitude of ~ 23 and is located only $\sim 1.2''$ away from the much brighter $r \sim 21$ arc; hence, obtaining a redshift has proved challenging.

This chapter presents a spectral continuum determined for this galaxy, from which a tentative redshift of 0.42 ± 0.02 is derived. The highest resolution (FWHM = $0.7''$) image of FSC 10214+4724 yet taken at H ($1.6\mu\text{m}$) with FASTTRAC is also presented. The observed

redshift and H magnitude of the galaxy indicate a lensing mass with a velocity dispersion of 210 ± 20 km/s. Such a lens should produce a faint counter-arc 1.6" north of the main arc which is indeed observed. Moreover, it is argued that it is possible that the luminosity from FSC 10214 could be explained by a background ultra-luminous infrared galaxy of $\sim 3.7 \times 10^{12} h^2 L_{\odot}$. In this chapter a $q_0 = 0.5$, $h = 0.5$ cosmology is assumed.

4.2 Observations

4.2.1 Imaging With FASTTRAC

On the photometric nights of February 18 and 21, 1995 (UT) FSC 10214 was imaged in the near infrared at H ($1.6 \mu\text{m}$) with FASTTRAC (Close & McCarthy 1994; Close, Wittman & McCarthy 1994) at the Steward Observatory 2.3m telescope at Kitt Peak. The infrared science camera was the original 256×256 NICMOS3 array (Rieke et al. 1993) with a $0.23''/\text{pixel}$ scale. For this observation a R \sim 16 star located $\sim 40''$ away (star B in RR91) was tracked at 30 Hz with the low read noise CCD. The resulting corrected images have $\text{FWHM} \sim 0.7''$, compared to the uncorrected $\text{FWHM} \sim 1.2''$.

A $54 \times 54''$ field around FSC 10214 was imaged for 60s then offset by a random amount ($< 15''$) in RA and DEC followed by the next exposure. All images were sky-subtracted and flat fielded using the median of 4 frames before and 4 after each image. The frames were aligned and averaged together based on the positions of stars A and B. The final image has a total integration time of 91 minutes and a 2σ detection limit of $22 \text{ mag arcsec}^{-2}$ (see figure 4.1a).

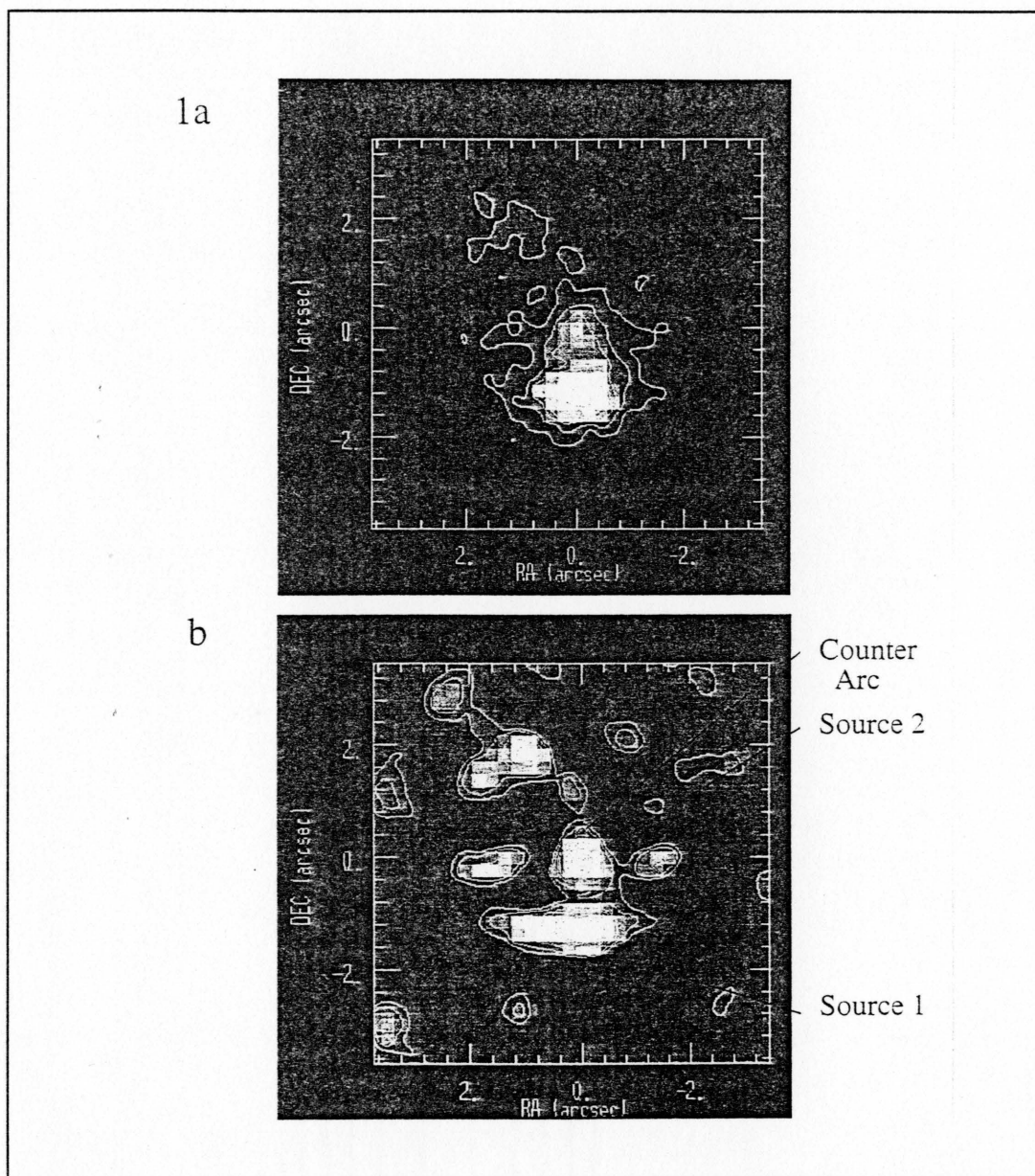


Figure 4.1a: The 91 min H image of IRAS FSC 10214 (FWHM=0.7"). Contours are at the 11($\sim 2.5\sigma$), 22, 33, 44, 55, 89% level of source 1's peak. **1b:** The result of 30 Lucy iterations on figure 4.1a (restored to FWHM=0.5"). Contours are at the 1.7 ($\sim 2\sigma$), 3, 6.7, 10, 16.7, 26.7, 40, 50, 67.7% level of source 1's peak flux. Source 1 appears to be a $\sim 2''$ long radially unresolved arc with a bright 0.5" core. Source 2 (the lens) is located 1.25" north and is unresolved in its core. There appears to be a blended source $\sim 0.35''$ north of source 2, which is tentatively identified as the counter-arc image. The weak emission just north of the counter-arc is likely detector noise since it is detected only in frames from one night.

This image was then deconvolved with 30 iterations of the Lucy algorithm and restored to a resolution of 0.5" (see figure 4.1b) using star A as an excellent high S/N PSF. In addition, the image was deconvolved with a linear flux-conserving multi-frame iterative deconvolution algorithm (IDA, see Jefferies & Christou 1993), again using star A as the PSF, to produce a 0.4" FWHM image. The morphologies of both the Lucy and IDA deconvolved images are nearly identical and so only the Lucy image is displayed in figure 4.1. As depicted by figure 4.1b, FSC 10214 appears to be composed of 2 main components: a southern extended ($\sim 2''$ long) arc-like object, which will be referred to as source 1 (after M94), and a fainter object 1.25" north of source 1 referred to as source 2. This morphology is very similar to that of the K ($2.2\mu\text{m}$) images obtained by M94 and GL95.

The raw and IDA deconvolved images were examined with DAOPHOT (Stetson 1987). Photometry was calibrated with the Elias standard HD18881 (Elias et al. 1982). Within a 2" beam; star A has $H=16.05\pm0.15$, source 1 has $H=17.4\pm0.2$, and source 2 has $H=18.5\pm0.2$. The errors are dominated by the uncertainty in the absolute calibration. These magnitudes are similar to those measured by E94.

4.2.2 Spectroscopy

Since the definitive test of the lensing hypothesis can only be made by securing a redshift for source 2, FSC 10214+4724 was observed in $\sim 0.6''$ seeing with the Blue Channel spectrograph on the MMT on the night of April 6, 1995 (UT). Four separate 30-minute exposures, all at airmass < 1.1 were obtained. The slit during each exposure was aligned

N-S, allowing a spectrum for a galaxy 23" to the south of the object to also be obtained. The spectra have scales of 0.30"/pixel spatially and 3.90Å/pixel in the dispersion direction which slightly undersamples the resolution of 6.2Å for the 1" slit used. The spectra were reduced using the usual bias subtraction and flat fielding procedures. The night sky spectrum was determined for each image individually, replicated to two dimensions and subtracted. The subtraction was excellent in intensity and wavelength, with the tilt of the sky lines from

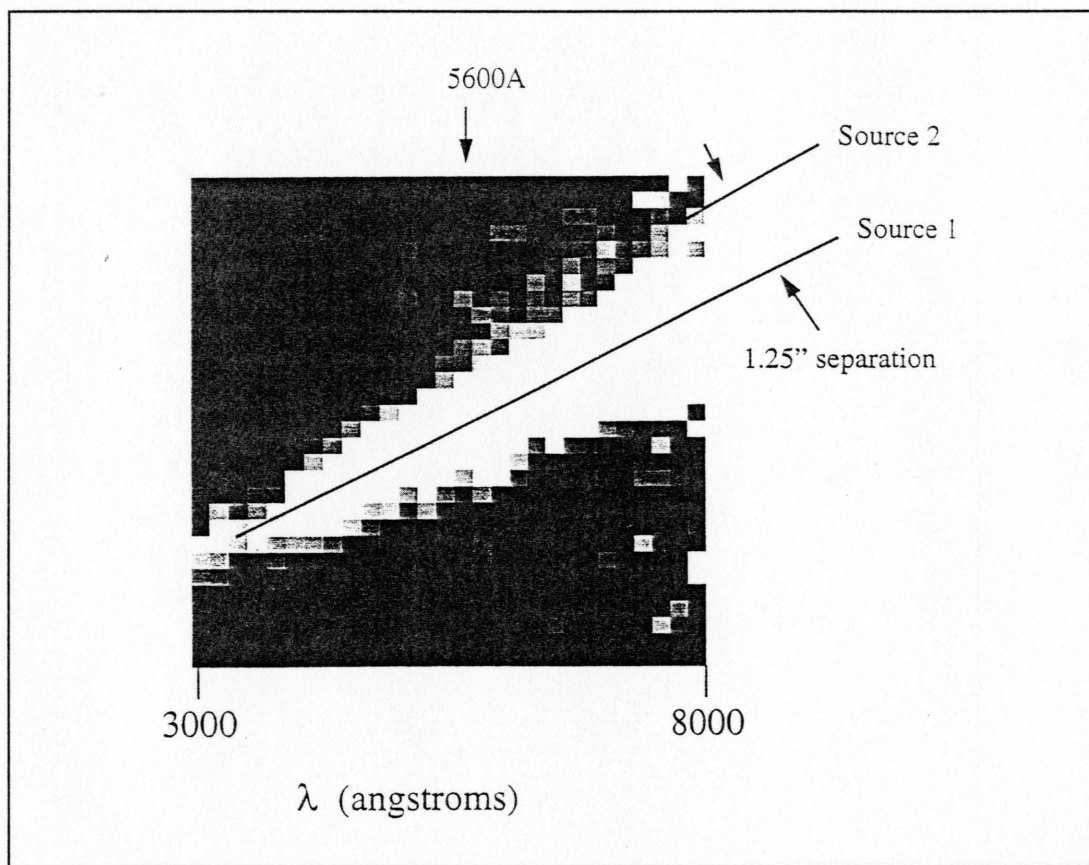


Figure 4.2: Binned 150Å/pixel "spectrum" of source 2. The tilt of the F_0 spectrum is from the instrument optics, not atmospheric dispersion. Note the presence of a weak component 1.25" north of source 1 redward of 5600Å, which is identified as continuum from source 2.

bottom to top <1 pixel. The four background-subtracted two-dimensional spectra were coadded using median combining and a sigma-clipping algorithm for cosmic ray rejection, and with small integer-pixel offsets in the spatial direction as determined from the four strongest lines in the spectrum. No offsetting was done in the dispersion direction since the measured offsets were all <1 pixel in that direction. Despite the excellent seeing, the FWHM of the coadded spectrum in the spatial direction is $\sim 1.2''$, probably due to drift in the MMT mirror stacking. Finally, the coadded two-dimensional spectrum was flux calibrated by an observation of Feige 34, extinction was corrected with a standard extinction curve, and wavelength calibration was performed using a weighted average of two comparison lamp exposures.

Since there was no separate trace of source 2 clearly visible in this coadded two-dimensional spectrum, it was decided to increase the S/N by binning the spectrum in wavelength space. The spectrum was divided into segments ~ 40 pixels ($\sim 150\text{\AA}$) in length, avoiding strong night sky line residuals and emission lines from source 1. Each segment was collapsed down to a single pixel in the dispersion direction using a simple average and reassembled into a new, much shorter spectrum shown in figure 4.2. North of the bright continuum of source 1 there is a detection of source 2 redward of 5690\AA . There is no known optical ghost in the MMT+Blue Channel optics that would cause this effect. As a check, the

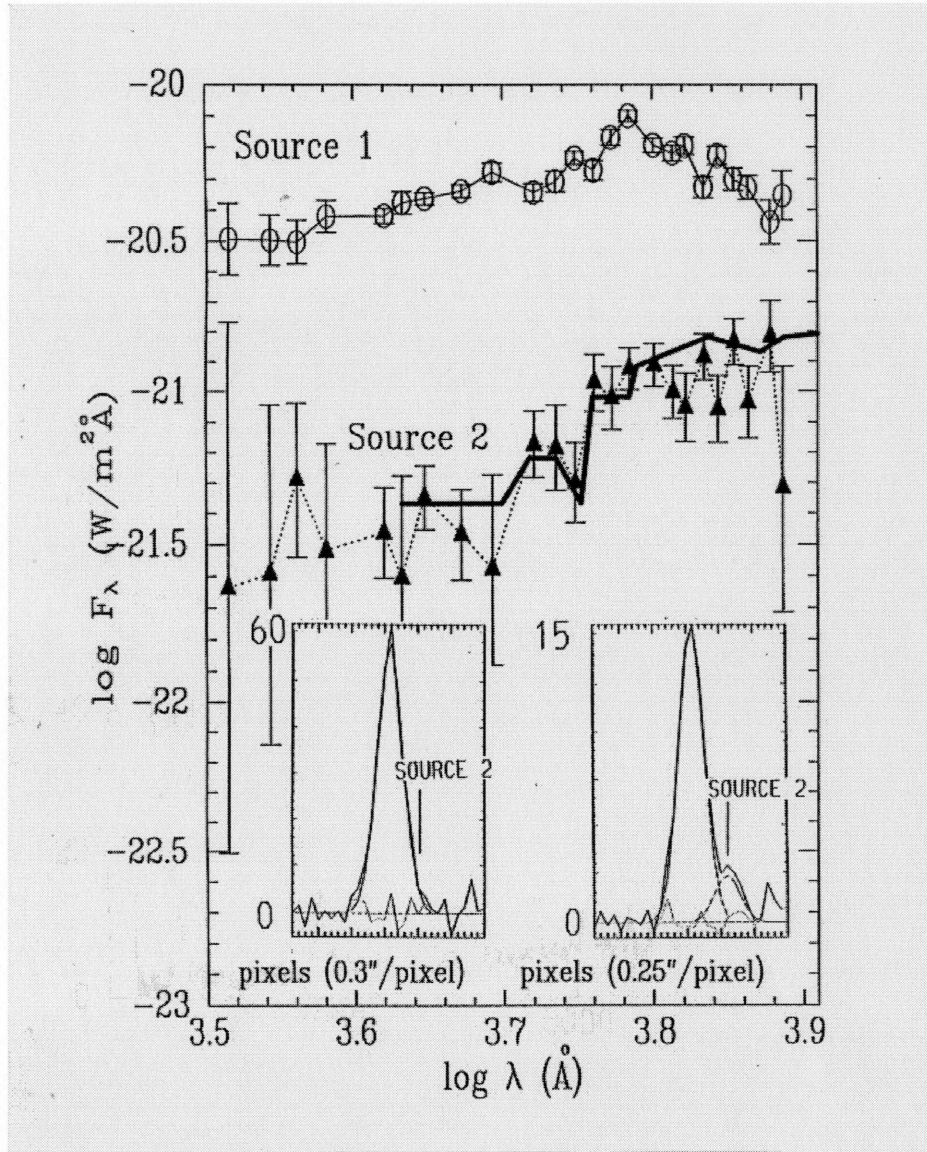


Figure 4.3: The binned continuum of source 1 is marked by open circles (see section 4.2.2 for details). The binned continuum for source 2 is marked by the solid triangles. The 13 Gyr old 1 Gyr burst E0 SED model of Bruzual & Charlot 1993 has been redshifted to $z=0.42$ and over plotted for comparison (dark solid line). Note the good match to the 4000\AA break at 5690\AA . **Right Hand Inset:** a typical spatial cut of the binned continuum (at 6300\AA) across source 1 (center) and source 2 ($1.2''$ right of center). The dashed line is the blended gaussian fit of source 1 and source 2 to the continuum. **Left Hand Inset:** a spatial cut across the CIII emission line ($\sim 6200 \text{\AA}$). Note the lack of emission above the continuum level at the position of source 2. This shows that the continuum from source 2 is not scattered light from source 1.

the spectrum of the galaxy 23" south of FSC 10214 was binned, as was standard star in the same manner. Neither showed any excess flux to the north at the red end of the spectrum. Thus the emission appears real, albeit of low S/N.

Even with this extreme binning, source 2 is faint enough and near enough to source 1 that normal extraction of its spectrum is difficult. Instead, two blended gaussians (see the right-hand inset in figure 4.3) were fit to each column of the binned two-dimensional spectrum shown in figure 4.2. The widths of the gaussians were constrained to be identical, the continuum was set to zero, and the separation between the gaussians was fixed at the 1.25" separation between source 1 and 2, although the absolute peak positions were allowed to vary from the initial estimate. The F_λ flux of each gaussian is plotted vs. wavelength in figure 4.3 for sources 1 (open circles) and 2 (solid triangles). Excluding the area around the bright emission lines from source 1 (see figure 4.4a), it was found that the continuum fit was almost always better with a second gaussian (source 2) $\sim 1.25''$ north of the main gaussian (cf. the right-hand insert in figure 4.3). As a test, two blended gaussians were fit with the second gaussian forced $1.25''$ *south* of the peak of source 1. The flux in this gaussian was reassuringly consistent with zero across the spectrum.

It is seen from figure 4.3, that the continuum spectrum of source 2 is not identical to that of source 1. It is also possible to check whether or not source 2 has emission lines at the same wavelengths as source 1. If the equivalent widths are equal in each component, one expects to see emission lines from source 2 at $\sim 13\%$ the strength of those in source 1; no such emission is seen at any of the emission lines. For example the CIII line is shown to have

no emission above the continuum at the position of source 2 in the left-hand insert in figure 4.3. This agrees with narrowband imaging studies (ef. Soifer et al 1992) which suggest no line emission from source 2.

The only significant feature in the spectrum of source 2 is the break at an observed wavelength of $5690 \pm 90 \text{ \AA}$. It is extremely unlikely that source 2 is at $z=2.286$ since there is

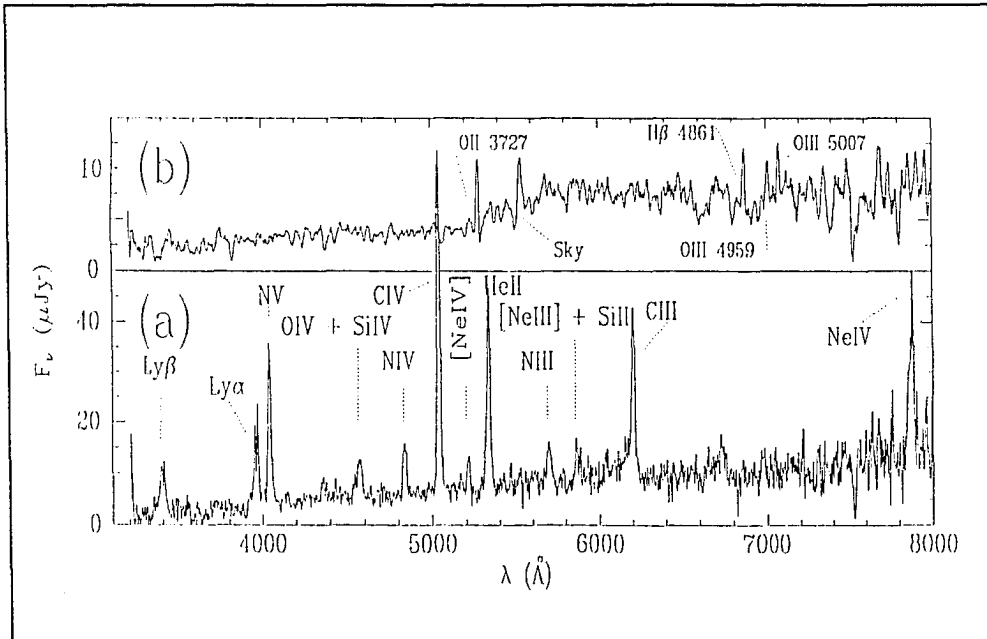


Figure 4.4a: A F_v spectrum of source 1. The measured equivalent widths are consistent with previously published measurements. The spectrum extends farther to the blue than any other published spectrum, showing that $\text{Ly}\beta$ is self-absorbed like $\text{Ly}\alpha$ and that it has an anomalously large equivalent width, 1.4 ± 0.5 times that of $\text{Ly}\alpha$. $\text{Ly}\beta$ also appears to be redshifted $\sim 5000 \text{ km/s}$ with respect to $\text{Ly}\alpha$, but the wavelength calibration is suspect this close to the atmospheric cutoff, thus it is possible that this line is instead $\text{OVI } 1031/1037$. There is also a noticeable depression of the continuum blueward of $\text{Ly}\alpha$ due to the $\text{Ly}\alpha$ forest, quantifiable as a flux deficit $D_A = 0.28 \pm 0.36$, a reasonable value for $z=2.3$ (Schneider et al. 1989). **4.4b:** Optimally extracted spectrum of the galaxy $23''$ south of FSC 10214+4724. $\text{OII } 3727$ and $\text{H}\beta$ are clearly visible, along with $\text{OIII } 4959/5007$ at lower significance, giving a redshift of $z=0.429 \pm 0.002$. The spectrum has been smoothed with a 20 \AA boxcar.

no known feature that would cause such a break at 1730\AA rest wavelength. Therefore this feature is tentatively identified with a 4000\AA break, implying that source 2 has a redshift of $z_L=0.42\pm0.02$ and is thus gravitationally lensing source 1. The break is only significant at the 2.2σ level; however, its strength of 1.9 ± 0.8 is consistent with the range 1.8-2.4 expected for an early type galaxy at $z\sim0.42$. This is shown in figure 4.3 by the overlay of Bruzual & Charlot's (1993) E0 SED redshifted to 0.42 (dark solid line). *A priori*, one may expect a lensing galaxy to be an early type, since such galaxies are more efficient lenses due to their deeper central potentials (Turner et al. 1984).

Further evidence in support of $z_L=0.42$ comes from the emission line galaxy 23" to the south, whose spectrum, reduced in the standard way, shows an emission line redshift of $z=0.429\pm0.002$ (figure 4.4b). Moreover, there are six extended objects within 23" of source 2, which is a 3σ overdensity at this galactic latitude (M94). Thus it is quite possible that both source 2 and this galaxy are part of a group at $z\sim0.43$. While it is dangerous to claim association based on position alone, the known presence of one galaxy at $z=0.43$, plus the overdensity in this field, makes the tentative $z_L=0.42$ redshift more likely.

4.3 Discussion

Assuming that source 2 is an early type galaxy at $z_L=0.42$ with an observed H magnitude of 18.45 ± 0.15 in a 2" aperture implies a D0 ($\sim50\text{kpc}$) aperture corrected magnitude of 17.28 ± 0.28 (from the H growth curves of Aaronson, Huchra, & Mould 1979). Thus, source 2 has $M_H=-25.1\pm0.3$ for $q_0=0.5$, $h=0.5$ (incorporating the relatively small -

0.3 ± 0.1 mag of evolution and K corrections estimated from the early-type galaxy SED of Bruzual & Charlot 1993). An elliptical galaxy of this magnitude has a rest frame color of $\langle H-K \rangle = 0.20 \pm 0.05$ (Mobasher, Ellis, & Sharples 1986), from which a $M_K = -25.3 \pm 0.3$ for source 2 is estimated. Since the K-band luminosity function has $M_K^* = -25.5 \pm 0.3$ (Mobasher, Ellis, & Sharples 1993), it appears that source 2 is consistent with a L^* galaxy. This reasonable luminosity further indicates the plausibility of the 0.42 lens redshift.

Utilizing the Faber-Jackson relation (Faber & Jackson 1976) one finds a velocity dispersion of $\sigma \sim 210 \pm 20$ km/sec is typical for this luminosity. One can use this velocity dispersion to predict the morphology of the image formed by the lens. If it is assumed that the lensing galaxy can be approximated by a singular isothermal spherical mass distribution, then the separation δ between the main arc (source 1) and the counter-arc along the (north-south) axis of symmetry is roughly given by:

$$\delta \sim \frac{8\pi\sigma^2 D_{sL}}{c^2 D_s} = \frac{8\pi\sigma^2}{c^2 \sqrt{1+z_L}} \left[\frac{\sqrt{1+z_s} - \sqrt{1+z_L}}{\sqrt{1+z_s} - 1} \right] \quad (4.1)$$

($\Omega_0 = 1$), where D_s is the angular diameter distance to the source and D_{sL} is the angular diameter distance from the lens to the source (Blandford & Narayan 1992). Based on the determination of $z_L = 0.42$, $\sigma \sim 210 \pm 20$ km/s, and $z_s = 2.28$, equation 4.1 predicts $\delta = 1.6 \pm 0.2''$. After subtracting source 2 from figure 4.1b, it is apparent that indeed there is a faint ($H \sim 21.8$) source $1.6 \pm 0.1''$ north of source 1. This 2σ detection is only tentative; however,

a re-analysis of M94's deeper K band image by BL95 produces a source at this position, as does a sharper K image taken by GL95. Hence, the case for the presence of a counter-arc located $\sim 1.6''$ north of source 1 is very compelling. This shows the parameters $z_L=0.42$, $\sigma \sim 210 \text{ km/s}$ and $z_s=2.28$ are consistent with the morphology and photometry independently observed in three recent images of the lensed object.

Since FSC 10214 appears to be lensed, its unique "hyper-luminosity" could be merely due to magnification of a more common, fainter extragalactic object. The strong ($\sim 17\%$) polarization of optical emission and reddened narrow line emission spectra of the background source are similar to the properties of a Seyfert II (L93, E94, and Jannuzi et al. 1994). Hence, it is worthwhile to see if a typical Seyfert II could be lensed by source 2 and produce the observed (lensed) luminosity of $\sim 1.2 \times 10^{14} h^2 L_\odot$ (Rowan-Robinson et al. 1993).

A possible geometry for this system suggested by BL95 places the Seyfert II core just south of the southern cusp in the typical "diamond" inner caustic formed by elliptical lenses. This results in a tangential stretching of the obscured AGN core and central dust torus into two thin arcs on either side of the lensing galaxy separated by δ arcsec. BL95's full simulation of the gravitational lens justifies a simple assumption that the magnification of the source can be approximated by l/d , where l is the length of the arc and d is the intrinsic diameter of the source. This approximation is applicable for small d , up to a maximum $m=50$ for their model.

Downes et al. (1992) fit the IR emission from FSC 10214 with two dust components: $\sim 3.8 \times 10^{13} L_\odot$ from $T=80 \text{ K}$ dust and $\sim 4 \times 10^{13} L_\odot$ from warmer $T=230 \text{ K}$ dust. The remaining

$\sim 4 \times 10^{13} L_{\odot}$ of optical through x-ray luminosity may plausibly be attributed directly to the AGN (which may also be the source heating the dust). This obscured AGN will be seen reflected from a "mirror" region (Antonucci 1993) and could be lensed into the observed bright 0.5" long core which is the center of source 1 (figure 4.1b). This is in good agreement with observations in the optical and radio which are mainly sensitive to emission from the AGN core of the background source (BL95, L93). Since "mirror" regions are estimated to have $d \sim 100$ pc (Antonucci 1993), or 0.0125" at $z=2.286$ ($h=0.5$, $q_0=0.5$), then $m \sim 0.5/0.0125=40$. This yields an intrinsic luminosity for the AGN component of $L_{\text{AGN}} \sim 1 \times 10^{12} h^{-2} L_{\odot}$. This is less than that of the narrow-line object IRAS 20181-2244 (Elizalde & Steiner 1994). Therefore, it is a plausible intrinsic L_{AGN} luminosity.

To see if FSC 10214's IR luminosity could result from thermal emission from the obscuring dusty torus, following BL95 and estimating the minimum size an optically thick thermal spherical surface could have and still produce a given L_{IR} yields:

$$d \geq \sqrt{\frac{L_{\text{IR}}}{\pi \sigma T^4}} \quad (4.2)$$

For the $T=230$ K dust component, if it is assumed that the magnification is at its maximum of ~ 50 then an intrinsic $L_{\text{IR}} = 8 \times 10^{11} L_{\odot}$ is required, which can be generated in an area with a diameter as small as ~ 30 pc, well below the maximum size of 80 pc possible for $m=50$. For

the cooler $T=80$ K dust if one assumes a reasonable $d \sim 400$ pc, then in the simple approximation of $m \sim l/d$, one can still have $m=40$ if it is assumed that this region is responsible for the full $\sim 2''$ long arc. However, using the more exact dependence of magnification m on source size d of BL95 (their figure 2), it is found that for $d \sim 400$ pc, $m \sim 20$. Thus, the intrinsic luminosity of the $T=80$ K dust component must be $\sim 1.9 \times 10^{12} L_{\odot}$ in this model to produce the $\sim 2.0''$ arc and account for $\sim 3.8 \times 10^{13} L_{\odot}$.

Summing these three emission components in this simple lensing model, it is found that the intrinsic (unlensed) luminosity of FSC 10214 is $\sim 3.7 \times 10^{12} h^2 L_{\odot}$. Consequently, even though it is lensed by magnifications $m \sim 20-50$, FSC 10214 is not a typical Seyfert II but an ultraluminous infrared galaxy (ULIRG; Sanders et al. 1988) with a Seyfert II-like spectrum typical of the most luminous infrared galaxies (Veilleux et al. 1995). In fact, it would be the third-most luminous object discovered by IRAS, behind only IRAS 15307+3252 (Cutri et al. 1994) and IRAS 09104+4109 (Hines & Wills 1993). While such high luminosity objects are very rare at low redshifts, they may have been more common at high z if the ULIRG population has undergone positive luminosity evolution. And while such a large magnification is *a priori* unlikely (Trentham 1995), it is consistent with the lensing geometry, and lower magnifications require FSC 10214 to be even more intrinsically luminous (GL95). While it is somewhat unsettling that one of the intrinsically most luminous objects in the known universe is also gravitationally lensed, FSC 10214 may have been discovered only *because* it is so strongly magnified. Unlensed and lensed but less strongly magnified high-redshift ULIRGs will have escaped discovery because they are too faint to

make it into IRAS-selected surveys. Thus, it is possible that this simple treatment of the lensing geometry and emission components of FSC 10214 yields a plausible answer for its intrinsic properties. However, a more detailed treatment, constrained by a confirmation of the lens redshift and by HST images (Eisenhardt et al. 1995), is required to confidently derive the intrinsic properties of this unique object.

4.4 Conclusions

A high spatial resolution H image and spectroscopy of IRAS FSC 10214+4724 have been obtained. This image depicts FSC 10214 as a radially unresolved $\sim 2''$ long arc with a $0.5''$ core (source 1) focused on a fainter object with a unresolved core (source 2) $1.25''$ north. A tentative spectral continuum for source 2 is identified. This continuum has a 2.2σ break at $5690 \pm 90 \text{ \AA}$. The position and strength of the break is suggestive of a early type galaxy's 4000 \AA break at a redshift of 0.42 ± 0.02 . In addition, the redshift of a galaxy only $23''$ south of source 2 was found to be a very similar $z = 0.429 \pm 0.002$.

The observed $H = 18.45 \pm 0.15$ magnitude of source 2, combined with a redshift of 0.43 , implies that it has $M_K = -25.3 \pm 0.3$, consistent with a typical L^* early-type galaxy. This magnitude indicates a velocity dispersion of $\sigma \sim 210 \pm 20 \text{ km/s}$. Such a galaxy will produce the observed arc-like morphology of source 1 by gravitational lensing and form a counter-arc $1.6 \pm 0.2''$ north of source 2. Since such an counter-arc is observed in this work and others (BL95, GL95) one finds the paradigm that IRAS FSC 10214+4724 is a gravitational lens image produced by a galaxy at $z = 0.43$ very compelling. Finally, it was argued that the

background source is an ultraluminous IR galaxy with an intrinsic (unlensed) luminosity of $\sim 3.7 \times 10^{12} h^{-2} L_{\odot}$.

CHAPTER 5

AN ADAPTIVE BEAM COMBINING MIRROR FOR THE MMT

This chapter discusses the present effort in developing a new tip-tilt adaptive system at Steward Observatory. The new system (called FASTTRAC II) is the natural successor to FASTTRAC in that it tip-tilt corrects all six MMT beams.

It is important to note that development of FASTTRAC II was an effort carried out by the whole AO team at Steward Observatory. The author's main contribution to the project was in the development of a novel six element tip-tilt beam combiner with Guido Brusa and Don Bruns. Therefore only the development of the FASTTRAC II's beam combiner will be highlighted here.

5.1 Introduction

The Center of Astronomical Adaptive Optics (CAAO) at Steward Observatory has a mission to provide the 6.5m MMT upgrade with a laser guide star, diffraction-limited AO system optimized for the near-infrared. This upgrade will replace the six 1.8m primaries with a single 6.5m mirror in 1997. In the meantime, CAAO has undertaken the development of FASTTRAC II which is a less complex instrument utilizing the existing six mirror MMT. It will serve as a mechanical, electrical, and software testbed for the 6.5m system, and will also be a powerful scientific instrument in its own right.

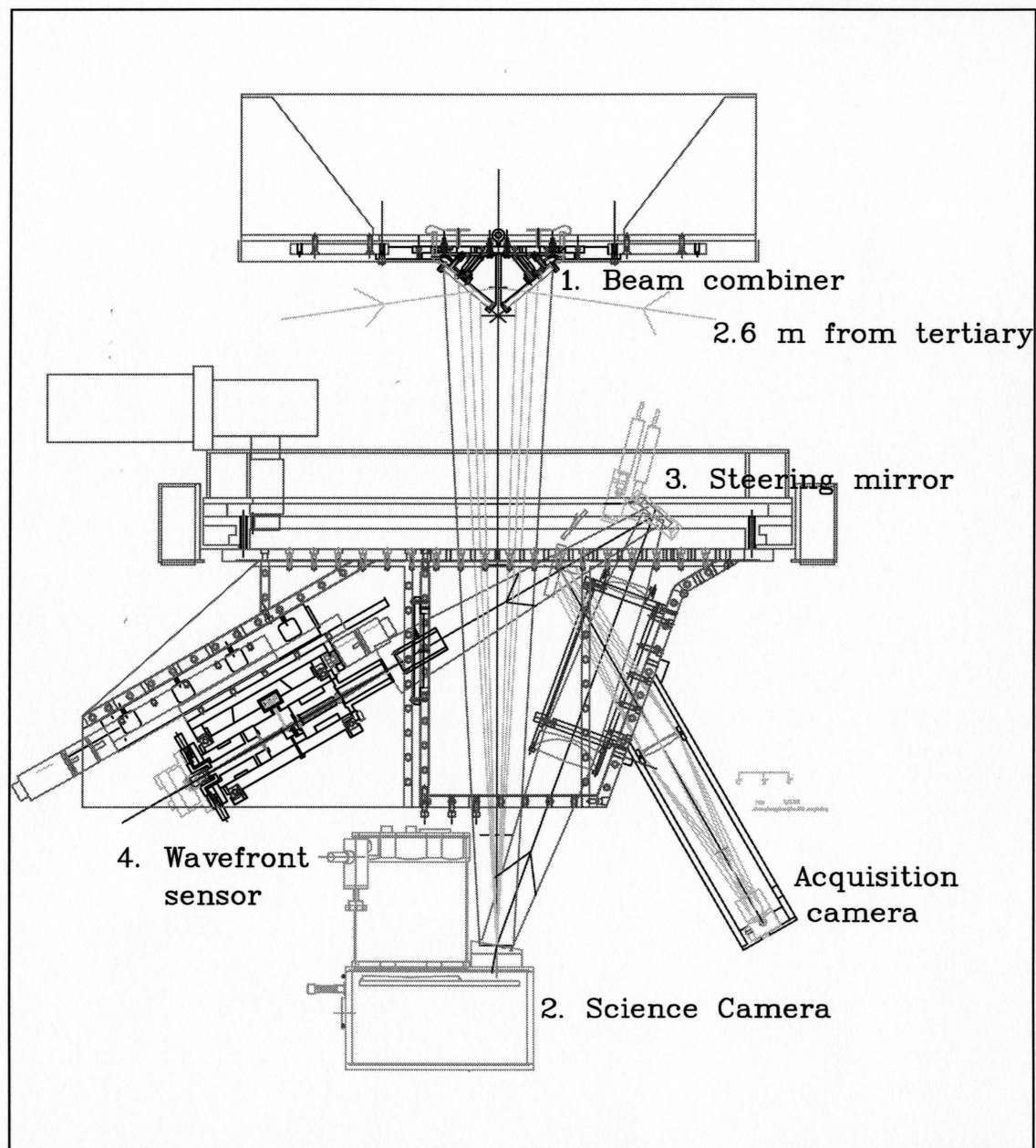


Figure 5.1: A cross-section of the whole FASTTRAC II instrument. The beam combiner adaptively folds light from all six primaries onto a dichroic entrance window of the infrared NICMOS3 Adaptive Optics Science Camera. Visible light from a guide star (found by the 4' FOV acquisition camera) is reflected off the dichroic and steered to the wavefront sensor (WFS). Based on the relative and global tilts measured by the WFS the beam combiner adaptively stacks all six beams at the focal plane of the science camera.

FASTTRAC II adaptively combines all six of the MMT's incoming $f/31.6$ beams into a common $f/8.4$ envelope (Gray et al. 1995). This instrument utilizes six independent tip-tilt correctors; hence it is the successor to FASTTRAC which utilizes a single tip-tilt Cassegrain secondary mirror (Close & McCarthy 1993; Close & McCarthy 1994).

For FASTTRAC II to adaptively stack the MMT beams, a six sided pyramidal beam combiner was developed. Each side of the pyramid is a tip-tilt mirror (see figure 5.1). For mechanical simplicity these mirrors do not move in piston, and so FASTTRAC II cannot at this time co-phase the MMT mirrors. Since this adaptive beam combiner replaces the existing static beam combiner normally used, no extra warm optical surfaces are added by FASTTRAC II from the point of view of the cryogenic infrared science camera (figure 5.1), resulting in the minimizing of the thermal background.

FASTTRAC II should achieve $0.3''$ FWHM images with Strehl ratios of ~ 0.5 , since it is well known (Close & McCarthy 1994) that rapid tip-tilt correction over a 1.8m aperture at K ($2.2\text{ }\mu\text{m}$, where r_0 can be $\sim 100\text{cm}$ at Mt. Hopkins (Lloyd-Hart et al. 1993) can achieve diffraction-limited resolutions. To meet these goals requires that each beam be stabilized to $\leq 0.05''$ rms (Goesbeck et al. 1995). Such a constraint requires the individual mirrors to have risetimes of $\sim 3\text{ms}$ or less to compensate for the turbulence typically observed at Mt. Hopkins. Moreover, all erroneous motion due to cross-talk and mechanical resonance must be minimized in the beam combiner when all six mirrors are simultaneously active.

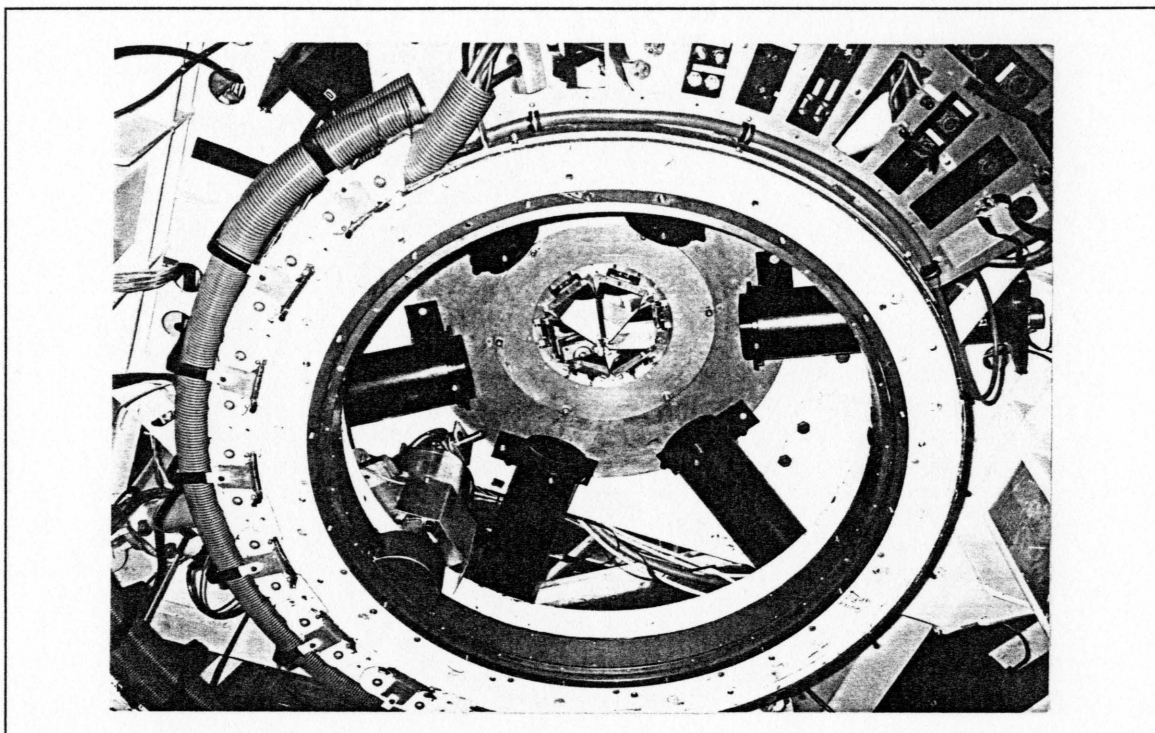


Figure 5.2: The beam combiner mounted at the MMT.

5.2 Design of the Beam Combiner

As depicted in figures 5.1 and 5.2 the beam combiner is a six sided pyramidal structure with each face a reflecting tip-tilt mirror. The major components of the actuators in each of these mirrors will be described first.

5.2.1 Capacitive Displacement Sensors

The heart of the servo system is a high speed (~ 10 KHz) displacement sensor to allow the accurate control of the mirror. Low cost capacitive sensors developed by the Arcetri Observatory in Italy and tested by Guido Brusa were used. The capacitance of a parallel plate capacitor is proportional to A/D , where A is the area of the conductive plates and D is the

separation between the plates. Therefore, a change in the displacement of a tip-tilt mirror could be determined by measuring a change in capacitance between a dynamic plate attached to a mirror and a static one attached to a reference surface. This concept results in capacitive displacement sensors that are economical (<\$100) and very accurate ($\sim 1\text{nm}$ rms up to 10 KHz).

To control each axis of the mirrors, two of these capacitors were placed on orthogonal axes (figure 5.3a) between the mirror and the static reference "wedge" holding the mirror (figure 5.3b). The capacitors were positioned as far along the axis as possible to maximize their lever-arm. A circular shape was chosen for the plates to maximize their areas. This created $\sim 12\text{pF}$ capacitances with $100\text{ }\mu\text{m}$ gaps between the plates. This has proved to be a large enough gap to avoid shorting due to slight non-parallelism between the plates.

5.2.2 Voice Coil Drivers

Voice coils drivers positioned the mirrors. The design used a moving magnet yoke acted on by a small voice coil. Since the mirrors were relatively massive, gluing the magnets directly to them did not appreciably alter their effective moment of inertia or the force required to move them. The advantage of this design is that the voice coils could be well grounded thermally to the wedge support structure. This avoided the heat dissipation problems of attaching the voice coil to the mirror. In addition, the only wire connections to the mirror were for the two capacitor plates.

Each actuator used a $3/8$ inch diameter, $1/4$ inch long NdFeB magnet inside a cold

rolled steel yoke. The voice coil used 25 feet of #40 gauge copper wire, resulting in a resistance of 26 ohms and an inductance of 140 μ H. The voice coils were designed and built by Don Burns of ThermoTrex Inc. The transfer function measured 0.3 N/ \sqrt{W} , and typically varied less than $\pm 0.5\%$ over a 1 mm range. The inductance prevents operation at very high drive frequencies, but this was not a problem for FASTTRAC II.

5.2.3 PID Control Circuit

A typical PID (Proportional-Integral-Derivative controller) analogue circuit was used to lock the mirrors to a commanded tilt. The PID utilized the positional feedback from the capacitive displacement sensor to drive the voice coils. The PID was tuned to provide a 3ms 10-90% critically damped risetime response. This performance was so impressive that a slightly modified design of these actuators is being used for the 300 element adaptive secondary for the 6.5m system, where cost per actuator is an important factor (Bruns et al. 1995).

5.2.4 Mirror Pivots

A challenging aspect of this design was the constraint placed on the tip-tilt pivots because the voice coils could not provide large forces. Therefore, the design required that the two axis tip-tilt pivot point be at the center of gravity of the mirror to minimize gravitational loading for a range of telescope elevations. Moreover, the pivot was required to have a low stiffness to help reduce the power required by the voice coils to rapidly tilt the mirror. Hence

a "floppy" tip-tilt pivot was needed, but the pivot had to be at the same time very stiff in piston and twist.

A solution, suggested by W. Davidson (Steward Observatory Technical Staff), was developed by silver soldering the long edges of two 0.5x0.2 inch rectangular pieces of stainless steel shim stock (0.010 inch gage) to the mirror and the wedge. A tilt of the mirror bends the stock in the direction of least resistance (perpendicular to the normal of the shim stock), while piston or twisting motion was forbidden. Each axis of the pivots consisted of two pieces of shim stock angled at 45° so that a virtual pivot was formed at the center of gravity of each mirror. The pivots had low resonances along each of the tip-tilt axes ($\sim 20\text{Hz}$). However, in piston and twist, the resonances were considerably stiffer at $\sim 800\text{Hz}$. Hence, the PID circuit could compensate for the low 20Hz resonance while the higher fundamentals for piston and twist were not excited by normal closed-loop operation. Moreover, the low pivot stiffness in tip and tilt allowed the voice coils to drive the mirrors at 150Hz with a $\pm 0.5''$ throw (on the sky) ($\sim \pm 2.5 \mu\text{m}$ at the capacitors) while only requiring ~ 0.1 Watts. Such low power is an insignificant thermal contribution to the background.

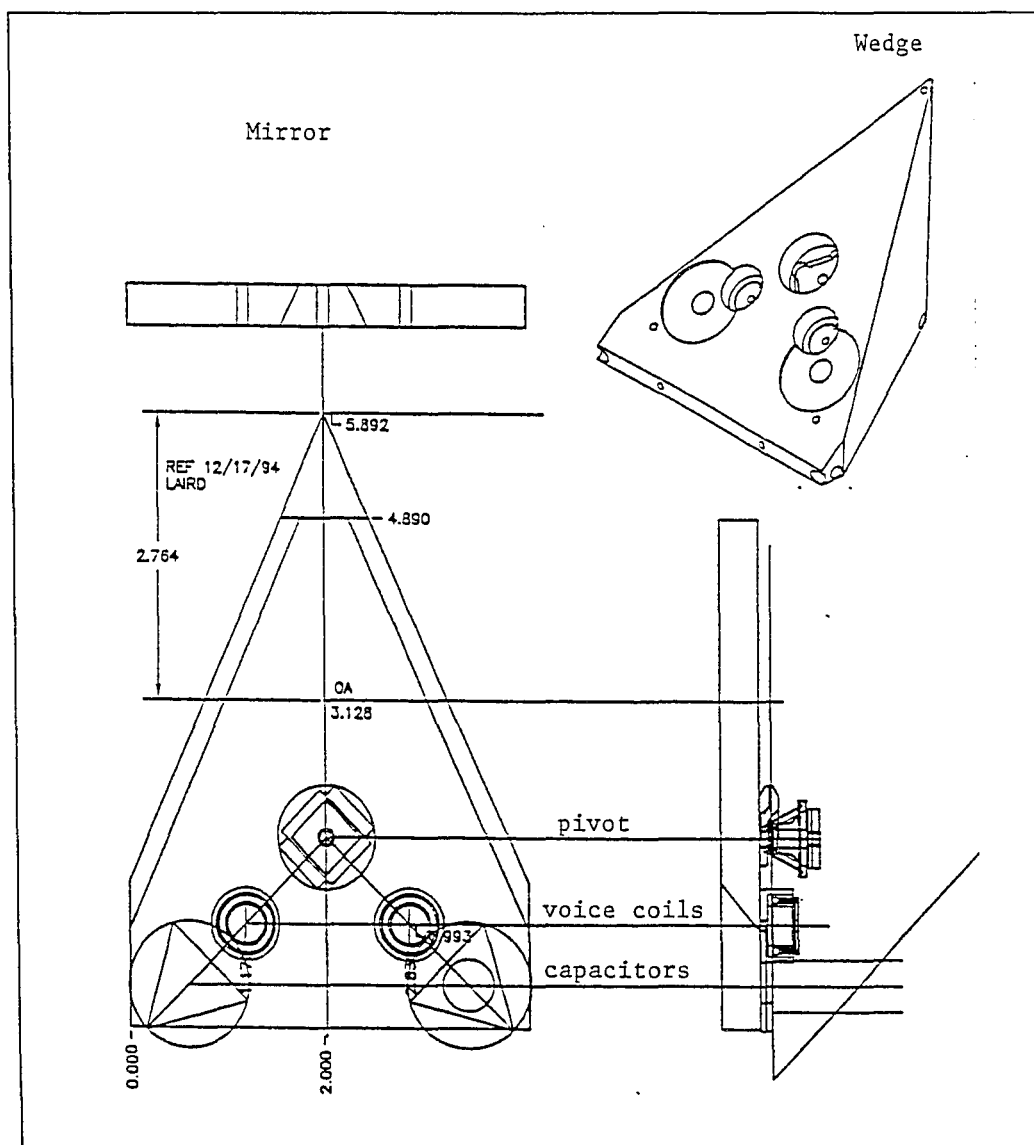


Figure 5.3a: The back of a single tip-tilt mirror (all dimensions in inches). The two axis pivot is located at the center of gravity. The two orthogonal control axes are shown. On each axis the voice coils follow the capacitor plates (at the corners). **b:** The right hand side shows the wedge which holds the mirror. The wedge is shown in cross-section with the mirror attached by the pivot. Also a 3D inset of a wedge without a mirror is shown for clarity (*above right*).

5.2.5 The tip-tilt mirrors

The mirror shapes were designed to maximize the lever arm for the voice coil drivers and capacitive sensors while simultaneously minimizing the rotational inertia. In addition, the mirrors were required to fit into a pyramidal reflector that could produce a $f/8.4$ common envelope and minimize the vignetting of an off axis source ($\sim 10\%$ for $60''$ off axis). The final design shown in figure 5.3a highlights how the pivot was located at the center of gravity of the 230g Zerodur mirrors. From this pivot point the two orthogonal tilt axis are defined with a voice coil driver and a capacitive displacement sensor on each axis.

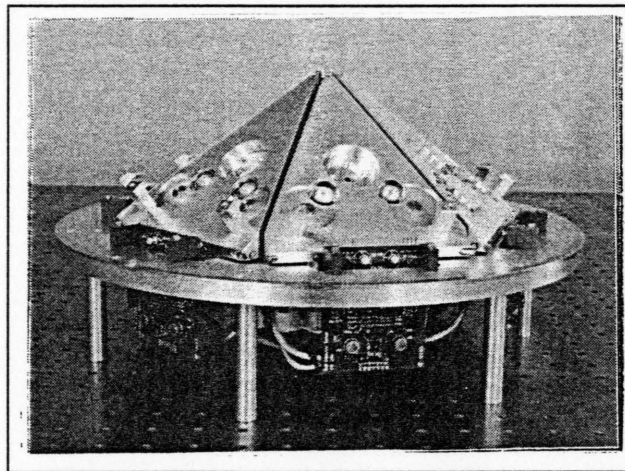


Figure 5.4: The whole beam combiner with all six wedges assembled but without the mirrors.

The thickness of the pivots suspended the mirrors 0.1 inches above the wedges (figure 5.3b). The bottom plate of each capacitor was raised so that the gap between the plates was $\sim 100\text{ }\mu\text{m}$. The magnet section of the voice coil (which was glued to the mirror) sunk into the voice coil yoke attached to the wedge. In this manner, all six mirrors were attached to their corresponding wedges.

5.2.6 System Integration

The final system was designed and built by Don Bruns and Peter Gray (Steward Technical Support Group). The beam combiner system consisted of three main parts. The adaptive beam combiner itself was mounted in the constricted central part of the MMT (see figure 5.2). The PID controller box was mounted below the primary mirrors, easily accessible from the floor. An actuator status indicator box was located in the MMT control room.

The adaptive beam combiner included the mirror facets, the supporting pivots and wedges, the voice coil actuators, the capacitor sensors, and the clock and reference signal generator for the capacitor sensors (see figure 5.4). This assembly bolted directly to the telescope frame. After installation, the entire assembly was rotated and translated for global coarse alignment. Two 10 foot long, 25-pin shielded cables led to the PID controller box.

The PID controller box housed the main power supplies and the PID circuits. Each PID circuit was individually adjustable and replaceable. Each PID card also contained

filtering circuits to reduce the capacitor sensor sampling noise and the high current op-amp voice coil drivers. Two 75 foot long, 25 pin shielded cables exited this controller box and went to the MMT control room. A buffered output from each capacitor sensor was included in one cable, and the wavefront sensor input command used the other.

The actuator status indicator box contained 10-element bar LED displays for each of the 12 actuators. The display showed each actuator motion in real time, useful for diagnostic purposes. When the entire system loop was closed, the motion on the LED displays corresponded to the tilt corrections for atmospheric turbulence. At coarser gain, the LED displays showed gross tip-tilt alignment errors or MMT mirror drift.

5.2.7 Control Overview

Each of the six mirrors on the beam combiner has a two axis control servo system. At the heart of the control system is the PID circuit locking the mirror to the commanded tilt. The source of this command is from FASTTRAC II's wavefront sensor (WFS).

The WFS is a six element Shack-Hartmann sensor which tracks the positions of all six MMT beams from the laser beacon or natural visible guide star (see figure 5.1). Presently, the wavefront sensor itself is a frame transfer 128x64 pixel CCD (described in Close et al. 1994) which takes a minimum of ~14ms between integration and final processing of a frame. This slows down the beam combiner response to a lag time of ~17ms between photon detection and the end of mirror motion.

5.3 Performance

The existing static beam combiner was replaced with the tip-tilt beam combiner on April 15, 1995 at the MMT. Optical problems eliminated two of the six beams. The PID control circuits for each of the remaining eight actuator channels were tuned so that risetimes of 3ms were obtained for

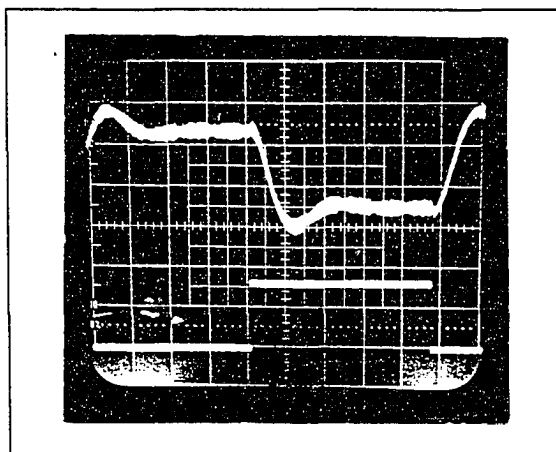


Figure 5.5: The typical closed loop response of one of the 12 tilt channels at the MMT. The bottom trace is 42Hz update input from the WFS and the top trace is the resulting motion of the tilt mirror. Note the 2.5ms 10-90% risetime of the mirror (each division is 5ms in x and 0.5" on the sky in Y).

large $\pm 0.75''$ throws (see figure 5.5). With this servo gain, all eight channels simultaneously gave a slightly underdamped response to a $\sim 150\text{Hz}$ update square wave. However, the system gain could have been increased further to risetimes of $\sim 2\text{ms}$ or less, but at these higher gains, mechanical resonances in the entire beam combiner were excited at $\sim 900\text{Hz}$. In addition, the achieved 3ms risetime was more than adequate for the goal of $0.05''$ rms image motion. Therefore, a lower gain was utilized so as not to excite any global resonances in the beam combiner support structure. All eight channels operated without noticeable mechanical or electrical interference in the telescope environment at this lower gain.

The optical control loop was closed on the beam combiner utilizing a bright V ~ 9 star almost immediately after first-light. The four beams locked immediately to their

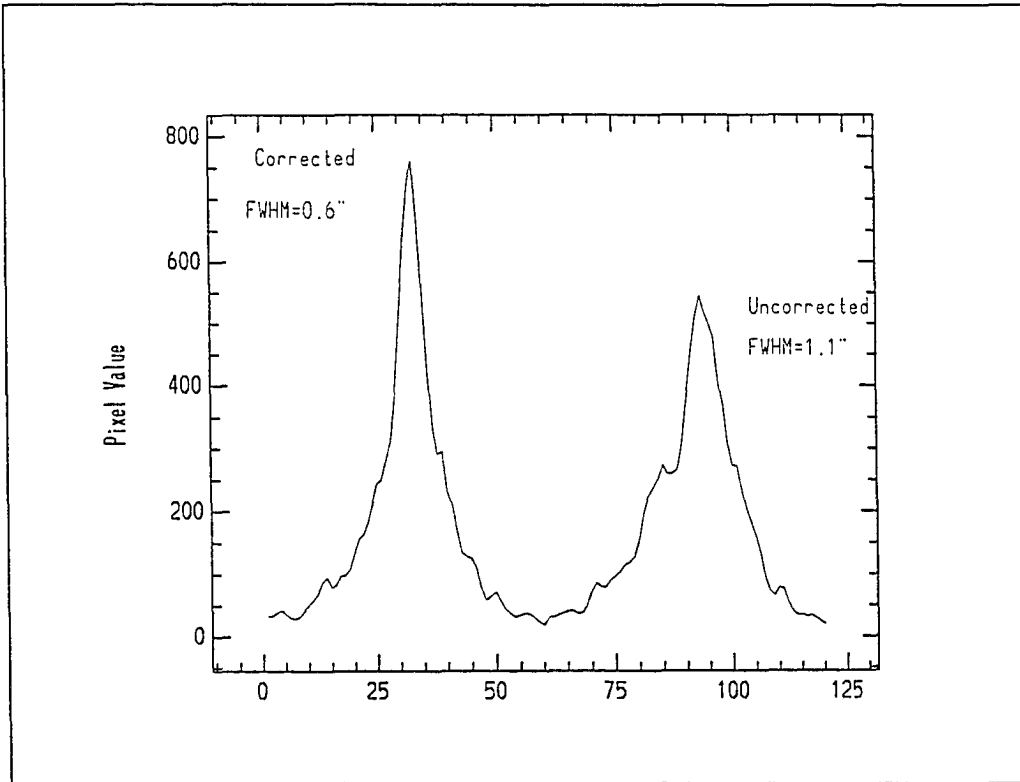


Figure 5.6: comparison between stellar profiles with and without closed loop correction. A guide star (V~9) was guided on (at a 60Hz update rate with 30ms time lag) for 60s while the science camera integrated at K (2.2 μ m with a 0.1"/pixel scale). Typically the corrected image had a Strehl ratio ~1.5 times larger and FWHM ~50% smaller than the uncorrected image.

respective quad cells on the Shack-Hartmann CCD. Due to temporary optical alignment errors, not all the beams were stacked on the science camera when the loop was closed. However, the beam combiner performed excellently, reducing the FWHM of 60s exposures of individual beams from 1.1" to 0.6" (see figure 5.6). The optical loop was closed with time lag ~30ms between the detection of photons and the end of mirror motion. This constrained image motion to less than 0.1" rms in the focal plane.

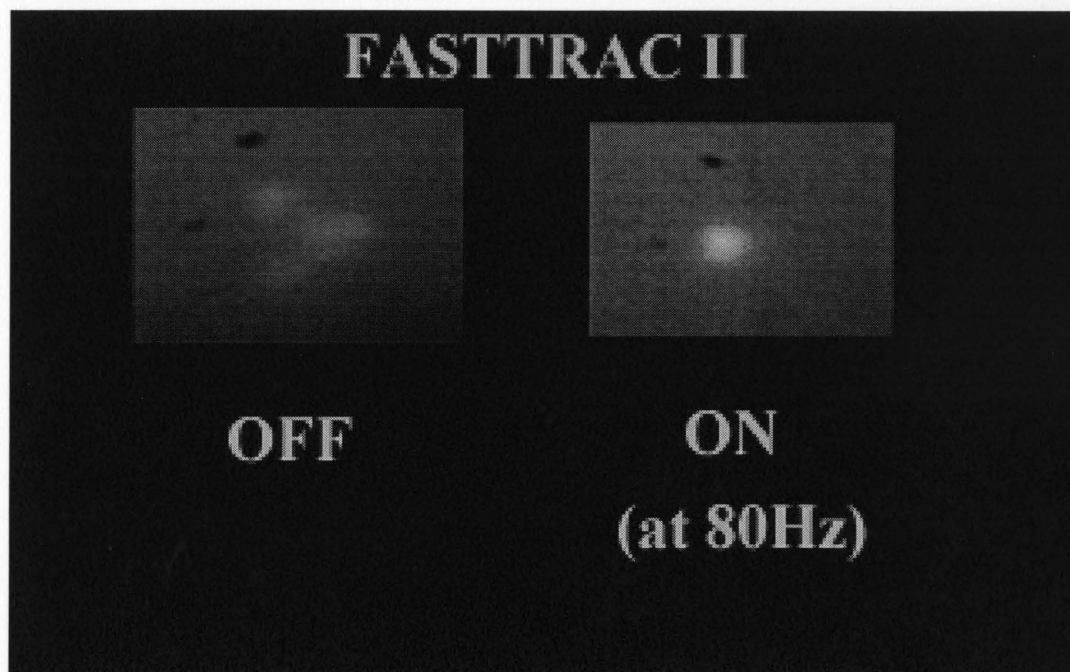


Figure 5.7: A typical gain when FASTTRAC II (-3 dB point at $\sim 4\text{Hz}$) stacks all six beams of the MMT simulator as viewed from the science camera's position in the AO lab.

FASTTRAC II should achieve greater gains later since the optical servo parameters were not optimal during first-light. For example, the CCD update rate was 60Hz with a time lag of $\sim 30\text{ms}$ (since it is a frame transfer device), whereas one can run at updates of 100Hz with only $\sim 17\text{ms}$ time lags on faint ($V \sim 15$) natural guide stars. Moreover, the correct optical alignment in the lab has now been achieved using the MMT telescope simulator (Gray et al. 1995).

5.4 FASTTRAC II's Future

In December of 1995, FASTTRAC II will have an improved optical alignment to allow simultaneous stacking of all six beams on the science camera when the control loop is

closed around the WFS (see figure 5.7). In addition, modifications to the WFS CCD readout software will eventually decrease the time lag to ~ 7 ms (for zero integration time). In fact, only very short ~ 2 ms exposures will be required when the bright ($V \sim 10$) sodium laser guide star system (Lloyd-Hart et al. 1995) is utilized in the Spring. Then only a faint $V \sim 17$ mag natural star will be required for global tilt removal since the stronger, more rapid differential tilts will be removed by tracking the laser beacon. The field of view of FASTTRAC II is $3.9'$ for acquisition of such a $V \sim 17$ star; therefore, nearly 100% sky coverage with this laser system at low galactic latitudes is anticipated.

A time lag of ~ 10 ms implies that the beam combiner closed around the WFS should improve atmospheric turbulence out to ~ 10 Hz. This would typically imply residual image motion of less than $0.05''$ rms. Hence, FASTTRAC II should easily provide $\sim 0.3''$ tip-tilt corrected infrared images, with great potential for significant scientific work. This has already been demonstrated by FASTTRAC in chapters 3 and 4 (cf. Close et al. 1995, Close et al 1995a, Mutz et al 1995, Close et al 1995b, Close et al. 1995c) where the 2.3m telescope was utilized (with only a quarter of FASTTRAC II's collecting power). Hence, CAAO anticipates a rewarding scientific campaign to begin in the December 1995 and continue until the 6.5m is installed.

5.5 Conclusions

A new adaptive tip-tilt beam combiner has been developed for the MMT. This beam combiner stacks all six MMT beams utilizing six tip-tilt mirrors. These mirrors are novel,

high performance, and economical. The tilt of each mirror is sensed through a capacitive displacement sensor, which has a flat response from 0-10kHz and an equivalent noise of ~1 nm. An analogue PID circuit utilizes this positional feedback to lock the mirrors to the commanded tilt via economical voice coil drivers. These mirrors achieve a 10-90% rise time of 3.0ms and have a critically damped response at 100-150Hz update rates. Based on their success, CAAO is implementing similar inexpensive actuators for the 300 element adaptive secondary mirror planned of the 6.5m MMT upgrade.

Six of these tip-tilt mirrors have been incorporated to adaptively combine all six beams from the MMT. During first light of the instrument individual beams improved from 1.1" to 0.6" FWHM in 60s exposures when a guide star was tracked at 60Hz. All the optics in the FASTTRAC II system have now been properly aligned and can accurately stack all six beams on the science camera.

CHAPTER 6

CONTINUING & FUTURE PROJECTS FOR FASTTRAC AND FASTTRAC II

This thesis has shown how a simple tip-tilt instrument can be developed and employed to produce significant and unique astronomical observations. Although only moderate gains in resolution and Strehl are achieved by tilt correction systems like FASTTRAC and FASTTRAC II, it is interesting to note that there are many scientific projects that can be successfully completed with such capabilities. Tilt-correction in combination with properly applied post-detection processing (such as deconvolution) will produce diffraction-limited images in the regime of $D/\lambda < 5$ if a proper PSF is obtained.

Therefore, it is not surprising that FASTTRAC is currently active in several observing campaigns. In particular, David Wittman and Marcia Rieke (Steward Observatory) are studying the stellar population of the nearby face-on spiral galaxy M33. By using FASTTRAC they are able to get individual infrared colors (K, H, and J) for the giant stars in M33. This group and Valentine Ivinov (Steward Observatory) are also imaging other galaxy types in the local group as well.

Steve Mutz and his collaborators at Arizona State University are using FASTTRAC to obtain high resolution infrared images of galaxies imaged by HST in the medium deep survey (Mutz et al. 1996). High resolution infrared images (H and K) are a good complement to the visible HST images (as also demonstrated in figure 1.5) since they will allow the visible to infrared color index of these galaxies to be determined at sub-arcsecond

resolutions.

Eric Hooper and Chris Impey (Steward Observatory) are using FASTTRAC to image the environments around selected QSO's in the infrared at sub-arcsecond resolutions. This requires deep imaging and so capitalizes on the software written by David Wittman and myself to give 95% efficiency to FASTTRAC's use of telescope time.

In addition, FASTTRAC will likely continue monitoring the Galactic Center region (see Chapter 3) for any sign of proper motion from the stars in the central cluster. Such observations should observe the stars closest to Sgr A* ($\sim 0.2''$ away) moving at $\sim 0.016''/\text{yr}$ if Sgr A* is indeed a million solar mass black hole. FASTTRAC may also continue monitoring the gravitational lens b1422+231 to estimate H_0 out to $z=3.6$ (see figure 1.5).

6.1 The Future for FASTTRAC and FASTTRAC II

6.1.1 Possible FASTTRAC Upgrades

To further increase the potential of the FASTTRAC instrument several steps could be taken. The most simple improvement would be to use the same "dichroic/entrance window" that FASTTRAC II uses (see figure 5.1). This would reduce the thermal background by eliminating the current warm dichroic above the science camera.

Significant improvements in sky coverage could be obtained with a new lower readnoise (3 electron rms) CCD. Such a CCD could adequately track guide stars as faint as $R \sim 17$ at 50 Hz at the 2.3m telescope. In addition, it would be beneficial to have a larger, unaberrated

FOV than the present $\sim 16 \times 16''$. This larger FOV could be very useful for allowing the CCD to more efficiently reposition the quad cell to follow the telescope as raster scanning is employed to maximize telescope efficiency. At the moment, the rather small $16 \times 16''$ FOV can only be used to raster scan science targets smaller than $\sim 10''$ across.

An other improvement in the efficiency of FASTTRAC would be in the automated positioning of the CCD to acquire off-axis guide stars. A simple XY Oriel motorized micrometer could be utilized to translate the CCD around the focal plane reflected off the tilted dichroic. Then the observer could simply type in the RA and DEC offsets of her guide star from the science target and the CCD would remotely acquire the star at the position of its quad cell when the science target is centered on the science camera. This would save considerable overhead (~ 20 min of telescope time) when moving to a new science target.

The infrared guiding ability of FASTTRAC could be further improved by the use of the new generation 1024×1024 HgCdTe detector in the Adaptive Optics Science Camera. These new arrays have much lower double correlated read noises of only ~ 15 electrons rms. Since this is factor of ~ 3 improvement in read noise it would allow FASTTRAC to lock onto guide stars of $K \sim 12-13$ at 50 Hz at the 2.3m. The addition of a 1024×1024 chip in the Science Camera would allow FASTTRAC to Nyquist sample a $100 \times 100''$ FOV at K (at the 2.3m) which would cover the entire tip-tilt isoplanatic patch. Such a large FOV will allow FASTTRAC to map out a star formation region or an embedded cluster 16 times faster than the present 256×256 Adaptive Optics Science Camera could, and perhaps more importantly a 1024×1024 camera would only require $1/16^{\text{th}}$ the number of guide stars.

The optics of the FASTTRAC system could also be considerably improved by use of a hexapod for automated collimation of the secondary mirror. Hexapods use six linear stepper motor driven actuators to move a secondary mirror accurately (but slowly) in tip-tilt, piston, and translate in X and Y. Therefore, a hexapod can allow active correction of collimation errors due to flexure and misalignment. Therefore, most of the optical errors detected in §2.7 could be removed and the theoretical Strehl ratio achieved.

Another significant improvement to FASTTRAC would be to boost its correction bandwidth from the present ~ 5 Hz (-3 dB) up to 50 Hz (-3 dB). This could limit residual image motion to less than 0.01" rms. Hence one would always expect to reach diffraction-limited resolutions when $D/\lambda < 6$. Tracking at the required 500 Hz would be only possible on the brightest of guide stars and would likely require a lighter, stiffer secondary mirror that is attached at three or more locations on its back (instead of the present single axial attachment- which allows the possibility of "ringing" at the edge of the mirror). To reach 500 Hz higher bandwidth PZTs would be required. Ideally a new secondary made of silicon carbide for its light weight and high stiffness would also be made.

6.1.2 FASTTRAC II

The new instrument (FASTTRAC II) described briefly in chapter 5 will be fully operational in December 1995. FASTTRAC II has implemented the same successful design philosophy as FASTTRAC in that it replaces an existing static optical element (the MMT beam combiner) with one that rapidly tip-tilt corrects. In this manner the FASTTRAC II

instrument adds no extra "warm" optical elements before the AO science camera (see figure 5.1). Since FASTTRAC II will have the collecting power of a 4.2m telescope it will quickly obtain deep images of faint objects at $\sim 0.3''$ resolutions. Hence FASTTRAC II will most likely obtain excellent extra-galactic images. Although the complex PSF that will be produced by the combination of the six MMT beams will require a very accurate PSF model if morphological information is to be reliably extracted from such images.

6.1.3 Laser Upgrade

An exciting upgrade to the FASTTRAC II instrument will be the addition of a Na Laser guide star system in the Spring of 1996. Such a system should achieve close to full sky coverage, requiring only a faint $V \sim 17$ visible guide star (within $\sim 60''$) to lock the global tilt across the whole MMT. Such a system would be able to correct almost any science field at low galactic latitudes (at high galactic latitudes suitable guide stars are still rare). This type of sky coverage would obviously allow many more scientific projects to be successfully completed.

The addition of a laser to FASTTRAC II would also allow the Center for Astronomical Adaptive Optics to gain invaluable experience with carrying out scientific observations with a laser guide star system. This experience will be critical to the quick successful development of a full AO system for the MMT 6.5m upgrade, since the laser and most of the opto-mechanics will be directly used in the 6.5m system. This system is

described in Appendix A.

6.2 Future Tip-Tilt Astronomy

The type of science that can be achieved by any AO system is closely matched to the limits and abilities of that particular system. Therefore this discussion will be broken into two parts covering the FASTTRAC, and FASTTRAC II systems. A few simple examples will be given of science projects that could be successfully completed by the system in question.

6.2.1 Science to be Done With FASTTRAC

FASTTRAC's main abilities is that it can use infrared guide stars, (or faint visible guide stars) and that it can correct a large field of view. A good project for FASTTRAC should also have an advantage to imaging in the infrared. For brevity just two examples will be presented here to show how FASTTRAC could be used for both infrared and visible guide star tracking.

One good example that needs infrared guide star tracking would be to continue imaging the inner 30x30" of the Galaxy (see Chapter 3 for more details). Such images should provide a database for the detection of extreme proper motion stars recently having a "hard" scattering off the central black hole. In addition, these images may also detect the 0.016"/yr

proper motion of the stars closest to Sgr A*. If no proper motions are detected than it is likely that Sgr A* is not a massive black hole.

An other good use of FASTTRAC would be to image the host galaxies of QSO's which should peak in contrast to the unresolved central AGN at $\sim 1.6 \mu\text{m}$ (the H band). Therefore, FASTTRAC should be able to sharpen the AGN enough so that PSF subtraction reveals the host galaxy more efficiently than either visible HST imaging or uncorrected infrared imaging (cf. McLeod 1994). Such observations could help settle the dispute of whether all AGN have host galaxies. In addition, the morphology of the host galaxies might help explain how AGN are "fed" and how they effect (and are effected by) their nearby surroundings. For this project the CCD would be utilized to track on any nearby $V \sim 16^{\text{th}}$ mag stars (or the central AGN could be utilized in many cases). By using FASTTRAC's ability to efficiently raster scan the guide star and science object, limiting magnitudes of ~ 22 mag/(square arcsecond) should be reached at H in ~ 90 min of telescope time at the 2.3m. This should be adequate for the detection of most nearby host galaxies.

6.2.2 Science to be Done With FASTTRAC II

The FASTTRAC II instrument is similar to FASTTRAC in that it is best used for objects that are interesting at moderate resolutions in the infrared. However FASTTRAC II's large 4.2m collecting area makes it a particularly good system for producing high resolution images of faint objects. In general there are few very deep images obtained at high resolutions. This is due to the lack of available integration time on HST and the domination

of tracking errors and atmospheric seeing in uncorrected deep ground-based images.

In particular, FASTTRAC II could obtain deep images of some of the few fields already deeply imaged by HST to obtain the infrared colors and morphologies of the many "blue" irregular galaxies detected by HST at $z \sim 0.3$. A lack of detection of these galaxies in the infrared could help explain why the excess of these blue galaxies is not seen in the infrared deep galaxy counts. In addition, the infrared morphologies will likely help decide whether these "blue" galaxies are "normal" starbursts or blue due to interactions (or whether they are "galaxies" at all). These deep images will also be useful for deconvolution by utilization of the PSF that will hopefully show up in the $30 \times 30''$ FOV. As with FASTTRAC, FASTTRAC II's control system allows raster scanning and so such deep images can be acquired efficiently.

FASTTRAC II is a very good instrument for deeply probing the environments around QSO's as is currently being done with the FASTTRAC instrument by Eric Hooper. Such a project could be carried out much faster with FASTTRAC II's superior collecting area.

Imaging of faint isolated objects should be avoided since FASTTRAC II will have considerable structure in its PSF. Hence the best science will be only be done if there is a isolated calibration point source in the field with the science target. The PSF will have time dependant structure due to systematic and random errors in the stacking of all six beams. For example, the stacking errors could cause a point source to appear as a tight binary, and without a calibration point source nearby in the field it would be hard to tell what the true object morphology really is. In general this is in an annoying problem for interpreting the

validity of any structure in images obtained with AO.

6.3 Conclusions

Astronomical observations with FASTTRAC are continuing. These observations will obtain significant astronomical insight into objects such as the massive black hole at the center of the galaxy, the stellar populations of the nearest galaxies, and the environments around distant QSO's.

FASTTRAC II will soon (December 1995) start making observations optimized for deep imaging at moderate resolutions. Moreover, in the spring of 1996 FASTTRAC II's laser guide star system should increase its sky coverage greatly.

APPENDIX A

THE 6.5M MMT AO SYSTEM: AN EXAMPLE OF FUTURE OF ADAPTIVE OPTICS SYSTEMS

The single 6.5m mirror being installed in the MMT will provide an excellent opportunity to develop a very powerful full AO system. This appendix will outline what is planned for this system as a detailed example of what a future AO systems will be like.

Based, in part, on the excellent performance of FASTTRAC's tip-tilt secondary the Center for Astronomical Adaptive Optics is planning to implement the world's first fully adaptive secondary (cf. Martin et al. 1995). This secondary will not only correct tip-tilt but it will also be deformed by ~300 voice coil actuators so that nearly perfect images will be obtained at K (Sandler et al. 1995). These voice coil actuators are based on those developed for the FASTTRAC II beam combiner (see §5.2).

In typical full AO systems the deformable mirror must be at a reimaged pupil (requiring typically 3-5 extra warm optical surfaces) this will increase the thermal emissivity of these systems considerably and limit their usefulness at wavelengths longer than 2 microns. The huge advantage of an adaptive secondary is that it is at the telescope pupil and so no extra warm surfaces need to be added in front of the science camera (as shown by the FASTTRAC II design).

Since it will require a very bright natural guide star of at least V~8 mag to get enough flux into each of the 6.5m's ~300 subapertures (in the ~2ms sample time allowed) it is critical that a laser guide star be used to provide better sky coverage. Since a laser guide star

has the advantage that a narrow 589nm filter can be used to eliminate the sky and moon background, (while keeping most of the light from the laser guide star) one needs a $V=9^{\text{th}}$ mag *laser* guide star for the 6.5m system. Hopefully the addition of such a laser guide star system will be relatively simple since the laser should have already been fully developed for the FASTTRAC II system. The usefulness of such a laser system will be in its ability to reliably produce a sub-arcsecond 9^{th} magnitude star (~ 5 Watts at 589nm). This looks promising since Jacobsen et al. (1995) have already produced a $V=9.85$ laser star with a 1.6" FWHM using a 2.5Watt Coherent ring dye laser at 589nm. According to calculations by Webb (1995) this laser guide star should not have been saturated, and so the large 1.6" size of the beacon was likely due to poor seeing that night at the MMT.

Of course, as mentioned chapter 1, the laser system will still be dependant on nearby natural guide stars for tilt correction. To maximize the number of available natural stars a infrared tilt quad cell will be utilized. The advantage of tracking in the infrared (first done with FASTTRAC) is that the tilt star shares the higher order correction provided by the laser guide star resulting in a Strehl of ~ 0.6 at K. This is in contrast to a visible guide star which would be poorly corrected by only 300 elements across a 6.5m aperture, (at V the guide star is composed of many speckles and has an almost uncorrected Strehl ratio < 0.01). This high Strehl of 0.6 at K will give the quad cell much higher sensitivity and will increase the guide star contrast by a factor of ~ 10 (assuming λ/D pixels). Therefore, adequate image stabilization should be possible on stars of $V \sim 18.5$ mag; hence nearly full sky coverage should be obtainable. However, there is no available IR detector that could obtain these

performances. For example the current 256x256 NICMOS3 arrays would only be able to guide on stars of $V \sim 16$ (for a -3 dB point at 10Hz) with a double correlated readnoise of ~ 50 electrons rms. It may be possible to use a "rejected" 1024x1024 HgCdTe chip with high dark current and poor cosmetics to take advantage of their superior ~ 15 electron rms read noise. Such a tilt sensor still could only use stars of $V \sim 17$. One can eliminate read noise altogether with a IR solid state photomultiplier (SSPM) such as that developed by Rockwell. However, these high speed photon counting devices so far have low quantum efficiency and so are not yet useful. Future edge-illuminated (instead of the present back illuminated) SSPMs should reach theoretically $V \sim 18.5$ ($K=17$) in a 10ms exposure with the 6.5m. A IR quad cell of such SSPM's should achieve nearly full sky coverage (86% of the sky at 30° and 53% at the galactic pole; interpreted from Bacall & Soniera 1981) with the 6.5m AO system.

Hence the 6.5m AO system will use an adaptive secondary and a laser beacon to adaptively correct science targets over most of the sky. The on-axis corrected images produced by the system should have Strehl ratios of ~ 0.6 at K (for an off-axis natural tilt star, Sandler et al. 1995). The images will have a resolution of $0.07''$ FWHM and have Strehl ratios of up to 0.4 at distances of $\sim 15''$ from the on-axis science target. Hence the relatively inexpensive 6.5m AO system will achieve higher resolutions than the much more expensive HST/NICMOS near infrared camera which will only produce $0.2''$ images at K. In fact the 6.5m system's $0.07''$ K images are very competitive with what HST can obtain at any wavelength since the finest $0.04''$ WFPC II pixels limit wide field ($35 \times 35''$) HST images to $\sim 0.08''$ (without sub-pixel stepping). Of course the HST Faint Object Camera (FOC) can

produce very high resolution (properly sampled) 0.028" images but the FOV is limited to only 3.5x3.5".

However, due to anisoplanatic effects creating a strongly position dependant PSF in the AO images HST/NICMOS will still be able to obtain far more stable images over a large FOV for accurate photometry. This makes HST/NICMOS the better instrument for studies of weak variability and faint object recovery from crowded fields. Nevertheless, there is a vast amount of science that can be achieved with the 6.5m system that either could not be done with HST/NICMOS due to cost or due to HST's smaller 2.4m aperture.

A.1 Science to be Done With The 6.5m System

The advantages of the 6.5m system are that it has a large light grasp and it has the ability of producing 0.07" images with 0.6 Strehl ratios at K. In addition, the laser guide star system opens up almost the whole sky for adaptive correction (see §6.1.2 for more details). These attributes will make the 6.5m system one of the most powerful telescopes in existence. The largest drawback to the system is that it may not be fully operational until 1997 and so will directly compete with HST/NICMOS and several other large telescope AO systems (cf. the KECK 10m system; Olivier et. al. 1995). However, in thermal emissivity and optical throughput the 6.5m will be unequaled by any ground-based system due to its adaptive secondary. The drawback is the risk involved in developing world's first adaptive secondary. However, there is currently successful development occurring of a prototype 5x5 adaptive "secondary" that will soon prove "proof of concept" for the 300 actuator system (Bruns et

al. 1995). Therefore it will be assumed here that the system will work as predicted.

The range of science projects that could be obtained with such an instrument is vast. Good examples are 0.07" images of extended objects like the planets. For example, high resolution AO images of Saturn during its next ring plane crossing would allow faint objects in the rings (or near them) to be seen for the first time, in this manner the 6.5m system could in theory detect new Saturnian moons during the next plane crossing. Another solar system task well suited to high resolution infrared imaging is the continued mapping of Saturn's largest moon Titan. Titan's thick atmosphere has the lowest opacity in methane bands at 1.6 and 2 microns. The 6.5m would provide maps of Titan's surface accurate to ~500 km on the ground. Of course there many other examples of solar system objects which could also be better imaged with AO but they are too numerous to be listed here.

Some of the nearby stars would also look quite interesting at these resolutions. For example, the dusty shells around some giants will be resolved. Young stars will also be prime targets. In particular, the stellar envelopes and dusty circumstellar disks around young stars will show detail at the 10 AU scale in the nearby Taurus star formation cloud. Such images of circumstellar disks around the youngest stars should show "gaps" due to tidal clearing from forming planets. Hence many young proto-solar systems could be studied to give insight on the frequency and distribution of young planets. Moreover, the study of the interaction of these disks and the strong winds usually associated with them (as in most T Tauri stars) is a poorly understood process and images at these resolutions should help in untangling the complex bond between disk accretion and polar winds.

The large collecting area of the 6.5m makes an ideal extra-galactic instrument. For example, deep high resolution images of distant galaxy clusters will measure the morphologies of the faintest members of these clusters. This project could also help refine the M/L ratio for these clusters and perhaps detect more luminous matter than was previously detected without AO. Moreover, the 0.07" images delivered by the 6.5m will nicely complement all the visible images taken by HST of any of these deep sky objects. Hence color gradients for all these galaxies can be obtained with $\sim 0.1''$ resolutions. The addition of a spectrograph to the 6.5m AO system will enable velocity dispersions to be obtained from the inner 0.1" around AGNs. Such observations will help determine if there are indeed super massive black holes at the center of AGNs.

Cosmological work can be carried out on the ground instead of with expensive HST time. For instance well known gravitational lenses can be adaptively imaged to completely split the inner sub-arcsecond pairs (such as the 0.4" pair in figure 1.5). These pairs will often have time delays of only a few hours between transmission of intrinsic variations in the lensed background AGN. Hence, observations of the systems (using lensed images themselves as the tilt beacon and the laser for the higher order term correction) should within a few nights measure this time delay accurately. These measurements coupled with a good knowledge of the lensing galaxy's mass (which can also be estimated from the excellent infrared colors of the lens produced by the 6.5m), will give an independent estimate of H_0 over large redshifts ($z \geq 3.6$). Other cosmological work that could be carried out with the 6.5m is the estimate of galactic distances using the surface brightness fluctuations (SBF) of the

galaxies. The distance that this technique can be used to is directly proportional to the angular resolution of the telescope, therefore observations with 6.5m could theoretically measure distances out to 100 Mpc (at the moment only ~15 Mpc can be reached using SBF from the ground). Using these SBFs one should be able to obtain another estimate of H_0 .

In conclusion, the MMT 6.5m state-of-the-art AO system is expected to be operational around 1998. The successful operation of this laser guide star system would make the 6.5m one of the most powerful imaging telescopes in the world.

REFERENCES

- Aaronson, M., Huchra, J., & Mould, J. 1979, *ApJ*, **229**, 1
- Allen, D. A., & Sanders, R. H. 1986, *Nature*, **319**, 191
- Antonucci R. 1993, *ARA&A*, **31**, 473
- Backer D. C., & Sramek R. A. 1982, *ApJ*, **260**, 512
- Backer, D. C., & Sramek, R. A. 1987, in *The Galactic Center* (AIP Conf. Proc. No **155**), ed D. C. Backer (NY: AIP), 163
- Backer, D. C., Zensus, J. A., Kellermann, K. I., Reid, M., Moran, J. M., & Lo, K. Y. 1993, *Science*, **262**, 1414
- Bahcall, J., & Soniera, R., 1981, *ApJ. Suppl.*, **47**, 357
- Becklin, E. E., & Neugebauer, G. 1975, *ApJ*, **200**, L71
- Blandford, R. D., & Narayan, R. 1992, *ARA&A*, **30**, 311
- Broadhurst, T., & Lehar, J. 1995, *ApJL*, submitted
- Brown, D. S. et al. 1988, in ESO Conf. **30**, "*Very Large Telescopes and Their Instrumentation*", ed. M. H. Ulrich (Garching, ESO), 761
- Bruns, D.G., et al. 1995, *ESO Topical meeting on Adaptive Optics* (Garching), in press
- Bruzual, G., & Charlot, S. 1993, *ApJ*, **405**, 538
- Christou, J. C. 1992, *PASP*, **103**, 1040

- Close, L.M., Richer, H., & Crabtree, D. 1990, *AJ*, **100**, 1968
- Close, L.M., McCarthy, D., Christou, J., & Melia, F. 1992, *BAAS*, **24**, 1178
- Close, L.M., & McCarthy, D.W. 1993, *Proc. SPIE*, **1920**, 353
- . 1994, *PASP*, **106**, 77
- Close, L.M., Wittman, D., & McCarthy, D.W. 1994, *Proc. SPIE* **2201**, 447
- Close, L.M., McCarthy, D.W., & Melia, F. 1995, *ApJ*, **439**, 682
- Close, L.M., Hall, P.B., Liu, C.T., & Hege, E.K. 1995a, *ApJ*, **452**, L9
- Close, L.M., Brusa, G., Bruns, D.G., Lloyd-Hart, M., & McCarthy, D.W. 1995b, *SPIE*, **2534**, 105
- Close, L.M. et al. 1995c, *ESO Topical meeting on Adaptive Optics* (Garching), in press
- Cutri, R., et al. 1994, *ApJ*, **424**, L65
- DePoy, D. L., & Sharp, N. A., 1991, *AJ*, **101**, 1324
- Downes, D., Radford, S. J. E., Greve, A., Thum, C., Solomon, P. M., & Wink, J. E. 1992, *ApJ*, **398**, L25
- Eckart, A., Genzel, R., Krabbe, A., Hofmann, R., van der Werf, P. P., & Drapatz, S. 1992, *Nature*, **335**, 526
- Eckart, A., Genzel, R., Hofmann, R., Sams, B. J., & Tacconi-Garman, L. E. 1993, *ApJ*, **407**, L77
- Eckart, A. 1995 (private communication)
- Eisenhardt, P., et al. 1995 *BAAS*, **27**, 886
- Elias, J.H., Frogel, J.A., Matthews, K., & Neugebauer, G. 1982, *AJ*, **87**, 1029
- Elizalde F., & Steiner J.E. 1994, *MNRAS* **268**, L47
- Elston, R., McCarthy, P. J., Eisenhardt, P., Dickinson, M., Spinrad, H., Januzzi, B. T., & Maloney, P. 1994, *AJ*, **107**, 910

- Faber, S. M., & Jackson, R. E 1976, *ApJ*, **204**, 668
- Forrest W. J., Pipher J. L., & Stein, W. A. 1986, *ApJ*, **301**, L49
- Fried, D.L., 1966 *JOSA*, **56**, 1372
- Fugate, R.Q. et al. 1991, *Nature*, 353, 1
- Fugate, R.Q. 1992, Proc. "*Laser Guide Star Adaptive Optics Workshop*" 134
- Golimowski, D. A., Clampin, M., Durrance, S. T., & Barkhouser, R. H. 1992, *Appl. Opt.*, **250**, 666
- Graham, J.R., & Liu, M.C. 1995, *ApJL*, in press.
- Graves, J.E., Roddier, F., Roddier, C., Northcott, M. 1995, Proc. *Topical Meeting on Adaptive Optics*, Garching, ESO, in press
- Gray, P., Lloyd-Hart M., Angel, J.R.P., McCarthy, D.W., Sandler, D.G., Close, L.M., Brusa, G., McLeod, B.A., Groesbeck, T.D., Wittman, D.M., Ryan, P.T., Martinez, T., Bruns, D.G., Hughes, J.M., & Cheselka, M. 1995, proc. *SPIE*, **2534**, 2
- Groesbeck, T.D., Stahl, S.M., & Sandler, D.G. 1995, proc. *SPIE*, **2534**, 17
- Haller, J.W., Rieke, M.J., Rieke, G.H., Tamblyn, P., Close, L.M., & Melia, F. 1996, *ApJ*, in press
- Herbst, T. M., Beckwith, S. V. W., & Shure M. 1993, *ApJ*, **411**, L21
- Hollywood, J.M., Fulvio, M., Close, L.M., McCarthy, D., & DeKeyser, T.A. 1995, *ApJ*, **448**, L21
- Hines, D.C., & Wills, B.J. 1993, *ApJ*, **415**, 82
- Jacobsen et al. 1994, *SPIE*, **2201**, 342
- Jannuzi, B.T., Elston, R., Schmidt, G.D., Smith, P.S., & Stockman, H.S. 1994, *ApJ*, **429**, L49
- Jefferies, S.M., & Chirstou, J.C 1993, *ApJ*, **415**, 862
- Lacy, J.H., Achtermann, J.M., & Serbyn, E. 1993, *ApJ*, **415**, 205

- Lacy, J. H., Townes, C. H., & Hollenbach, D. J. 1982, *ApJ*, **262**, 120
- Lawrence A., et al. 1993, *MNRAS*, **260**, 2
- Lloyd-Hart, M., Angle, J.R.P., Jacobsen, B., Wittman, D., Dekany, R., McCarthy, D., Kibblewhite, W. Wild, Carter, B., & Beletic, J. 1995, *ApJ*, **439**, 455
- Lloyd-Hart, M., Dekany, R., McLeod, B., Wittman, D., Colucci, D., McCarthy, D., & Angel, R. 1993, *ApJ Lett*, **402**, L81
- Lynden-Bell, D., & Rees, M. 1971, *MNRAS*, **152**, 461
- Major, V., Doel, A. P., Dunlop, C. N., Myers, R. M., Purvis, A., & Thompson, M. G. 1990, *Proc SPIE*, **1236**, 179
- Martin, H.M. 1987, *PASP*, **99**, 1360
- Martin et al. 1995, ESO conf. proc. "*OSA Topical Meeting on Adaptive Optics*", Garching October 2, 1995 in press
- Masswinkel, F. et al. 1988, in ESO Conf. **30**, "*Very Large Telescopes and Their Instrumentation*", ed. M. H. Ulrich (Garching, ESO), 751
- Matthews et al. 1994, *ApJ*, **420**, L13
- McLeod, K.K. 1994, Ph.D Thesis, University of Arizona.
- McCarthy, D.W., McLeod, B., & Barlow, D., 1990, *Proc. SPIE*, **1237**, 496
- McCaughrean et al. 1994, *Infrared Astronomy with Arrays: The Next Generation* (ed. I.S. McLean), 297
- McCaughrean, M.J., & Stauffer, J.R. 1994, *AJ*, **108**, 1382
- McClure, R. D., et al. 1989, *PASP*, **101**, 1156
- McGinn, M. T., Sellgren, K., Becklin, E. E., & Hall, D. N. B. 1989, *ApJ*, **338**, 824
- Melia, F. 1992, *ApJ*, **398**, L95
- . 1994, *ApJ*, **426**, 577

- Melia, F., Jokipii, R., & Narayanan, A. 1992, *ApJ*, **395**, L87
- Melia, F., & Lamb D. 1995, *ApJ*, **439**, 805
- Mobasher, B., Ellis, R.S., & Sharples, R.M. 1986, *MNRAS*, **223**, 11
- . 1993, *MNRAS*, **263**, 560
- Mutz, S.B., Windhorst, R.A., Wittman, D., Close, L.M., McCarthy, D.W. 1996 *ApJ*, in press
- Press, W. H., & Rybicki, G. B. 1989, *ApJ*, **338**, 277
- Rieke, M. J., Rieke, G. H., Green, E. M., Montgomery, E. F., & Thompson, C. L. 1993, *Proc. SPIE*, **1946**, 179
- Rieke, G. H., & Lebofsky, M. J. 1982 The Galactic Center (AIP conf. proc. No **83**), 85
- Rieke, G. H., Rieke, M. J., & Paul, A. E. 1989, *ApJ*, **336**, 752
- Roddier, C., Roddier, F., Northcott, M.J, Graves, J.E., & Jim, K. 1996, *ApJ*, in press
- Roddier, F. 1988 *Applied Optics*, **267**, 7, 1223
- Roddier, F., Northcott, M.J., & Graves, J.E. 1991, *PASP*, **103**, 131
- Rosa, M. R., Zinnecker, H., Moneti, A., & Melnick, J. 1992, *A&A*, **257**, 515
- Rousset ,G., et al. 1990, *SPIE Conf.*, **1114**, 92
- Rowan-Robinson, M. et al. 1993, *MNRAS*, **261**, 513
- Rowan-Robinson, M. et al. 1991, *Nature*, **351**, 719
- Ruffert M., & Melia, F. 1994, *A&A*, **288**, L29
- Sanders, D. B., et al. 1988, *ApJ*, **325**, 74
- Sandler D.G. et al. 1995 *SPIE*, **2534**, 372
- Schmidt, G. 1991, (private communication)

- Schneider, D.P., Schmidt, M., & Gunn, J.E. 1989, *AJ*, **98**, 1507
- Sellgren, K., Mc Ginn, M.T., Becklin, E. E., & Hall, D. N. B. 1990, *ApJ*, **359**, 112
- Serabyn, E., Lacy, J. H., Townes, C.H., & Bharat, R. 1988, *ApJ*, **326**, 171
- Serjeant, S., Lacy, M., Rawlings, S., King, L., & Clements, D.L 1995, *MNRAS*, preprint
- Shapiro, S. L., Lightman, A. P., & Eardley, D. M. 1976, *ApJ*, **204**, 187
- Soifer, B.T., Neugebauer, G., Matthews, K., Lawrence, C., & Mazzarella, J. 1992, *ApJ*, **399**, L55
- Stetson, P. B. 1987, *PASP*, **99**, 191
- Stier, M., Duffy, M., Gullapalli, S., Rockwell, R., Sileo, F., & Krim, M. 1989, *IEEE Trans. Nuc. Sci.*, **36**, 903
- Tamblyn, P., Rieke, G. H., Hanson, M.M., Close, L. M., McCarthy D. W., & Rieke, M. J. 1996, *ApJ*, in press
- Thompson, L. & Ryerson, H. 1984, *Proc SPIE*, **445**, 560
- Trentham, N., 1995, *MNRAS*, in press
- Turner E.L., Ostriker J.P., & Gott J.R.III 1984, *ApJ*, **284**, 1
- Veilleux, S., Kim, D.C, Sanders, D.B., Mazzarella, J.M., & Soifer, B.T. 1995, *ApJS*, **98**, 171
- Webb, C. 1995 (private communication)
- Wittman, D., Angel, R., Lloyd-Hart, M., Colucci, D., & McCarthy, D. 1992, in ESO Conference on "*High Resolution Imaging by Interferometry*", 453
- Yusuf-Zadeh F., Morris., & Ekers R.D., 1990 *Nature*, **348**, 45